

## Editorials' corner – a personal view

### New approaches to the processing and tailoring of the properties of reinforced polymers

T. Czigány<sup>1\*</sup>, Gy. Marosi<sup>2</sup>, M. Q. Zhang<sup>3</sup>

<sup>1</sup>Department of Polymer Engineering, Budapest University of Technology and Economics, H-1111 Budapest, Műegyetem rkp. 3, Hungary

<sup>2</sup>Organic and Chemical Technology Department, Budapest University of Technology and Economics, H-1111 Budapest, Műegyetem rkp. 3, Hungary

<sup>3</sup>Materials Science Institute, Zhongshan University, Guangzhou 510275, P. R. China

This issue of eXPRESS Polymer Letters contains selected papers presented at the 3<sup>rd</sup> China-Europe Symposium on Processing and Properties of Reinforced Polymers held in Budapest, 11–15 June 2007. The founders of this conference series are Prof. C. G'Shell and Prof. S. L. Bai. The first conference was held in Nancy, France, while the second one in Beijing, China. The third conference at Budapest was attended by 180 participants from 30 countries, who visited also the exhibition 'Composites on Tour' ([www.compositesontour-2.be](http://www.compositesontour-2.be)) supported by the European Union. This exhibition involved the very first presentation of the most up-to-date composite products of the leading designers and companies in Europe.

Advancement of modern polymer composites such as nanocomposites, smart composites, hybrid com-

posites, fire retarded and green composites are increasingly represented at the meetings of this conference series. The common thinking of scientists of modelling, simulation, processing and testing of polymer composites generated new ideas, and created new cooperation among research groups. This meeting paid special attention to the establishment and enhancement of direct connections among the participants, and provided consultation possibilities for students.

This issue presents representative selection of the most recent results of the abovementioned research areas within the field of reinforced polymers. These papers, similarly to the relevant talks at the Budapest meeting, will, hopefully, promote the understanding among the researchers of the field and this tendency will surely continue in Guilin, China, where the fourth conference will be held in 2009.



Prof. Dr. Tibor Czigány



Prof. Dr. György Marosi



Prof. Dr. Ming Qiu Zhang

Chairmen of 3<sup>rd</sup> China-Europe Symposium on Processing and Properties of Reinforced Polymers  
Members of International Advisory Board of eXPRESS Polymer Letters

\*Corresponding author, e-mail: [czigany@eik.bme.hu](mailto:czigany@eik.bme.hu)  
© BME-PT and GTE

# Electrical relaxation dynamics in TiO<sub>2</sub> – polymer matrix composites

G. A. Kontos<sup>1</sup>, A. L. Soulintzis<sup>1</sup>, P. K. Karahaliou<sup>1,2</sup>, G. C. Psarras<sup>2</sup>, S. N. Georga<sup>1</sup>,  
C. A. Krontiras<sup>1\*</sup>, M. N. Pisanias<sup>1</sup>

<sup>1</sup>Department of Physics, University of Patras, 26504 Patras, Greece

<sup>2</sup>Department of Materials Science, University of Patras, 26504 Patras, Greece

Received 27 July 2007; accepted in revised form 20 September 2007

**Abstract.** Polymer matrix-TiO<sub>2</sub> composites were prepared in three different filler concentrations. The electrical relaxation dynamics as well as the electrical conductivity of all samples were examined by means of Broadband Dielectric Spectroscopy (BDS) over a wide frequency and temperature range. The recorded relaxation response includes contributions from both the polymer matrix and the reinforcing phase. Two relaxation modes ( $\beta$  and  $\gamma$ ) are observed in the low temperature region, which are attributed to the re-orientation of polar side groups of the matrix and rearrangement of small parts of the polymeric chain respectively. The  $\alpha$ -relaxation and the Maxwell-Wagner-Sillars effect (MWS), attributed to the glass-rubber transition of the polymeric matrix and to interfacial polarization phenomena respectively, are observed in the high temperature region. These two mechanisms are superimposed, thus a computer simulation procedure was followed in order to distinguish them. MWS effect becomes more pronounced with increasing concentration of the filler following an Arrhenius behaviour. The relaxation frequencies corresponding to  $\alpha$ -mode follow the Vogel-Tamann-Fulcher (VTF) equation. An additional relaxation mode is recorded at relatively high temperatures and high frequencies. Its occurrence and dynamics are related to the presence and the concentration of the filler. Finally, the Direct Current (DC) conductivity follows the VTF equation.

**Keywords:** polymer composites, particulate filler, polar oxide, dielectric spectroscopy

## 1. Introduction

Recently polymer matrix – ceramic filler composites receive increased attention due to their interesting electrical and electronic properties. Integrated decoupling capacitors, angular acceleration accelerometers, acoustic emission sensors and electronic packaging are some potential applications [1, 2]. Furthermore, electrical properties such as dielectric permittivity can be suitably adjusted, simply by controlling the type and the amount of ceramic inclusions. Ceramic materials are typically brittle, possess low dielectric strength and in many cases are difficult to be processed requiring high temperatures. On the other hand, polymers are flex-

ible, can be easily processed at low temperatures and exhibit high dielectric breakdown fields [3]. Integrating two complementary materials in a new composite structure, results in a novel material system, the performance of which is expected to be superior in comparison to the corresponding of the constituent phases. Composite materials of an amorphous polymeric matrix and fine ceramic particles are considered as heterogeneous disordered systems. Their electrical performance is directly related to the permittivities and conductivities of their constituents, the volume fraction of the filler and the size and shape of its particles. Titanium dioxide has been the subject of many studies

\*Corresponding author, e-mail: [krontira@physics.upatras.gr](mailto:krontira@physics.upatras.gr)  
© BME-PT and GTE

because of its remarkable optical and electronic properties [4–6]. It can be crystallized in three distinct structures, which are known as rutile, anatase and brookite. Epoxy resins are considered as a common and successful polymer matrix for the fabrication of composite materials due to their good adhesion with reinforcing elements, enhanced thermal stability, resistance to chemical attack and resistance to degradation under the influence of corrosive environment [7–11].

In the present study, the dielectric properties of composite systems consisting of an epoxy resin and ceramic titanium dioxide particles are investigated by means of Broadband Dielectric Spectroscopy (BDS) in a wide temperature range.

## 2. Experimental details

### 2.1. Sample preparation

Polymer matrix – ceramic TiO<sub>2</sub> composites were prepared in three different concentrations, namely 10 phr (parts per hundred), 30 phr and 50 phr. For the preparation of the samples a commercially available low viscosity epoxy resin (Epoxol 2004A, Neotex S.A., Athens, Greece) was used as a pre-polymer. The employed curing agent (Epoxol 2004B) operates at a slow rate allowing the addition of large quantities of the reinforcing phase. Ceramic titanium dioxide powder (Sigma-Aldrich) belongs to the rutile type with mean particle diameter less than 5 μm. The followed procedure includes mixing of the resin with the curing agent in a 2:1 (w/w) ratio. While the above systems were still in the liquid state, various amounts of the ceramic powder were added for the production of the composite samples. The initial curing took place at ambient for a week, followed by post-curing at 100°C for 4 hours. The thickness of the samples ranges from 1.5 to 2.5 mm and the diameter of all samples exceeds 30 mm.

### 2.2. Dielectric measurements

For the electrical characterization of the composites, BDS was employed in the frequency range of 0.1 Hz to 1 MHz, using Alpha-N Frequency Response Analyser, supplied by Novocontrol. The BDS-1200, parallel-plate capacitor with two gold-plated electrodes system, supplied also by Novocontrol, was used as test cell. The dielectric cell was electrically shielded in nitrogen gas atmosphere

and isothermal frequency scans were conducted for each of the examined specimens. Measurements were performed in the temperature range of –100°C to 150°C. The employed temperature step between successive frequency sweeps was 10°C. Temperature was controlled by the Quattro system within ±0.1°C. The instrument is interfaced to a PC for simultaneous control and automated data acquisition. The applied ac voltage used is  $V_{rms} = 1.0$  V.

## 3. Experimental results

### 3.1. Low temperature region

In polymer matrix composites electrical relaxation phenomena are expected to include contributions from both the polymer matrix and the ceramic filler. Thus, the respective dielectric response is expected to include relaxations arising from phase transitions of the polymer matrix ( $\alpha$ -relaxation), as well as faster relaxations ( $\beta$ ,  $\gamma$ ) attributed to reorientations and segmental motions of parts of the polymer chain. Moreover, due to the presence of the filler, interfacial phenomena (MWS effect) are expected to occur.

The recorded dielectric data could be expressed in terms of real ( $\epsilon'$ ) and imaginary part ( $\epsilon''$ ) of dielectric permittivity. Nevertheless, within this work the recorded data are transformed, via Equation (1), to the electric modulus formalism. Electric modulus is defined as the inverse quantity of complex permittivity:

$$M^* = \frac{1}{\epsilon^*} = \frac{1}{\epsilon' - j\epsilon''} = \frac{\epsilon'}{\epsilon'^2 + \epsilon''^2} + j \frac{\epsilon''}{\epsilon'^2 + \epsilon''^2} = M' + jM'' \quad (1)$$

where  $M'$  is the real and  $M''$  the imaginary part of electric modulus respectively.

This formalism is used because it excludes phenomena such as electrode polarization and space charge injection which lead to high values of permittivity and conductivity especially at high temperatures and low frequencies. Consequently, it allows the better representation of the MWS effect in the low frequency region. Extended arguments for the resulting benefits of this formalism are discussed elsewhere [12, 13].

$M'$  versus frequency as well as  $M''$  versus frequency, in the low temperature region (–100 to

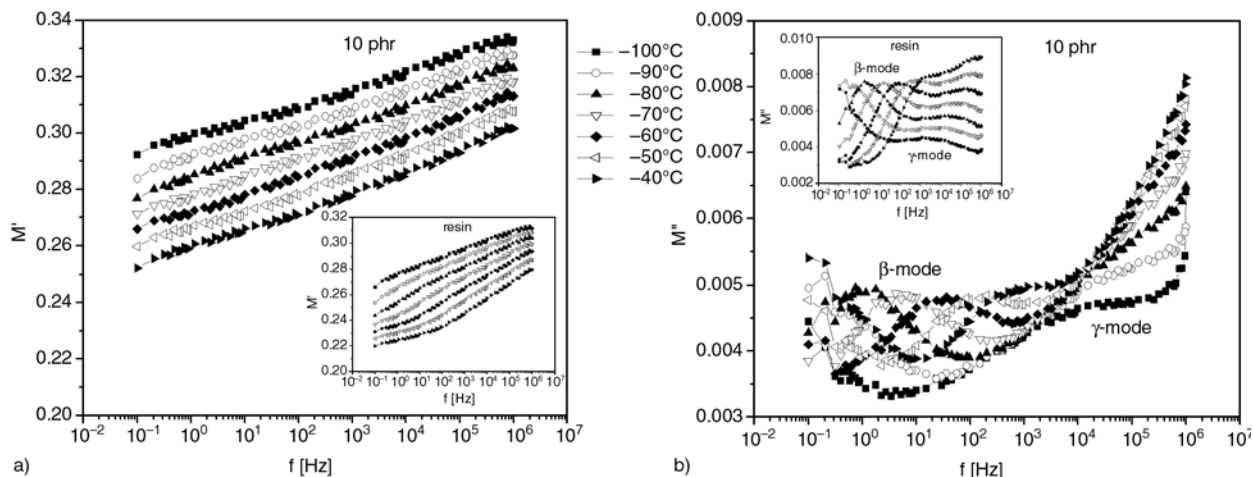


**Figure 1.** Real (a) and imaginary (b) part of electric modulus versus frequency for the specimen with 10 phr, in the low temperature region. Insert: Respective results for the pure epoxy specimen

–40°C), of the composite with 10 phr in TiO<sub>2</sub> are presented in Figures 1a and 1b respectively. Two, relatively weak, relaxation modes are recorded. These two relaxations are assigned as β- and γ-mode and they become evident via the corresponding loss peaks in the M'' spectrum. Both relaxations are originated from the pure resin, as shown in the insert of Figure 1, where the corresponding curves for the pure resin specimen, are presented. Moreover, since both processes are fast they are attributed to restricted local motions of the polymer chain i. e. re-arrangement of small parts of the polymer chain (γ-mode) and re-orientation of polar side groups (β-mode). The results suggest that the increase in concentration of ceramic TiO<sub>2</sub> slightly modifies the isothermal spectra of electric modulus. Specifically in the dielectric spectra, at low temperatures, of the composite with 10 phr in

TiO<sub>2</sub> only β-mode is clearly recorded. Elevated values of the imaginary part of electric modulus obstruct recording of the faster mechanism (γ-relaxation). Similar spectra, in the low temperature region, were obtained for the composites with 30 and 50 phr in TiO<sub>2</sub>.

### 3.2. High temperature region

Plots of M' versus frequency as well as M'' versus frequency, in the high temperature region (20 to 150°C), of the composite with 10 phr in TiO<sub>2</sub> are presented in Figures 2a and 2b respectively. In the high temperature region, the spectrum is dominated by the presence of α-mode. This mode, which is recorded in the same frequency range as in the case of the pure resin (insert of Figure 2) is related to the glass rubber transition of the polymer

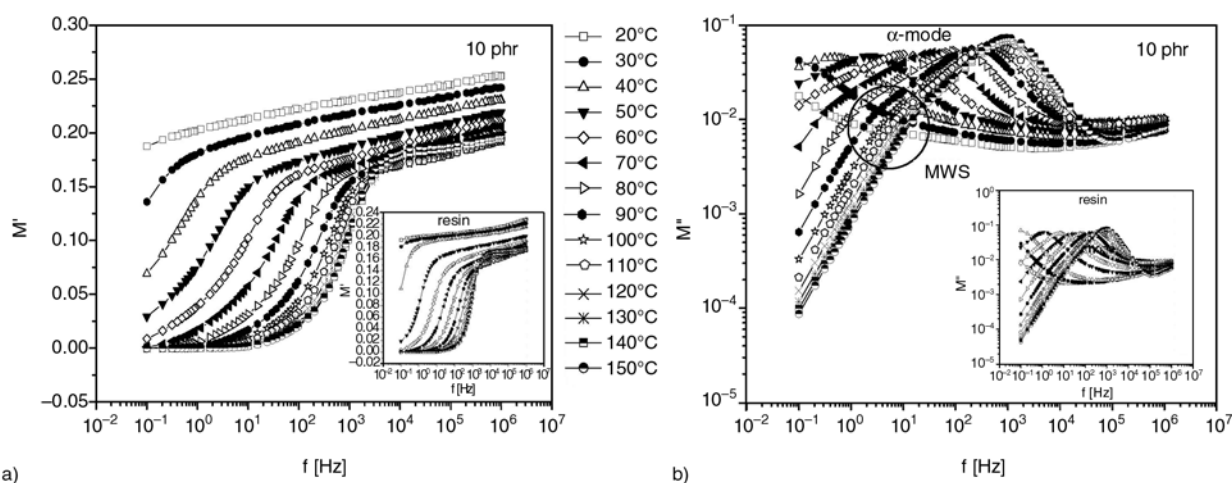


**Figure 2.** Real (a) and imaginary (b) part of electric modulus versus frequency for the specimen with 10 phr, at high temperatures. Insert: Respective results for the pure epoxy specimen

matrix. Peaks' position shifts to higher frequencies with increasing temperature, while the shape and magnitude of the formed peaks remain rather constant from 40 to 90°C. Above 90°C peaks' magnitude increases and the shift rate of maxima loci is reduced.

For the composite with 10 phr in TiO<sub>2</sub> an additional process, absent in the spectrum of pure resin, can be detected in the low frequency edge, below  $\alpha$ -relaxation. This process which is evident as a shoulder in the log-log spectra of  $M''$  (Figure 2b), at any given temperature, is slower than  $\alpha$ -relaxation. It is reasonable to suggest that interfacial phenomena are responsible for the occurrence of this mode. Interfacial polarization or MWS effect [14–16] is a relaxation process appearing in heterogeneous systems due to accumulation of charges at the interfaces of the system. The origin of these non-bounded charges arises from the stage of specimen preparation. At the matrix/particle interface charges form large dipoles, which are not able to follow simultaneously the alternation of the applied electric field. In the electric modulus presentation, the intensity of loss peaks is expected to decrease with increasing filler content. This becomes evident by simply comparing the results from the pure resin and those of the samples with 10 phr in TiO<sub>2</sub> (Figure 2b).

Pronounced MWS effect characterizes composite systems exhibiting high electrical heterogeneity between their phases. Typical examples of such systems are insulating matrix – conductive inclusions composites [17, 18]. The examined systems are consisting of titanium dioxide, which is a wide band gap semiconductor, and a typical insulating

thermoset polymer such as epoxy resin. Thus significant variation between the values of conductivity of the two constituent phases does not exist and consequently a remarkable MWS effect is not expected to occur. Dielectric spectra of Figure 2b are in accordance with previous remarks since only a weak interfacial polarization is recorded.

In the high frequency region, above  $\alpha$ -mode, another process is evident as a tail in the log-log spectra of composite with 10 phr in TiO<sub>2</sub>. The occurrence of this mode becomes more pronounced in composites with 30 and 50 phr in TiO<sub>2</sub> as shown in Figure 3.

In Figures 3a and 3b the imaginary part of electric modulus ( $M''$ ) versus frequency is plotted in a log-log representation, for the composites with 30 and 50 phr in TiO<sub>2</sub>, respectively. Both MWS effect and  $\alpha$ -mode are detected. The high frequency relaxation process which is absent in the dielectric spectrum of the pure matrix and not completely formed in the specimen with 10 phr, is now recorded. Thus the appearance of this process is strongly affected by the filler's concentration and should be attributed to the ceramic filler itself. Its location is intermediate in the dielectric spectra, lying between the fast (local modes) and the slow ( $\alpha$ -mode and MWS effect) processes, so for reasons of brevity, it would be called further on, as Intermediate Dipolar Effect (IDE).

### 3.3. AC electrical conductivity

The Alternating Current (AC) conductivity  $\sigma'$  of all samples has been calculated from the dielectric losses according to the Equation (2):

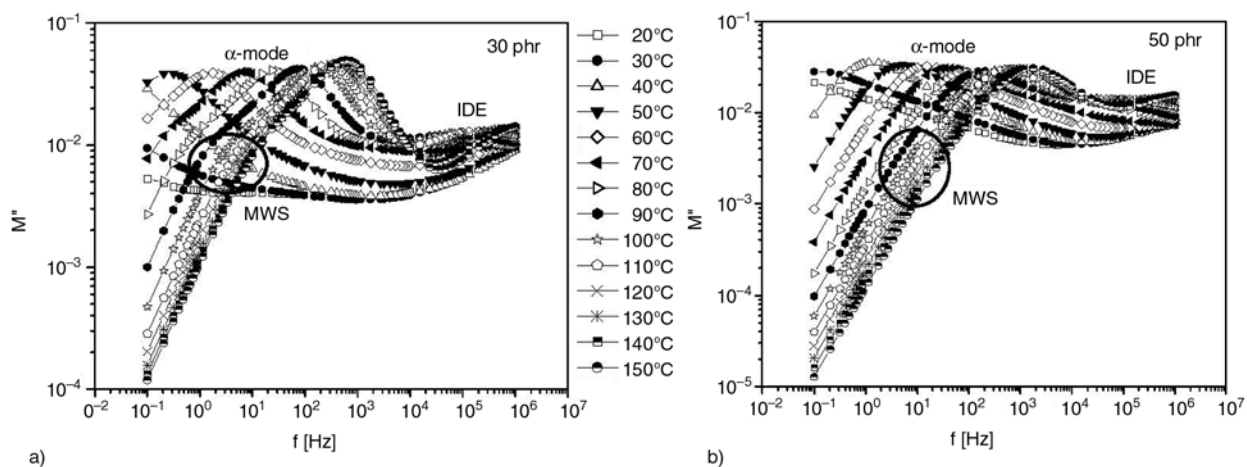


**Figure 3.** Imaginary part of electric modulus ( $M''$ ) versus frequency for the specimens with (a) 30 phr and (b) 50 phr in TiO<sub>2</sub>, at high temperatures

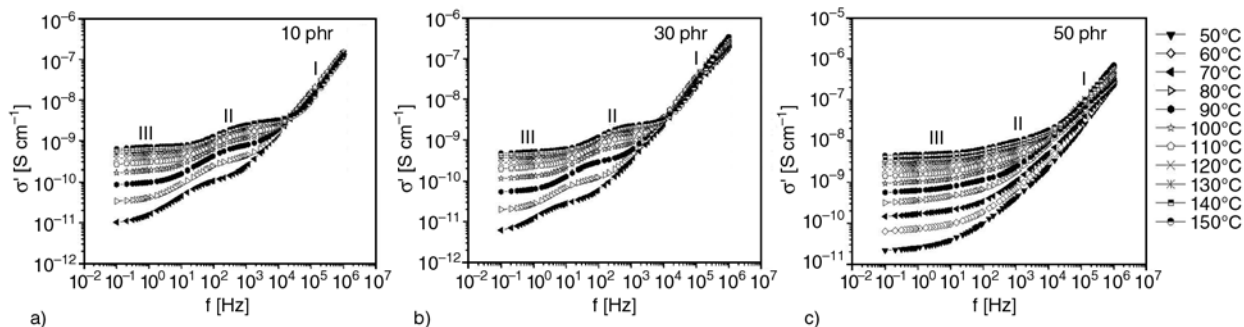


**Figure 4.** The real part of electrical conductivity ( $\sigma'$ ) versus frequency at elevated temperatures for composites with (a) 10 phr, (b) 30 phr and (c) 50 phr

$$\sigma' = \epsilon_0 \omega \epsilon'' \tag{2}$$

where  $\epsilon_0 = 8.85 \cdot 10^{-12}$  F/m is the permittivity of the free space and  $\omega = 2\pi f$  the angular frequency.

AC conductivity as a function of frequency is presented in Figure 4, at the high temperature region, for the composites with 10, 30 and 50 phr in  $\text{TiO}_2$ . For all the tested specimens an increase of conductivity  $\sigma'$  with temperature is observed especially at low frequencies. The dependence of electrical conductivity with frequency can be divided into distinct regions implying the existence of different dissipated effects [19]. In the high frequency region (I), conductivity increases with increasing frequency following the universal dielectric response law,  $\sigma' = A\omega^n$ , where  $n$  was found to be very close to 1. In this region a weak dependence of the conductivity with temperature is evident. In the low frequency region (III) a leveling off of the electrical conductivity is observed. This corresponds to the DC conductivity of the samples, which increases significantly with increasing temperature. In the intermediate region (II), dipolar relaxation

processes are present, the intensity of which is dependant upon filler content. Recalling dielectric data from Figures 2 and 3, two modes could be considered as responsible for the observed behaviour, in the specific region, namely MWS and  $\alpha$ -mode. However, in the AC conductivity formalism, resolve and quantification of the relative contributions can not be carried out.

#### 4. Discussion

Figure 5 provides isothermal plots of the imaginary part of the electric modulus ( $M''$ ) as a function of frequency, at two different temperatures, namely  $-80$  and  $120^\circ\text{C}$ , for the specimens with 10, 30 and 50 phr in  $\text{TiO}_2$  content.

In Figure 5a, both low temperature relaxation processes, namely  $\beta$ -mode and  $\gamma$ -mode, are evident in the specimen with 10 phr.  $\beta$ -mode is recorded in all tested samples and appears not to be influenced by the filler's concentration. On the contrary,  $\gamma$ -mode becomes weaker as the filler's concentration increases and is finally obstructed, in the spectra of 30 and 50 phr.

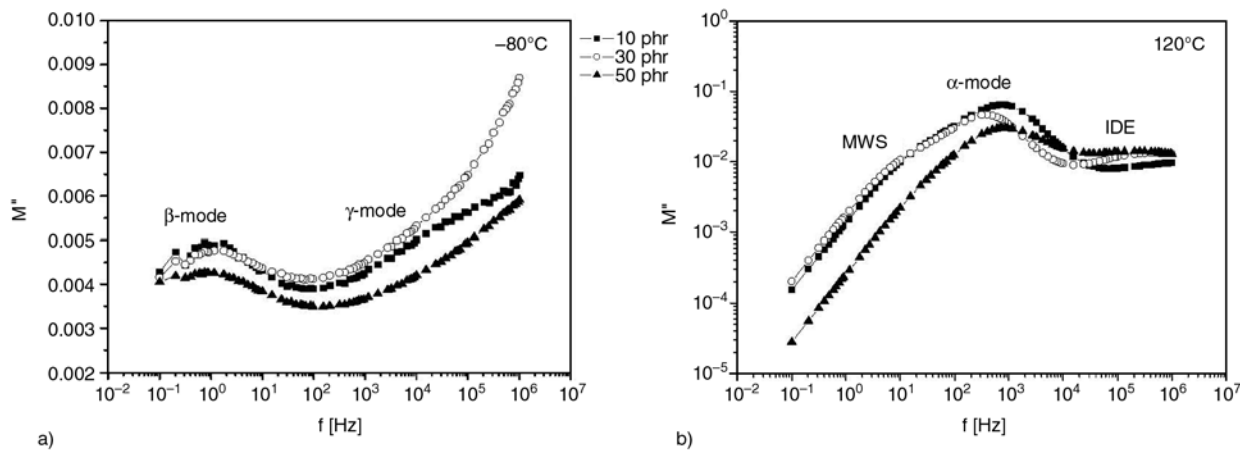


**Figure 5.** Imaginary part of electric modulus ( $M''$ ) versus frequency for all composites specimens at (a)  $-80^\circ\text{C}$  and (b)  $120^\circ\text{C}$

In Figure 5b,  $\alpha$ -mode is recorded in the middle of the frequency region forming a clear peak. The intensity of the peak is varies with filler's content. At the low and high frequency edges of the dielectric response spectra interfacial polarization phenomena (MWS effect) and IDE-mode are recorded respectively. IDE becomes stronger in the composites of 30 and 50 phr in  $\text{TiO}_2$ . The physical origin of IDE process cannot be ascribed unambiguously. The fact that it is detected in specimens with increased concentration of  $\text{TiO}_2$  implies that its source should be sought in the polarization effects of the ceramic filler.  $\text{TiO}_2$  is dielectrically anisotropic material, its unit cell attains tetragonal crystal structure and the static values of dielectric permittivity in the perpendicular and the lateral direction differ significantly [20]. Titanium oxide is classified as a polar oxide, exhibiting transitions between crystal structures with varying symmetry [21]. The local environment of the titanium sites in rutile is similar to that in barium titanate. The titanium site is surrounded by an octahedron of oxygen sites with a titanium-oxygen distance of  $\sim 2\text{\AA}$  [20]. The low symmetry of the unit cell of titanium dioxide, at room temperature, and the similarities to barium titanate is a strong indication that spontaneous polarization might be occurring in  $\text{TiO}_2$ . In that case, polarization effects might be relaxing under the influence of an external alternating electric field. The influence of temperature upon the distance of sites in the unit cell of  $\text{TiO}_2$  might assert a more symmetrical structure, where the redistribution of polarizabilities will produce zero net polarization. If so, a disorder to order, or in other words ferroelectric to paraelectric transition will take place at a critical temperature. However, in order to verify these initial indications more experimental work is necessary to be carried out.

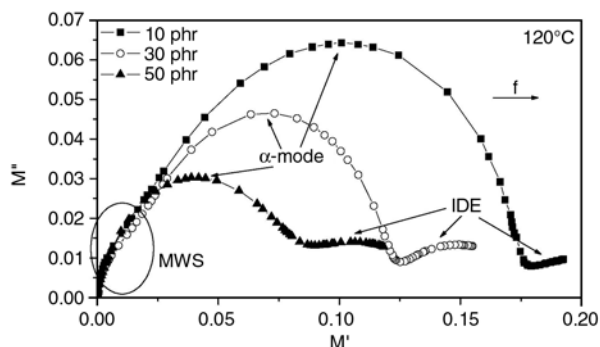


**Figure 6.** Cole-Cole plots for all composite specimens at  $120^\circ\text{C}$

The high temperature relaxation processes are also shown in the Cole-Cole representation of Figure 6. Apart from the semicircle corresponding to  $\alpha$ -mode, MWS relaxation is also present in the low frequency edge. This fact is demonstrated by the asymmetry of the respective curves in the low frequency region where a hump is observed. The coincidence of the beginning of semicircles with the origin of the graph is a clear indication that no other relaxation process is present, at lower frequencies, in all studied composite systems. Moreover, the variation of the semicircles radius, corresponding to the  $\alpha$ -mode, indicates that  $\alpha$ -mode is influenced by the filler's concentration. Furthermore, at the high frequency end, experimental results from the composites with 30 and 50 phr contents in  $\text{TiO}_2$  form a suppressed semicircle reflecting the presence of IDE-mode.

Aiming to analyze the contribution of the three mechanisms, which are present at elevated temperatures, curves of  $\log M''$  versus  $\log f$  are fitted using a multi-peak fitting procedure. As an example, the fitting procedure employed for the specimen with 30 phr in  $\text{TiO}_2$  is shown in Figure 7. The experimental data are fitted using, as first approximation, three Debye-type processes. The experimental data are satisfactorily described by the solid line which is a superposition of the three Debye-type relaxation processes corresponding to each of the experimentally determined modes (dashed lines). Debye-type processes are characterized by a single relaxation time, which can be easily evaluated by the abscissa of loss maxima. Obtained results are given in Table 1. The influence of the filler content on relaxation dynamics, as expressed by the evalu-

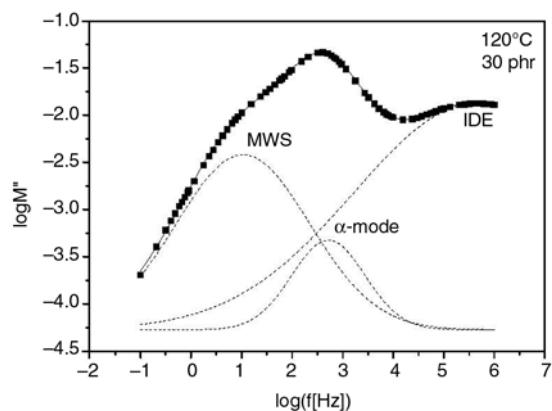


**Figure 7.** Fitting procedure for the composite with 30 phr in  $\text{TiO}_2$  at  $120^\circ\text{C}$ . The experimental data are fitted via the superposition of three Debye-type processes

**Table 1.** Evaluated relaxation times at 120°C

Sample	$\tau$ [ms]		
	MWS	$\alpha$ -mode	IDE
Epoxy + 10 phr TiO <sub>2</sub>	45.31	0.15	–
Epoxy + 30 phr TiO <sub>2</sub>	7.76	0.29	0.2·10 <sup>-3</sup>
Epoxy + 50 phr TiO <sub>2</sub>	0.49	0.22	0.03·10 <sup>-3</sup>

ated relaxation times, appears to be more pronounced in the MWS and IDE effects. In both cases relaxation times decrease with increasing filler’s content, implying that both processes are facilitated with the increase of TiO<sub>2</sub> content. Taking into account the frequency-temperature superposition it can be concluded that MWS and IDE effects appear at lower temperature range as the TiO<sub>2</sub> content increases. On the other hand the relaxation times of  $\alpha$ -mode do not show any particular trend with the variation of filler’s content. However, the validity of this conclusion is limited since the glass/rubber relaxation process deviates from a pure Debye mechanism.

The temperature dependence of loss peak position for all the examined systems and for all three relaxation processes at elevated temperatures is depicted in Figure 8. MWS and IDE modes exhibit an Arrhenius type behaviour in all concentrations according to the Equation (3):

$$f_{max} = f_0 \exp\left(-\frac{E_A}{k_B T}\right) \quad (3)$$

where  $f_0$  is a pre-exponential factor,  $E_A$  the activation energy,  $k_B$  the Boltzmann constant, and  $T$  the temperature in K. The temperature dependence of

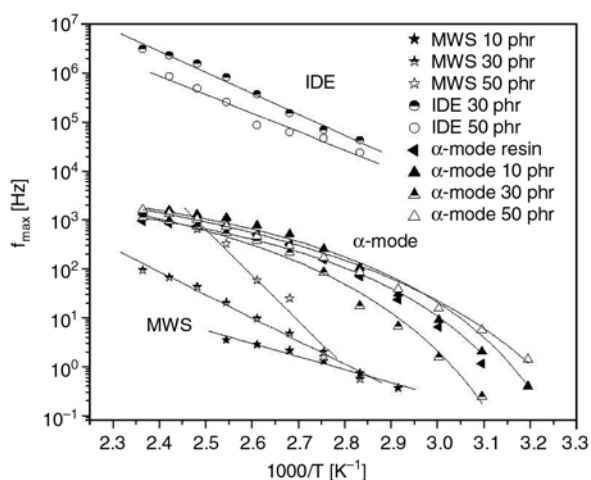


**Figure 8.** The dependence of relaxation frequencies with the reciprocal temperature at elevated temperatures, for all measured samples

**Table 2.** Activation energies and VTF parameters for all the tested specimens

	MWS	$\alpha$ -mode		IDE
	E <sub>A</sub> [eV]	T <sub>0</sub> [K]	B [K]	E <sub>A</sub> [eV]
Epoxy	–	280	395	–
Epoxy + 10 phr TiO <sub>2</sub>	0.53	275	430	–
Epoxy + 30 phr TiO <sub>2</sub>	0.94	280	545	0.85
Epoxy + 50 phr TiO <sub>2</sub>	1.86	285	595	0.75

$\alpha$ -relaxation can be described by the Vogel-Tamann-Fulcher equation (4) [22–24]:

$$f_{max} = f_0 \exp\left(-\frac{B}{T - T_0}\right) \quad (4)$$

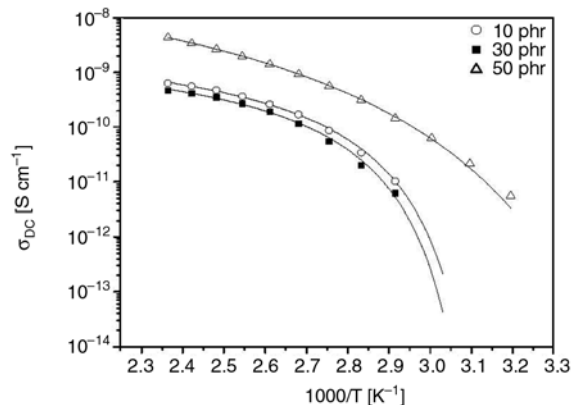
where  $f_0$  is a pre-exponential factor,  $B$  a constant (being a measure of the activation energy), and  $T_0$  Vogel temperature or ideal glass transition temperature. This equation considers that relaxation rate increases rapidly at lower temperatures because of the reduction of free volume.

Table 2 summarizes the obtained results for the activation energies of MWS and IDE effects as well as the VTF parameters  $T_0$  and  $B$ .

The dependence of the Direct Current (DC) electrical conductivity  $\sigma_{DC}$  ( $\sigma'$  at 0.1 Hz) with reciprocal temperature is shown in Figure 9 for all the composites. DC conductivity remains rather constant for composites with 10 and 30 phr. This is not a surprising behaviour taking into account the insulating nature of both the inclusion and the matrix. A slight increase is observed only for the composite with 50 phr.

DC conductivity values follow the Vogel-Tamann-Fulcher equation (5):

$$\sigma_{DC} = \sigma_0 \exp\left(-\frac{B}{T - T_0}\right) \quad (5)$$



**Figure 9.** DC electrical conductivity as a function of reciprocal temperature

**Table 3.** VTF parameters concerning the temperature dependence of DC conductivity at the examined composites

	<b>B [K]</b>	<b>T<sub>0</sub> [K]</b>
Epoxy + 10 phr TiO <sub>2</sub>	196	306
Epoxy + 30 phr TiO <sub>2</sub>	188	313
Epoxy + 50 phr TiO <sub>2</sub>	569	259

where  $\sigma_0$  pre-exponential factor,  $B$  a parameter related to the activation energy and  $T_0$  is the Vogel temperature. The experimental data are satisfactorily fitted by VTF equation (solid lines) and fitting parameters are listed in Table 3.

#### 4. Conclusions

The dielectric response of polymer composites consisting of an epoxy resin matrix and rutile TiO<sub>2</sub> ceramic filler has been studied in the frequency range 0.1 Hz–1 MHz and temperatures from –100 to 150°C. The relaxation phenomena recorded include contributions from both the polymeric matrix and the reinforcing phase. At low temperatures, two distinct relaxation processes, namely  $\beta$ - and  $\gamma$ -mode, were detected in all composites and originate from the pure resin. Both dielectric processes are attributed to local motions resulting from reorientations of polar side groups and small segments of the polymer chain. At high temperatures three additional relaxation processes were detected. From lower to higher frequencies at constant temperature, they are attributed to interfacial polarization phenomena (MWS effect), glass/rubber transition, and to relaxing polarization (IDE) of the TiO<sub>2</sub> ceramic particles respectively. MWS effect becomes stronger with increasing filler's concentration and IDE becomes more pronounced at the concentrations of 30 and 50 phr in TiO<sub>2</sub>. MWS and IDE relaxations exhibit an Arrhenius type dependence with temperature while  $\alpha$ -mode follows VTF model. Relaxation times and activation energies for all high temperature modes were calculated. The DC electrical conductivity of all samples was evaluated at 0.1 Hz, where a leveling off of the corresponding curves is observed at the relatively high temperatures. DC electrical conductivity increases with increasing temperature following the VTF model. Finally, the existence of a self-relaxing polarization mechanism in ceramic

TiO<sub>2</sub> composites can be exploited for the design of functional polymer matrix systems.

#### Acknowledgments

This work was partially supported by the General Secretariat for Research and Technology (GSRT) of Greece in the framework of Joint Research and Technology Programs between Greece and Tunisia (project code 121-e).

#### References

- [1] Chahal P., Tummala R. R., Allen M. G., Swaminathan M.: A novel integrated decoupling capacitor for MCM-L technology. *IEEE Transactions on Components Packaging and Manufacturing Technology, Part B: Advanced Packaging*, **21**, 184–193 (1998).
- [2] Dias C. J., Igreja R., Marat-Mendes R., Inacio P., Marat-Mendes J. N., Das-Gupta D. K.: Recent advances in ceramic-polymer composite electrets. *IEEE Transactions on Dielectrics and Electrical Insulation*, **11**, 35–40 (2004).
- [3] Bai Y., Cheng Z.-Y., Bharti V., Xu H. S., Zhang Q. M.: High-dielectric-constant ceramic-powder polymer composites. *Applied Physics Letters*, **76**, 3804–3806 (2000).
- [4] Bhuvanesh N. S. P., Gopalakrishnan J.: Solid-state chemistry of early transition-metal oxides containing d<sup>0</sup> and d<sup>1</sup> cations. *Journal of Materials Chemistry*, **7**, 2297–2306 (1997).
- [5] Linsebigler A. L., Lu G., Yates J. T.: Photocatalysis on TiO<sub>2</sub> surfaces: Principles, mechanisms, and selected results. *Chemical Reviews*, **95**, 735–758 (1995).
- [6] Oehrlein G. S.: Oxidation temperature-dependence of the DC electrical-conduction characteristics and dielectric strength of thin TA205 films on silicon. *Journal of Applied Physics*, **59**, 1587–1595 (1986).
- [7] Varma I. K., Gupta V. G.: Thermosetting resin-properties. In: 'Comprehensive Composite Materials' (eds.: Talreja R., Manson J-A. E., Kelly A., Zweben C.) Elsevier, Amsterdam, Vol 2, chapter 2.01, p. 2–18 (2000).
- [8] Hull D., Clyne T. W.: An introduction to composite materials. Cambridge University Press, Cambridge (1996).
- [9] Daniel I. M., Ishai O.: Engineering mechanics of composite materials. Oxford University Press, Oxford (1994).
- [10] Schwartz M. M.: Composite materials handbook. McGraw-Hill, New York (1984).
- [11] Ellis B.: Chemistry and technology of epoxy resins. Blackie Academic and Professional, London (1993).

- [12] Tsangaris G. M., Psarras G. C., Kouloumbi N.: Electric modulus and interfacial polarization in composite polymeric systems. *Journal of Materials Science*, **33**, 2027–2037 (1998).
- [13] Psarras G. C., Manolakaki E., Tsangaris G. M.: Electrical relaxations in polymeric particulate composites of epoxy resin and metal particles. *Composites, Part A: Applied Science and Manufacturing*, **33**, 375–384 (2002).
- [14] Macedo P. B., Moynihan C. T., Bose R.: The role of ionic diffusion in polarization in vitreous ionoc conductors. *Physics and Chemistry of Glasses*, **13**, 171–179 (1972).
- [15] Bakr A. A., North A. M.: Charge carriers hopping in poly(arylenevinyl-enes). *European Polymer Science*, **13**, 799–803 (1977).
- [16] Starkweather H. W., Avakian P.: Conductivity and electric modulus in polymers. *Journal of Polymer Science, Part B: Polymer Physics*, **30**, 637–641 (1992).
- [17] Tsangaris G. M., Psarras G. C.: The dielectric response of a polymeric three-component composite. *Journal of Materials Science*, **34**, 2151–2157 (1999).
- [18] Psarras G. C., Manolakaki E., Tsangaris G. M.: Dielectric dispersion and ac conductivity in-iron particles loaded-polymer composites. *Composites, Part A: Applied Science and Manufacturing*, **34**, 1187–1198 (2003).
- [19] von Hippel A. R.: *Dielectrics and waves*. Artech House, Boston (1995).
- [20] Parker R. A.: Static dielectric constant of rutile (TiO<sub>2</sub>), 1.6-1060K. *Physical Review*, **124**, 1719–1722 (1961).
- [21] Kim J. Y., Jung H. S., No J. H., Kim J. R., Hong K. S.: Influence of anatase-rutile phase transformation on dielectric properties of sol-gel derived TiO<sub>2</sub> thin films. *Journal of Electroceramics*, **16**, 447–451 (2006).
- [22] Vogel H.: Das Temperaturabhängigkeitgesetz der Viskosität von Flüssigkeiten. *Zeitschrift für Physik*, **22**, 645–646 (1921).
- [23] Tammann G., Hesse W.: Die Abhängigkeit der Viskosität von der Temperatur bei unterkühlten Flüssigkeiten. *Zeitschrift für Anorganische und Allgemeine Chemie*, **156**, 245–257 (1926).
- [24] Fulcher G. S.: Analysis of recent measurements of the viscosity of glasses. *Journal of the American Ceramic Society*, **8**, 339–355 (1925).

# Hot consolidated all-PP composites from textile fabrics composed of isotactic PP filaments with different degrees of orientation

A. Izer, T. Bárány\*

Department of Polymer Engineering, Faculty of Mechanical Engineering, Budapest University of Technology and Economics, H-1111 Budapest, Műegyetem rkp. 3., Hungary

Received 27 July 2007; accepted in revised form 29 September 2007

**Abstract.** Self-reinforced polypropylene composites (SRPPC) were hot pressed from textile layers (carded mat, knitted fabrics) at three different temperatures (160, 165 and 170°C) by setting a constant pressure (6 MPa) and constant holding time (2 min). Both textiles consist of two kinds of isotactic polypropylene (iPP) fibers differing in their orientation. In these compositions the highly oriented iPP works as reinforcement and the less oriented one fulfills the role of the matrix after hot consolidation. Two textile assemblies, viz. carded (also needle punched) mats and knitted fabrics were hot pressed; and the properties of the resultant SRPPC plates were investigated under tensile and falling weight impact conditions. The microstructure of the SRPPC was analyzed by light microscopy using polished sections and by SEM using cut surfaces.

**Keywords:** *polymer composites, self-reinforcement, consolidation, textile fabric, polypropylene*

## 1. Introduction

Nowadays the most frequently used reinforcement in the automotive industry is glass fiber (GF) – applied mainly in polypropylene (PP) and polyamide (PA) matrices. In spite of the excellent mechanical properties of glass fiber reinforced polymer composites, the main disadvantage is their limited recyclability. The importance of recycling forced the researchers to develop more environment-friendly solutions. Self-reinforced polymer composites (SRPC) tend to be one of the best choices, so the research and the development of these composites is an extensively studied topic nowadays. SRPCs are composed of reinforcing fabrics made of highly oriented technical fibers and a matrix material. Recall that they are of the same polymer. The key issue of their manufacturing is to find a suitable processing window that ensures that the reinforcing fibers do not melt (or only partially)

and the matrix wets them out accordingly [1–4]. The focus of many research works is to widen this window. In case of SRP composites, three concepts are used. The first technique is hot compaction, where the outer layer of the fibers melts and recrystallizes as a matrix in a suitable temperature and pressure range [1, 5, 6]. The second one is co-extrusion, where a thin layer with lower melting temperature is co-extruded with a highly oriented, thicker core, and these bands are textile structured and hot consolidated [2, 7–9]. Finally, there is the film-stacking method, where the matrix and reinforcement layers are laminated onto each other and are hot pressed [3, 4, 10, 11]. In case of the film-stacking method, the material selection and combination is more flexible and the composite production can also be made continuously by using a double belt press. In case of the latter two methods the melting temperature difference (20–30°C; in case of PP) can be

\*Corresponding author, e-mail: [barany@pt.bme.hu](mailto:barany@pt.bme.hu)  
© BME-PT and GTE

reached if random PP copolymer/isotactic PP (iPP) [2, 3, 7–12]; beta polymorph of iPP/iPP fiber [4] combinations are used. Furthermore, the processing window is narrower (7–8°C) if various iPP fibers having different stretching ratios (orientation degrees) are used. As far as we know there are no studies on the manufacturing of SRPCs exploiting the last mentioned possibility. Therefore, our aim is to investigate the hot consolidation of carded (and needle punched) mats and knitted fabrics. Both textiles consist of two kinds of oriented iPP fibers. In these compositions the highly oriented material should work as reinforcement and the less oriented one should fulfill the role of the matrix after hot pressing. The textile layers were hot consolidated (hot pressed) at three different temperatures (160, 165 and 170°C) at constant pressure (6 MPa) and for constant holding time (2 min). Tensile and instrumented falling weight impact test were performed on the composite sheets.

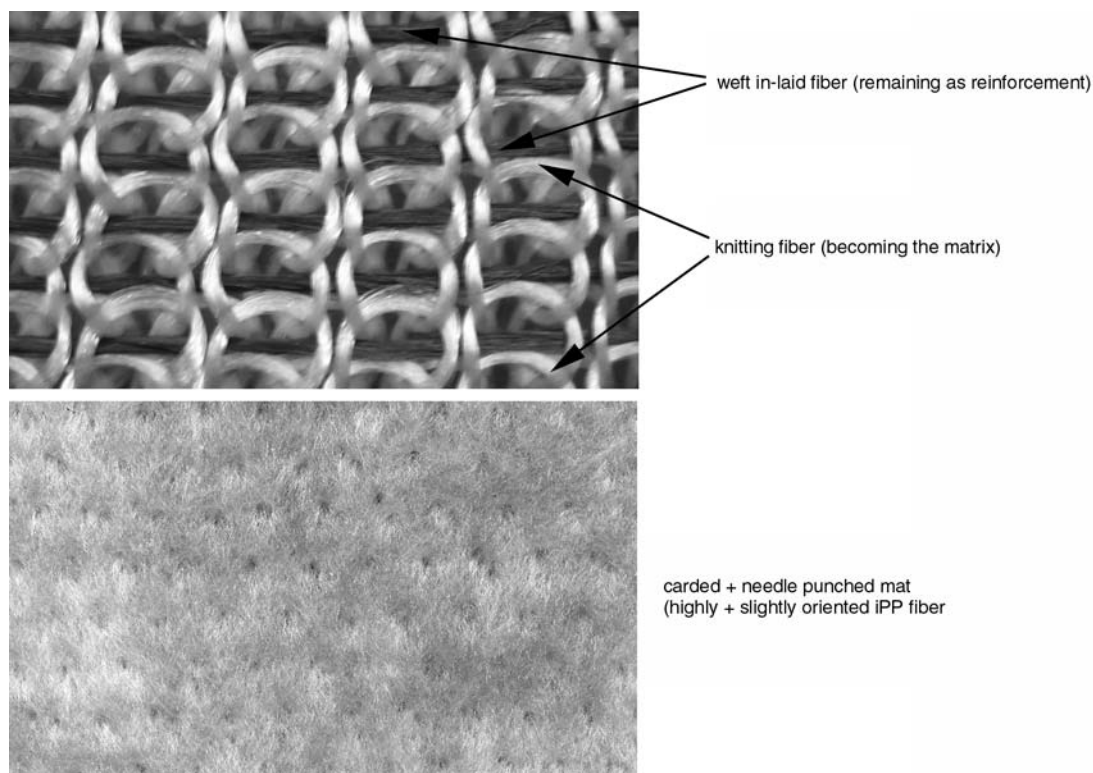
## 2. Experimental

### 2.1. Materials and their processing

Slightly oriented iPP fiber produced by Sopilén Ltd. (Sopron, Hungary) was used as the matrix and highly oriented iPP fibers manufactured by

Stradom S.A. (Czestochowa, Poland) as the reinforcement. Tensile test (100 mm/min, 23°C) and differential scanning calorimetry tests (10°C/min) were performed on the single fibers. The related results are listed in Table 1. In this study we mark the reinforcing fibers as highly oriented and the matrix fiber as slightly oriented. Although, we have no information about the degree of orientation but from the testing results (single fiber) this characteristic can be concluded. Note that the observed difference in the melting temperatures ensures the targeted manufacturing of self reinforced polypropylene composites (SRPPC).

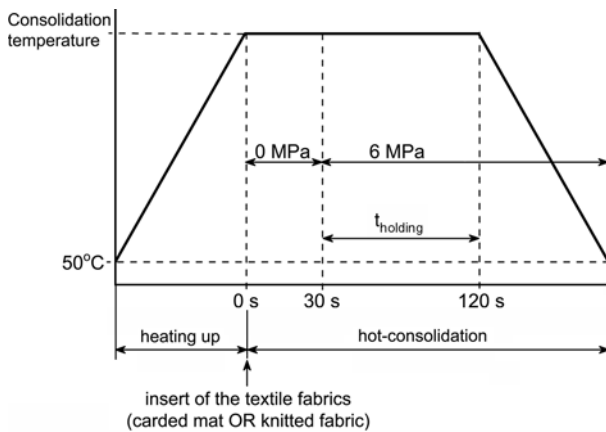
Two different textile fabrics were used for SRPPC sheets. (i) Plain weft knitted fabric (becoming the matrix) with in-laid iPP fiber reinforcement was prepared from the fibers (cf. Figure 1). Note that the reinforcing contents were set to be 24 and 38 wt% determined by the nominal weight of the reinforcing fibers used. (ii) Chopped ( $\approx 80$  mm) matrix giving and as reinforcement working fibers were carded and needle punched together as described in details in Ref. [12] (hereafter referred to as: carded – it is shown on Figure 1). The identical textile layers (in case of knitted 8, in case of carded 4 plies) were placed on each other by keeping the reinforcement alignment constant; therefore



**Figure 1.** The scheme of the plain weft knitted fabric with in-laid iPP fiber reinforcement (hereafter referred to as: knitted fabric) and carded and needle punched mat

**Table 1.** The properties of the matrix and reinforcing fibers

Fiber	Tensile strength [MPa]	Tensile modulus [GPa]	Average diameter [ $\mu\text{m}$ ]	Melting temperature (1 <sup>st</sup> run) [ $^{\circ}\text{C}$ ]	Melting temperature (2 <sup>nd</sup> run) [ $^{\circ}\text{C}$ ]
Reinforcing fiber (2200 dtex, white) for knitted fabric and carded mat	$465 \pm 32$	$3.7 \pm 0.3$	$40.2 \pm 1.8$	178.9	165.7
Reinforcing fiber (1200 dtex, black) for knitted fabric	$440 \pm 42$	$3.9 \pm 0.4$	$40.3 \pm 3.6$	178.4	164.2
Matrix fiber (600 dtex, white) for carded mat	$89 \pm 11$	$0.9 \pm 0.1$	$58.4 \pm 3.7$	170.5	165.5
Matrix fiber (2100 dtex, white) for knitted fabric	$148 \pm 25$	$1.9 \pm 0.3$	$45.5 \pm 3.0$	171.0	163.4

**Figure 2.** The parameters of the composite processing (consolidation)

the resulting composite plates are of anisotropic nature. These packages were consolidated by hot pressing at three different temperatures (160, 165 and  $170^{\circ}\text{C}$ ) at constant pressure (6 MPa) and for constant holding time (2 min). The detailed settings of the hot pressing process are shown in Figure 2. The thickness of the manufactured composite sheets is approximately 3 mm.

## 2.2. Specimens and their testing

The consolidation quality was studied on polished cross sections of the SRPPC sheets via reflection light microscopy (LM; Olympus BX51M).

The cut surface of the specimens was inspected in a scanning electron microscope (SEM; JEOL 6380 LA, Japan) after sputtering with Au/Pd alloy.

Static tensile and dynamic falling weight impact tests were performed on the manufactured composite sheets. The tensile tests were done on a universal ZWICK Z020 testing machine according to standard EN ISO 527. Tensile strength was determined from the tests results. Instrumented falling weight impact (IFWI) tests were performed on a

Fractovis 3789 (Ceast, Italy) machine with the following settings: maximal energy: 229.05 J; diameter of the dart: 20 mm; diameter of the support rig: 40 mm; weight of the dart: 23.62 kg and drop height: 1 m. IFWI specimens were quadratic, with a size of  $70 \times 70 \text{ mm}^2$ . Each test was performed at room temperature ( $23^{\circ}\text{C}$ ), in weft (for knitted fabric) and fiber direction (for carded mat).

## 3. Results and discussion

### 3.1. Microstructure characterization

Figures 3 and 4 show the LM pictures of the polished cross section of the hot consolidated knitted fabric (24.3 wt%; 160 and  $170^{\circ}\text{C}$ ) and carded (30, 50 and 70 wt%; 160 and  $170^{\circ}\text{C}$ ). Figures 3 and 4 reveal that the matrix fibers have melted partially at  $160^{\circ}\text{C}$ , while continuous matrix can be detected at the processing temperature of  $170^{\circ}\text{C}$ . For carded mat-based SRPPCs the reinforcing fibers distribute well in case of 30 wt% at each temperature but as the reinforcing fiber content increases, significant segregation of fibers can be seen and the fibers are distributed more homogeneously only at the highest temperature ( $170^{\circ}\text{C}$ ).

Figure 5 shows the SEM (magnification of  $100\times$ ) pictures of the cut surface of the SRPPCs produced from the knitted fabric (38.2 wt%) and Figure 6 displays SEM pictures (magnification of  $100\times$ ) of the cut surface of the SRPPCs produced from the carded mat (50 wt%) manufactured at 160 and  $170^{\circ}\text{C}$ , respectively. In both cases it can be seen well that with increasing processing temperature, the matrix fibers melted to a greater extent, hence consolidation improved. In other words, with increasing processing temperature, the matrix wets the reinforcing fibers more and better adhesion can be supposed.

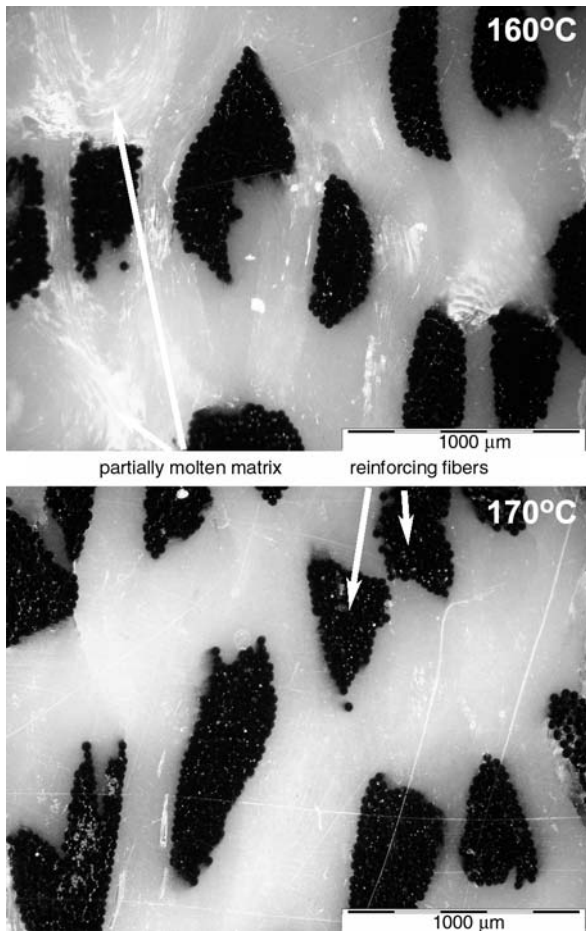


**Figure 3.** Light microscopic pictures of the polished cross section of the hot consolidated knitted fabric (nominal reinforcing content: 24.3 wt%) manufactured at 160 and 170°C

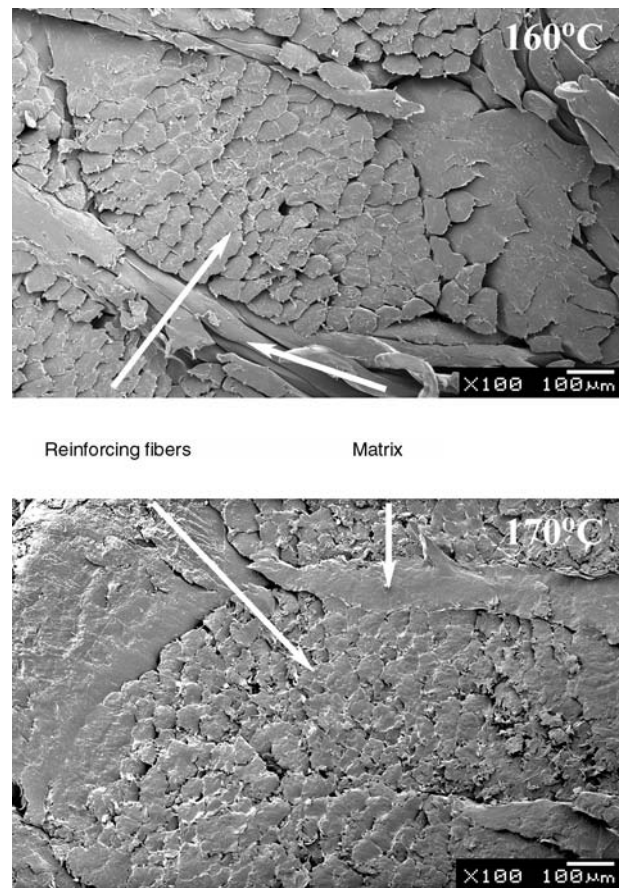


**Figure 5.** Scanning electron microscopic pictures of the cut cross section of the hot consolidated (at 160 and 170°C) knitted fabric (nominal reinforcing content: 38.2 wt%)

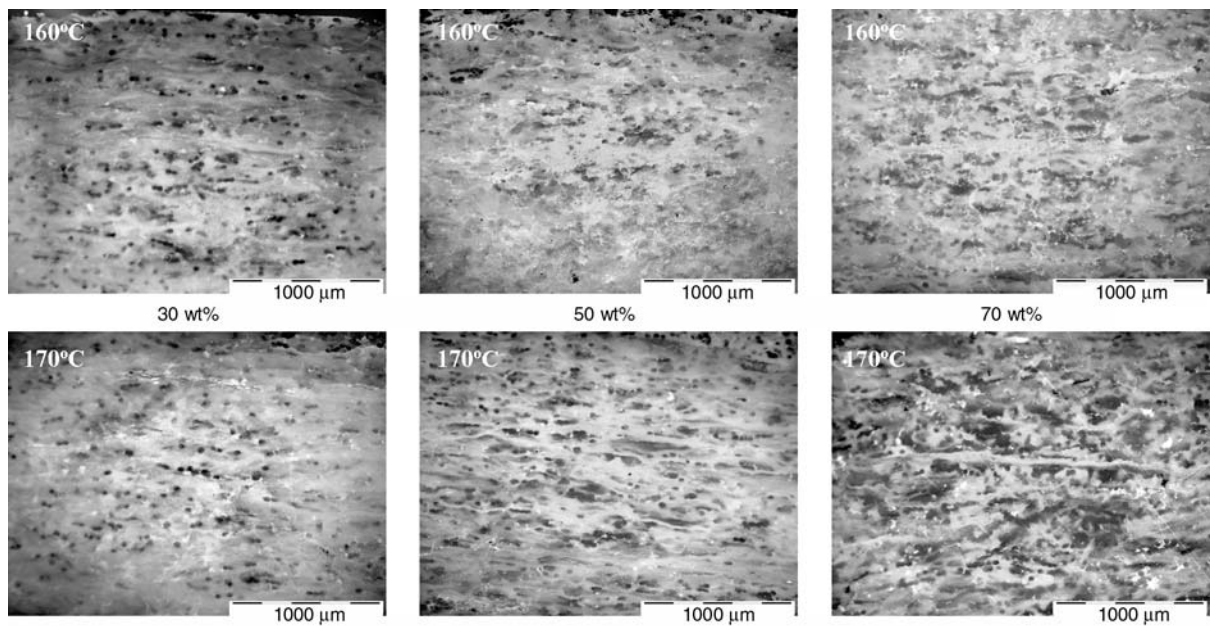


**Figure 4.** Light microscopic pictures of the polished cross section of the hot consolidated carded mat (nominal reinforcing content: 30, 50 and 70 wt%) manufactured at 160 and 170°C

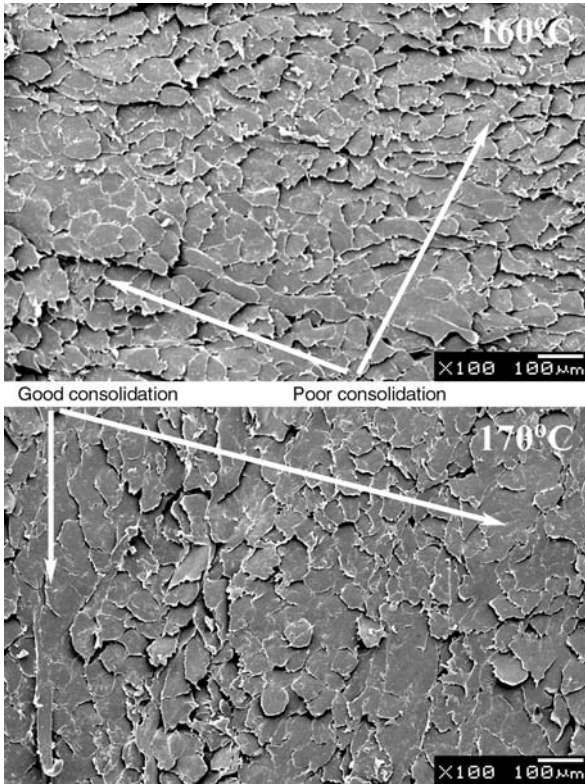


Figure 6. Scanning electron microscopic pictures of the cut cross section of the hot consolidated (at 160 and 170°C) carded mat (nominal reinforcing content: 50 wt%)

### 3.2. Static and dynamic tests

The results of the mechanical tests are listed in Table 2. Figures 7 and 8 show the tensile strength as a function of the processing temperature for knitted fabrics and carded mat-based SRPPCs, respectively. For both structures, as expected, the tensile

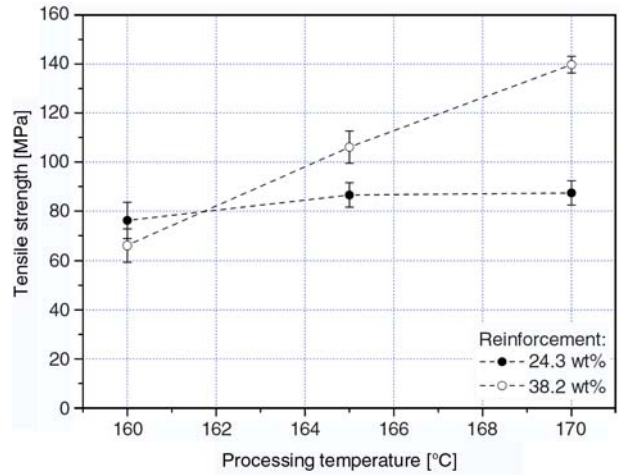


Figure 7. Tensile strength vs. processing temperature determined on the hot consolidated knitted fabrics

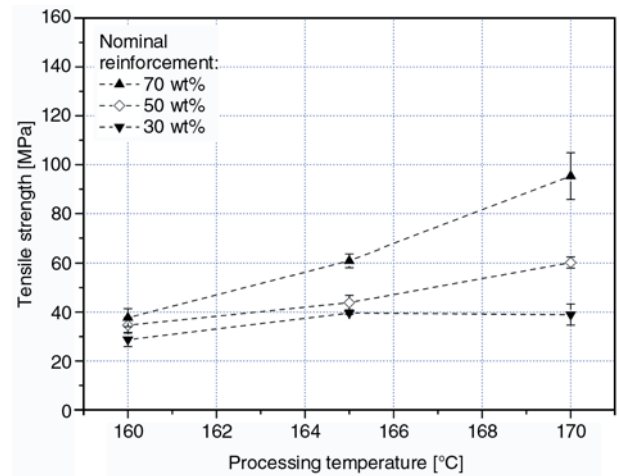


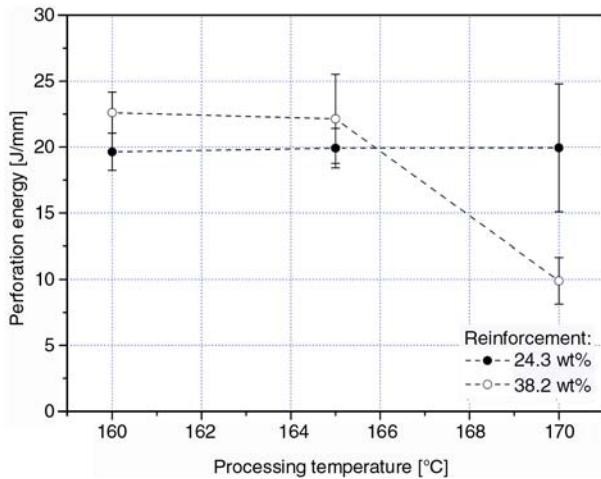
Figure 8. Tensile strength vs. processing temperature determined on the hot consolidated carded mat

Table 2. Mechanical properties of the manufactured composites

Composite build-up	Nominal fiber content [wt%]	Consolidation temperature [°C]	Tensile strength [MPa]	Tensile modulus [MPa]	Perforation energy [J/mm]
Knitted (black reinforcing fiber)	24.3	160	76.2 ± 7.4	2391 ± 244	19.6 ± 1.4
		165	86.6 ± 5.0	2269 ± 85	19.9 ± 1.5
		170	87.4 ± 5.0	2513 ± 46	19.9 ± 4.9
Knitted (white reinforcing fiber)	38.2	160	66.1 ± 6.7	2311 ± 156	22.6 ± 1.6
		165	106.1 ± 6.6	2353 ± 57	22.1 ± 3.4
		170	139.7 ± 3.4	2486 ± 55	9.9 ± 1.7
Carded (white reinforcing fiber)	30	160	28.8 ± 2.9	2131 ± 74	18.4 ± 2.5
		165	39.6 ± 0.5	2159 ± 40	16.1 ± 0.8
		170	39.0 ± 4.3	2161 ± 10	15.1 ± 2.4
Carded (white reinforcing fiber)	50	160	34.6 ± 3.2	2247 ± 83	20.0 ± 4.2
		165	43.9 ± 3.0	2218 ± 59	18.4 ± 3.5
		170	60.3 ± 2.3	2480 ± 68	11.6 ± 2.2
Carded (white reinforcing fiber)	70	160	37.7 ± 3.7	2425 ± 90	25.1 ± 1.2
		165	60.9 ± 2.8	2387 ± 99	20.4 ± 0.5
		170	95.4 ± 9.6	2837 ± 62	16.3 ± 2.7

strength increases with increasing processing temperature and with increasing reinforcing fiber content. According to our earlier studies [4, 11, 12] the tensile parameters (strength, modulus) decreased at temperatures higher than 170°C owing to the relaxation and partial melting of the reinforcing fibers. So, in our present study we have focused on the processing temperature range of 160–170°C. For better consolidation of the increasing reinforcing fiber content, matrix material having lower viscosity is demanded which is the result of the higher temperature. Therefore the tensile parameters depends more on the processing temperature with increasing reinforcement ratio.

Figures 9 and 10 show the perforation energy vs. processing temperature for knitted fabrics and carded mat-based SRPPCs, respectively. In case of carded mat-based SRPPCs – as expected – the per-



**Figure 9.** Perforation energy vs. processing temperature determined on the hot consolidated knitted fabrics

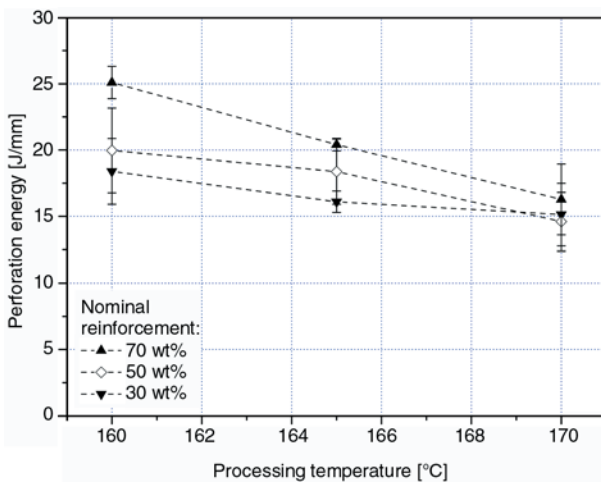


**Figure 10.** Perforation energy vs. processing temperature determined on the hot consolidated carded mat

foration energy decreases – especially at higher reinforcement content – with increasing processing temperature content, and this refers to the improvement of consolidation. Note that the poorly consolidated system absorbs higher energy up to the failure than the better consolidated one. This can be advantageous for special applications. The results of IFWI tests performed on knitted fabric-based SRPPC sheets are twofold. First, the values are as high as for carded-based SRPPCs with significant deviation. Second, the typical failure of these specimens (knitted fabric-based) is the total pull out of the in-laid reinforcing fibers and at the highest processing temperatures the specimen tears at the whole length along the in-laid reinforcing fibers (in weft direction) (Figure 11), even at increased specimen dimensions (90×90 mm). In case of carded-based SRPPC specimens (IFWI) the same behavior was experienced as in our earlier studies [4, 11]: when the composite is consolidated at lower processing temperature, massive delamination took place while the SRPPC sheets produced at higher processing temperature are less prone to delamination but exhibited markedly lower energy dissipation.

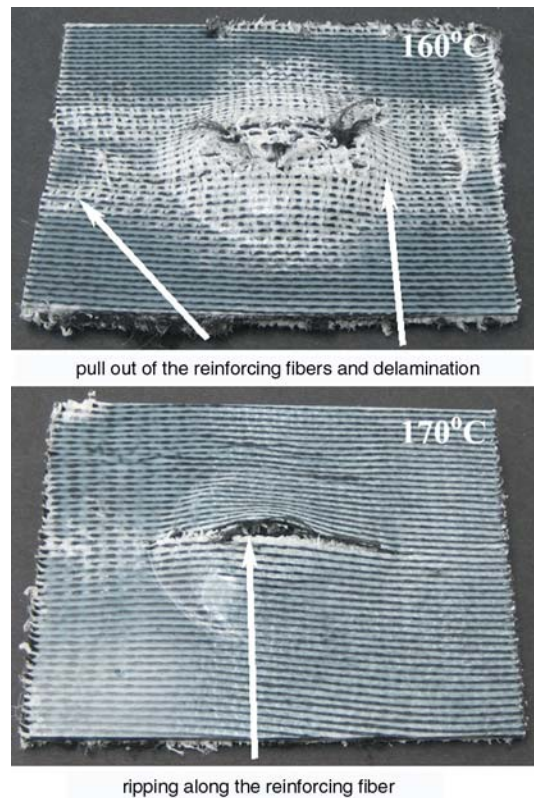


**Figure 11.** Typical failure behavior of knitted IFWI specimens of knitted fabric-based SRPPCs (produced at 160 and 170°C)

To compare the knitted fabric and carded mat-based SRPPCs, it can be stated that the tensile strength is much higher for knitted fabric-based SRPPCs (38 wt%) than the carded mat-based one (70 wt%), but there is no considerable difference in perforation energy values. The cause of the difference in tensile strength can be the fact that the knitted fabrics are composed of continuous fibers while carded mats contain chopped fibers.

#### 4. Conclusions

Self-reinforced polypropylene composites (SRPPC) were prepared by hot consolidation of knitted fabrics and carded mats with different reinforcement content. Both kinds of textile structures were consolidated by hot pressing at different temperatures (160, 165 and 170°C) at constant pressure (6 MPa) and for constant holding time (2 min). The consolidation quality of the resulting composite sheets was studied on polished and cut cross section with light and scanning electron microscopes, respectively. Static tensile and dynamic falling weight impact tests were performed on the composite plates. Based on the results the following conclusions can be drawn:

1. With the set processing parameters, the selected and applied matrix fiber / reinforcing fiber combinations are suitable for forming self-reinforced polymer composites with excellent mechanical properties (in reinforcing fiber direction).
2. According to the LM and SEM pictures it can be stated that the matrix fibers have melted at the highest temperature (170°C) and formed the matrix in which the reinforcing fibers or roving (for knitted fabrics) are embedded therefore better adhesion can be supposed.
3. In case of higher reinforcing contents, the processing (hot consolidation) temperature influences the tensile strength and perforation energy the most significantly for both textile structures.
4. The knitted fabric-based SRPPCs containing continuous reinforcing iPP fiber possess better mechanical properties than the carded mat-based version containing discontinuous reinforcing iPP fibers even if the reinforcement content of the latter is much higher.

#### Acknowledgements

This work was supported by the János Bolyai Research Scholarship of the Hungarian Academy of Sciences and the Hungarian Scientific Research Fund (OTKA F60505 and NI62729).

#### References

- [1] Ward I. M., Hine P. J.: The science and technology of hot compaction. *Polymer*, **45**, 1423–1437 (2004).
- [2] Peijs T.: Composites for recyclability. *Materials Today*, **6**, 30–35 (2003).
- [3] Houshyar S., Shanks R. A., Hodzic A.: Influence of different woven geometry in poly(propylene) woven composites. *Macromolecular Materials and Engineering*, **290**, 45–52 (2005).
- [4] Bárány T., Karger-Kocsis J., Czigány T.: Development and characterization of self-reinforced poly(propylene) composites: carded mat reinforcement. *Polymers for Advanced Technologies*, **9–10**, 818–824 (2006).
- [5] Hine P. J., Ward I. M., Jordan N. D., Olley R., Bassett D. C.: The hot compaction behaviour of woven oriented polypropylene fibres and tapes. I. Mechanical properties. *Polymer*, **44**, 1117–1131 (2003).
- [6] Ward I. M.: Developments in oriented polymers, 1970–2004. *Plastics, Rubber and Composites*, **33**, 189–194 (2004).
- [7] Alcock B., Cabrera N. O., Barkoula N-M., Loos J., Peijs T.: The mechanical properties of unidirectional all-polypropylene composites. *Composites, Part A: Applied Science and Manufacturing*, **37**, 716–726 (2006).
- [8] Alcock B., Cabrera N. O., Barkoula N-M., Loos J., Peijs T.: Interfacial properties of highly oriented coextruded polypropylene tapes for the creation of recyclable all-polypropylene composites. *Journal of Applied Polymer Science*, **104**, 118–129 (2007).
- [9] Abraham T., Banik K., Karger-Kocsis J.: All-PP composites (PURE®) with unidirectional and cross-ply lay-ups: dynamic mechanical thermal analysis. *Express Polymer Letters*, **1**, 519–526 (2007).
- [10] Houshyar S., Shanks R. A.: Tensile properties and creep response of polypropylene fibre composites with variation of fibre diameter. *Polymer International*, **53**, 1752–1759 (2004).
- [11] Bárány T., Izer A., Czigány T.: High performance self-reinforced polypropylene composites. *Materials Science Forum*, **537–538**, 121–128 (2007).
- [12] Bárány T., Izer A., Czigány T.: On consolidation of self-reinforced polypropylene composites. *Plastics, Rubber and Composites*, **35**, 375–379 (2006).

# Controlled release profiles of dipyridamole from biodegradable microspheres on the base of poly(3-hydroxybutyrate)

A. P. Bonartsev<sup>1,3\*</sup>, V. A. Livshits<sup>1</sup>, T. A. Makhina<sup>1</sup>, V. L. Myshkina<sup>1</sup>, G. A. Bonartseva<sup>1</sup>,  
A. L. Iordanskii<sup>1,2</sup>

<sup>1</sup>Laboratory of biochemistry of nitrogen fixation, A. N. Bach's Institute of Biochemistry, Russian Academy of Sciences, Leninskii prosp. 33, 119071 Moscow, Russia

<sup>2</sup>Laboratory of transport phenomena in polymers, N. N. Semenov's Institute of Chemical Physics, Russian Academy of Sciences, Kosygin str. 4, 119991 Moscow, Russia

<sup>3</sup>Laboratory of enzyme chemistry, Faculty of Biology, Moscow State University, Leninskie gory 1-12, 119992 Moscow, Russia

Received 19 July 2007; accepted in revised form 15 October 2007

**Abstract.** Novel biodegradable microspheres on the base of poly(3-hydroxybutyrate) (PHB) designed for controlled release of antithrombotic drug, namely dipyridamole (DPD), have been kinetically studied. The profiles of release from the microspheres with different diameters 4, 9, 63, and 92  $\mu\text{m}$  present the progression of nonlinear and linear stages. Diffusion-kinetic equation describing both linear (PHB hydrolysis) and nonlinear (diffusion) stages of the DPD release profiles from the spherical subjects has been written down as the sum of two terms: desorption from the homogeneous sphere in accordance with diffusion mechanism and the zero-order release. In contrast to the diffusivity dependence on microsphere size, the constant characteristics ( $k$ ) of linearity are scarcely affected by the diameter of PHB microparticles. The view of the kinetic profiles as well as the low rate of DPD release are in satisfactory agreement with kinetics of weight loss measured *in vitro* for the PHB films. Taking into account kinetic results, we suppose that the degradation of both films and PHB microspheres is responsible for the linear stage of DPD release profiles. In the nearest future, combination of biodegradable PHB and DPD as a representative of proliferation cell inhibitors will give possibility to elaborate the novel injectable therapeutic system for a local, long-term, antiproliferative action.

**Keywords:** biodegradable polymers, poly(3-hydroxybutyrate), microspheres, controlled drug release, diffusion

## 1. Introduction

For the last three decades the intensive research studies and developments of polymer systems for controlled release of pharmaceuticals have been carried out [1–3]. At curative dose the prolonged delivery of drugs from the systems into organism permits to eliminate the shortcomings in peroral, injectable, aerosol, and the other traditional methods of drug administration. Among those shortcomings hypertoxicity, instability, pulsative character

of rate delivery, ineffective expenditure of drugs should be pointed out. Alternatively, applications of therapeutical polymer systems provide orderly and purposefully the deliverance for an optimal dose of agent that is very important at therapy of acute or chronic diseases [4]. At treatment of cardiovascular and other diseases one of the perspective classes of drugs is the class of inhibitors of cell proliferation (ICP). In particular, pharmaceuticals on the base of ICP are widely used for preventing

\*Corresponding author, e-mail: [bonar@inbi.ras.ru](mailto:bonar@inbi.ras.ru)  
© BME-PT and GTE

the spread of restenosis after operations in cardiovascular surgery [5, 6]. In this relation, it has been recently shown that a wide-spread antithrombotic drug dipyridamole (DPD) inhibits effectively the cell proliferation, but the DPD advantages the minority of negative by-effects [7, 8] in contradistinction to most of ICP. In accordance with this argument DPD has been picked over as the effector for designing polymer therapeutic system for controlled drug delivery. Quite recently Zhu and coworkers [9] have designed the DPD controlled release polymer system on the base of microspheres composed of polylactide – polyglycolide copolymers (PLGA). They have clearly shown that DPD release includes two stages: the diffusion stage and the subsequent stage of hydrolytic degradation of PLGA. It is worth to note that the use of implants consisting of polylactides, polyglycolides and their copolymers is not without a number of sequelae related with the chronic inflammatory reactions in tissue [10–14].

Instead of PLGA applications, we propose alternatively to use bacterial poly(3-hydroxybutyrate) (PHB) [15]. Recently PHB and its copolymers are a focus of attention as biodegradable and biocompatible materials for biomedicine. The combination of physical and biological properties promote the use of this polymer for design and elaboration of different medical devices such as surgical sutures, repair patches, vascular prostheses, stents, periodontal membranes, orthopaedic implants, wound dressings etc. [16]. Besides, the ability of PHB to encapsulation and further release of drugs permits the use of PHB to design novel therapeutic systems [15].

Taking into account the above arguments, the objects of this paper are the production of PHB microspheres loaded with the DPD as well as the study of kinetic profile of the drug release in cardiovascular therapy. In the nearest future, combination of biodegradable PHB and DPD as a representative of proliferation cell inhibitors will give possibility to design an injectable therapeutic system for a local, long-term, antiproliferative action.

## 2. Materials and methods

### 2.1. PHB production

The PHB strain used in this work (*Azotobacter chroococcum* 7B) was capable of synthesizing PHB in an amount of up to 80% on the dry weight basis

of the cells. A collection of strains of the genus *Azotobacter* were maintained on Ashbey's medium. To achieve cellular PHB hyperproduction, the culture of the *Azotobacter* strain was grown on Burke's medium in excess of content of the carbon source [17]. The process of isolation and purification from the biomass of *A. chroococcum* 7B included the following stages: dissolution of PHB in chloroform by shaking at 37°C for 12 h, separation of the PHB solution from the cell residue by filtration, isolation of the PHB by isopropanol precipitation, and repeated its dissolution in chloroform followed by isopropanol precipitation and drying at 60°C. The MW of the polymer was determined by viscosimetry. Measurements of viscosity in the PHB – chloroform solutions were performed at 30°C. The MW was calculated using the Mark-Houwink-Kuhn equation  $[\eta] = 7.7 \cdot 10^{-5} \cdot M^{0.82}$  [18]. The chemical structure of PHB, the type of its crystal lattice, and its crystallinity (0.74) were previously determined using the methods of differential scanning calorimetry, IR Fourier spectroscopy, and crystal X-ray structure analysis [19].

### 2.2. Microsphere preparation and characterization

Dipyridamole-incorporated PHB microspheres were prepared using an oil-in-water emulsion method [9]. PHB polymer with molecular weight (MW) of 485 kDa was used for microspheres preparation. DPD and PHB in proportions of 1:4 were dissolved in 8 ml of chloroform. The solution was added drop-wise to 300 ml of PVA solution (0.4–1.2% w/v) while stirred. The mixture was homogenized for 2 h at 600–2000 rpm using an overhead stirrer RZR 2021 (Heidolph, Germany) or at 20 000 using a homogenizer SilentCruiser M (Heidolph, Germany). After complete chloroform evaporation the produced solid microspheres were divided by glass filter with various pore sizes. The final product was obtained by centrifugation (5702 R centrifuge, Eppendorf, Germany), washing with distilled water. The centrifugation and washing processes were repeated at least five times to completely remove PVA and DPD adsorbed onto the microspheres surface. Then the microspheres were dried in thermostat at 60°C and gently powdered. Encapsulation efficiency of microspheres was calculated from the ratio of the encapsulated

drug amount in microspheres to the total drug amount used for preparation.

For the microspheres with the highest diameter (group 4) we duplicated the concentration of DPD in order to enhance the rate of release. (The rate of release is decreased with the increase of sphere diameter). The concentration increase was required for the sake of adjustment of all kinetic profiles including the largest microspheres in the same time scale ( $x$ -axis). The amount of loaded DPD was determined by dissolving the microspheres in chloroform followed by spectrophotometric analysis with UV-spectrophotometer DU-650 (Beckman Coulter, USA) at maximums of DPD absorption (293 and 415 nm). The preparation of PHB films for loss of polymer mass presented in Figure 4 has been described in our preliminary paper [15].

### 2.3. In vitro release

Controlled release of DPD from PHB microspheres was carried out at conditions in vitro: in phosphate-buffered saline (pH 7.4) at 37°C. Eight lots of each group of about 5 mg of DPD-loaded PHB microspheres were used as drug depot. 4 ml of release medium (phosphate-buffered saline, pH 7.4) was added to each drug depot in the vial to maintain sink conditions. The mixture was agitated at 50 rpm at magnetic stirrer MS-01 (Elmi, Latvia) in a thermostat TC-1/20 (Russia) at 37°C. At specific time points, release medium was sampled completely by centrifugation of mixture at 14 000 rpm (5702 R centrifuge, Eppendorf, Germany) and assayed for DPD using the spectroscopic method. The release kinetics was then determined. The removed release medium was replaced with an equal volume of fresh medium after each sampling and was added to deposited microspheres. Residual content of DPD in microspheres was also measured by spectrophotometric technique. The conditions of experiment (stirring rate, volume and concentration of working solutions) for obtaining of DPD-loaded PHB

microspheres with different diameter are collected in Table 1. From this table we can see that the stirring rate is a dominating factor affecting the sphere diameter. The weight loss of polymer films was determined by drying and weighting of the samples after their exposition in the buffer as it was described in [15].

### 3. Results and discussion

As a drug vehicle of DPD, we have used the microspheres produced from PHB solution by the oil-in-water emulsion method described in Experimental part. The pioneer work devoted to PHB microsphere preparation have been presented in [18]. Figure 1 presents a typical microphotograph of spherical samples with diameter 63  $\mu\text{m}$  loaded by DPD. As can be seen in this figure, the PHB subjects have the spherical form without visible defects. They are adequately homogeneous and do not have visible inclusions or voids. Besides, the yellow DPD has slightly colored the interior of the microspheres; therefore, as well as Kassab *et al.* [20], we assume a uniform distribution of the drug throughout the volume of a microsphere.

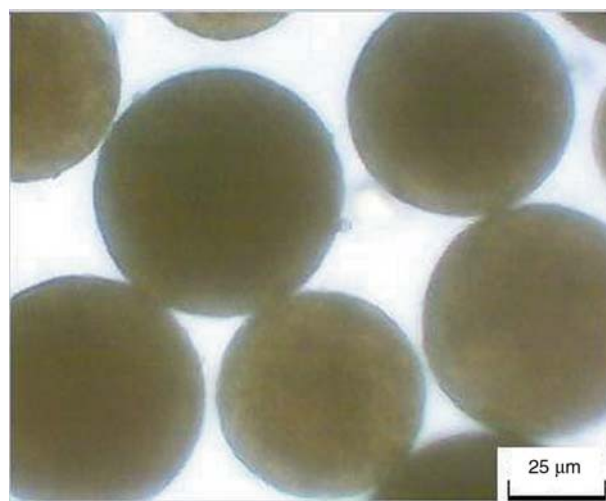


**Figure 1.** Microphotographs of PHB microspheres loaded by DPD with diameters 63  $\mu\text{m}$

**Table 1.** The conditions for producing PHB microspheres of different diameter loaded with definite content of DPD

Group #	Mass of DPD in working solution [mg]	Mass of PHB in working solution [mg]	PVA concentration [% (w/w)]	Stirring rate [rpm]	Diameter of microspheres mkm $\pm$ SD	DPD content in PHB microspheres [% (w/w)]*
1	24	96	0.8	2000	3.6 $\pm$ 2.4	4.8 $\pm$ 0.4
2	24	96	0.6	1000	18.7 $\pm$ 2.9	5.2 $\pm$ 0.4
3	24	96	0.4	600	62.7 $\pm$ 6.6	4.9 $\pm$ 0.4
4	47	100	0.6	500	91.7 $\pm$ 15.4	11.0 $\pm$ 0.5

\*Averaged values for ten samples with standard deviation

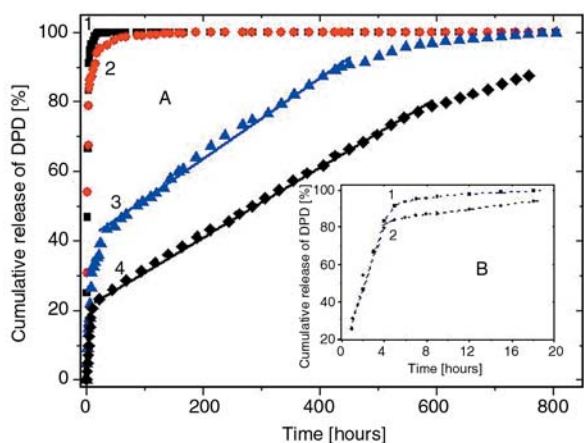


**Figure 2.** Kinetics profiles of DPD release from PHB microspheres *in vitro* (phosphate buffer, 37°C). A: General view of kinetic curves for the microspheres with different diameters: 4(1), 19(2), 63(3), and 92(4) μm. The lines show the second stage of release following the zero-order equation. B: Details of the curves for the microspheres with the smaller diameters: 4(1), 19(2)

The kinetic profiles of DPD release into phosphate buffer for the microspheres with different diameters are presented in Figure 2. The curves 3 and 4 referring to the series with the bigger diameters 63 and 92 μm, respectively, have two distinctive ranges: the initial range where fast release is observed and the following one where the constant rate is exhibited for a sufficiently long time of release (several hundreds of hours). For the microspheres with a relatively small diameter (19 μm, curve 2), we may also point out a small linear part of the drug release curve for 6–21 h interval, but for the smallest samples (diameter is as small as 4 μm, curve 1) the linear range is practically missing.

The similar profiles of drug release had been observed and have been well described for the microspheres on the base of PLGA and loaded by 5-fluorouracil [21]. The difference between the kinetic profiles between PHB and PLGA microspheres is that the copolymer microspheres have the third kinetic range when at the final stage the abrupt emission of 5-fluorouracil comes about. Most recently, in our works describing release profiles of DPD [15], indomethacin [15], and 5-nitrofurfuralidene semicarbozone [22] from the films of PHB, we have shown that for all three drugs the kinetic curves of release have the initial diffusion stage which smoothly transforms to the linear stage. However, the third abrupt stage was absent for all systems for several weeks. Taking into account

generally the Sipman’s three-stage model of release [21, 23, 24], we note that for the PHB microspheres having a higher hydrolysis resistance as compared with PLGA, final stage of PHB network degradation and, hence, at the given conditions *in vitro* a drastic DPD discharge has not attained (see Figure 2). At the same time, reposing on the literature data and our experiments obtained for the ‘PHB films – drug’ systems [15, 22] we assume that the linear part of the kinetic curves for both the films and the microspheres could be interpreted rather as the start of zero-order hydrolytic reaction for PHB macromolecules.

Diffusion-kinetic equation describing both linear (hydrolysis) and nonlinear (diffusion) stages of the DPD release profiles from the spherical subjects could be written down as the sum of two terms : desorption from the homogeneous sphere in accordance with diffusion mechanism (the first summand involving square brackets in Equation (1a)) and the zero-power release (the addend in this equation):

$$\frac{\partial G_t}{\partial t} = D \left[ \frac{\partial^2 G_t}{\partial z^2} + \left( \frac{2}{z} \right) \left( \frac{\partial G_t}{\partial z} \right) \right] + k \tag{1a}$$

Here  $D$  is the constant (or averaged) diffusion coefficient of the drug in the polymer microspheres, [cm<sup>2</sup>/sec];  $G_t(z, t)$ ,  $\partial G_t/\partial z$ ,  $\partial G_t/\partial t$  and  $\partial^2 G_t/\partial z^2$  are the current drug concentration [%], the first and second derivatives of  $G_t$  with respect to  $t$  (time) or  $z$  (spherical coordinate of diffusion) respectively; and  $k$  is the zero-order constant. Following Crank [25], transformation of Equation (1a) into the conventional diffusion equation (1b) for spheres has been performed by introduction of new variables  $C_t \equiv G_t - kt$  and  $u = C_t z$ :

$$\frac{\partial u}{\partial t} = D \left[ \frac{\partial^2 u}{\partial z^2} \right] \tag{1b}$$

The boundary and initial conditions for solution of differential Equation (1a) have been written by standard way. At  $t = 0$ ,  $C_0 = \text{const}$  in the interval  $0 < z < R$ , and at  $t > 0$  and  $z = R$  we have  $C_0 = 0$ , at  $t > 0$  and  $z = 0$ ,  $u = C_t z = 0$ .

In accordance with our approach, at any time of release the balance of the drug masses in the surrounding medium is fulfilled as Equation (2):

$$G_{mt} = M_t + M_{Ht} \tag{2}$$

here  $G_{mt}$  is the total amount of DPD [mg] released from the microspheres by the time  $t$ ;  $M_t$  is the portion of DPD mass released via the diffusion process; and  $M_{Ht}$  is the other portion of DPD mass released via degradation mechanism.

It is common knowledge that solution of Equation (1b) has two variations, namely for relatively small time of diffusion when  $M_t/M_\infty \leq 0.5$  approximately and for relatively long time when the condition  $M_t/M_\infty > 0.5$  is fulfilled. In the first instance the approximation (3) is correct [25]:

$$\frac{M_t}{M_\infty} = 6 \left[ \left( \frac{D_\alpha t}{\pi^2 R^2} \right)^{0.5} \right] \tag{3}$$

where  $M_t$ ,  $M_\infty$  are cumulative weights of the drug desorbed via diffusion by the time  $t$  and infinite time ( $t \rightarrow \infty$ ); respectively;  $R$  is averaged radius of microsphere; the other symbols are the same as in Equation (1a). In the second instance the expression (4) should be used:

$$\frac{M_t}{M_\infty} = 1 - \left( \frac{6}{\pi^2} \right) \exp \left[ - \frac{D_\beta \pi^2 t}{R^2} \right] \tag{4}$$

The graphic constructions of the diffusion data in the framework of Equation (3) ( $M_t/M_\infty - t^{0.5}$ ) or logarithmic variant of Equation (4) ( $\ln(M_t/M_\infty) - t$ ) enable us to use these equations as a criterion of transport mechanism and simultaneously calculate the DPD diffusivities in PHB. In Figure 3a the fragments of kinetic profiles for release from PHB microspheres with different diameters are shown. The release data being plotted in coordinates of

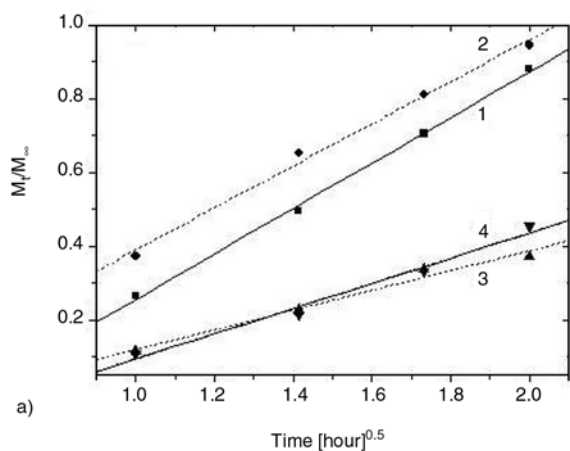


**Table 2.** DPD diffusion coefficients in the PHB microspheres for relatively small (Equation (3)) and long (Equation (4)) time of diffusion

Diameter of specimen ·10 <sup>3</sup> [cm]	Diffusion coefficient ·10 <sup>11</sup> [cm <sup>2</sup> /s] (Equation (4))	Diffusion coefficient ·10 <sup>11</sup> [cm <sup>2</sup> /s] (Equation (3))
0,36	0,10	0,08
1,9	1,5	2,0
6,3	2,8	2,6
9,2	21,1	16

Equation (3) – the relative loss of DPD in microspheres ( $M_t/M_\infty$ ) versus square root of time – give the values of diffusion coefficients,  $D_\alpha = \pi^2 R^2 \cdot (\text{tg}\alpha)^2 / 36$ , where  $\text{tg}\alpha$  is the slope ratio of linear part of the release curves. The examples of the graphical solution for Equation (4) in semilog coordinates for the microspheres with different diameters are presented in Figure 3b. The integral diffusion coefficients of DPD ( $D_\beta$ ) could be easily estimated through expression  $D_\beta = \text{tg}\alpha \cdot R^2 / \pi^2$ , where  $\text{tg}\beta$  is also the slope ratio of linear part for the release curves presented, however, in the semilog linear coordinates (Figure 3b). Both diffusivities ( $D_\alpha$ ,  $D_\beta$ ) are shown in Table 2. In case of molecular diffusion one would expect a coincidence between values of diffusion coefficients calculated by different Equations (3) and (4). Table 2 demonstrates actually the closely adjacent values of DPD diffusivities that support the real diffusion mechanism of release going on the initial stage of the kinetics curves. Just as in the paper [21], for the systems PLGA loaded by 5-fluorocycle, in the PHB-DPD samples concerned the diffusion coefficients depend sharply on the size of the microspheres.

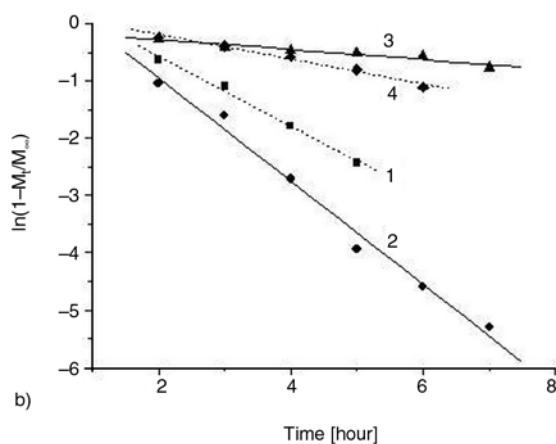


**Figure 3.** Initial (a) and final (b) regions of diffusion stage for DPD release from the PHB microspheres with diameters 4 μm (1), 19 μm (2), 63 μm (3), and 92 μm (4). The data are represented in coordinates of Equation (3) and in semilogarithmic coordinates of Equation (4)

As previously stated above, the linear kinetics of DPD release occurs together with diffusion mechanism (see Figure 2). For the series of microparticles with diameters 92, 63, and 19  $\mu\text{m}$  the kinetic impact comes into particular prominence after terminating diffusion. In contrast to the diffusivity dependence on microsphere size, the constant characteristics ( $k$ ) of linearity are scarcely affected by diameter of PHB microparticles. The proper rate of hydrolytic degradation should not dependent on geometry of a sample as evidenced by Figure 2 (linear ranges for microspheres with diameters are 92 and 63  $\mu\text{m}$ ). The analogous conclusion has been published in the basic paper of Witt and Kissel [26] for PLGA microspheres.

The view of the kinetic profiles as well as the low rate of DPD release are in satisfactory agreement with kinetics of weight loss measured *in vitro* for the PHB films. The thickness of the PHB films (40  $\mu\text{m}$ ) was close to the diameters of our microspheres. In this case we assume that the proper hydrolysis kinetics may be similar for both the microspheres and the films.

As is obvious from Figure 4, the change in weight of the films as function of time occurs in accordance with a zero-order equation as well. The exception is an abrupt initial step of weight loss which may be interpreted as a fast extraction of residual impurities. Nature of these impurities is still unknown. It is not impossible that the impurities include the traces of monomers and oligomers

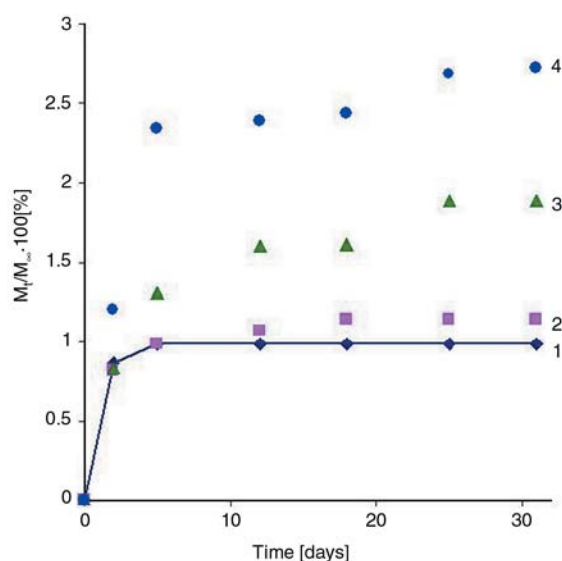


**Figure 4.** Loss of PHB weight as function of time for the films loaded by DPD. Concentration of DPD: 1 (0%), 2 (3%), 3 (10%), and 4 (30%)

coming during PHB isolation and film preparation. Whatever the nature of impurities may be, the following slow loss in PHB weight is observed in the same time frame that the linear kinetics of release (compare Figures 2 and 4). Here we note again that the slope of the kinetic curves reflected the weight loss approximately identical. Taking into account the above results, we may suppose that the domination of degradation for both PHB films and microspheres is responsible for the second linear stage of DPD release profiles. Assessment of the changes in the weight of the PHB microspheres immediately and the nature of this phenomenon are an urgent experimental challenge.

#### 4. Conclusions

We produced the biodegradable PHB-based microspheres by the oil-in-water emulsion technique. The microspheres with different diameters in interval 4–92  $\mu\text{m}$  were loaded with DPD which presents the class of inhibitors of cell proliferation and simultaneously the antithrombotic drugs. The kinetic profiles of drug release from microspheres into phosphate buffer conformed to the superposition of diffusion and zero-order process of PHB degradation. A sufficiently protensive linear part of kinetic profiles provides a way for application the PHB-DPD microsystem as a local drug release medical preparation.

#### Acknowledgements

This work was supported by grant no. 06-04-49339 from the Russian Foundation for Basic Research (RFBR) and by grant no. 07-II-10 from Foundation for Assistance to Small Innovative Enterprises (FASIE).

#### References

- [1] Lonsdale H. K.: The growth of membrane technology. *Journal of Membrane Science*, **10**, 81–181 (1982).
- [2] Douglas S. J., Davis S. S., Illum L.: Nanoparticles in drug delivery. *CRC Critical Reviews in Therapeutic Drug Carrier Systems*, **3**, 233–261 (1987).
- [3] Langer R. S., Wise D. L.: Medical applications of controlled release, Vol 2, Applications and evaluations. CRC Press, Boca Raton (1984).
- [4] Stauch M., Grossmann G., Wanjura D., Adam W-E.: Lack of tolerance after chronic administration of controlled-release isosorbide-5-mononitrate. *European Journal of Clinical Pharmacology*, **38**, Supplement 1, 31–34 (1990).

- [5] Ellis J. T., Kilpatrick D. L., Consigny P. M., Prabhu S., Hossainy S. F. A.: Therapy considerations in drug eluting stents. *Critical Reviews in Therapeutic Drug Carrier Systems*, **22**, 114–139 (2005).
- [6] Sarkar K., Sharma S. K., Sachdeva R., Romeo F., Garza L., Mehta J. L.: Coronary artery restenosis: Vascular biology and emerging therapeutic strategies. *Expert Review of Cardiovascular Therapy*, **4**, 543–556 (2006).
- [7] Masaki T., Kamerath C. D., Kim S.-J., Leypoldt J. K., Mohammad S. F., Cheung A. K.: In vitro pharmacological inhibition of human vascular smooth muscle cell proliferation for the prevention of hemodialysis vascular access stenosis. *Blood Purification*, **22**, 307–312 (2004).
- [8] Singh L. P., Rothfuss K. J., Wiernicki T. R., Lacefield W. B., Kurtz W. L., Brown R. F., Brune K. A., Bailey D., Dube G. P.: Dipyridamole directly inhibits vascular smooth muscle cell proliferation in vitro and in vivo: Implication in the treatment of restenosis after angioplasty. *Journal of the American College of Cardiology*, **23**, 665–671 (1994).
- [9] Zhu W., Masaki T., Bae Y. H., Rathi R., Cheung A. K., Kern S. E.: Development of a sustained-release system for perivascular delivery of dipyridamole. *Journal of Biomedical Materials Research, Part B: Applied Biomaterials*, **77**, 135–143 (2006).
- [10] Solheim E., Sudmann B., Bang G., Sudmann E.: Biocompatibility and effect on osteogenesis of poly(ortho ester) compared to poly(DL-lactic acid). *Journal of Biomedical Materials Research*, **49**, 257–263 (2000).
- [11] Böstman O., Pihlajamäki H.: Clinical biocompatibility of biodegradable orthopaedic implants for internal fixation: a review. *Biomaterials*, **21**, 2615–2621 (2000).
- [12] Lickorish D., Chan J., Song J., Davies J. E.: An in vivo model to interrogate the transition from acute to chronic inflammation. *European Cells and Materials*, **8**, 12–20 (2004).
- [13] Khouw I. M., van Wachem P. B., de Leij L. F., van Luyn M. J.: Inhibition of the tissue reaction to a biodegradable biomaterial by monoclonal antibodies to IFN-gamma. *Journal of Biomedical Materials Research*, **41**, 202–210 (1998).
- [14] Su S.-H., Nguyen K. T., Satasiya P., Greilich P. E., Tang L., Eberhart R. C.: Curcumin impregnation improves the mechanical properties and reduces the inflammatory response associated with poly(L-lactic acid) fiber. *Journal of Biomaterials Science, Polymer Edition*, **16**, 353–370 (2005).
- [15] Bonartsev A. P., Bonartseva G. A., Makhina T. K., Myshkina V. L., Luchinina E. S., Livshits V. A., Boskhomdzhev A. P., Markin V. S., Iordanskii A. L.: New poly-(3-hydroxybutyrate)-based systems for controlled release of dipyridamole and indomethacin. *Applied Biochemistry and Biotechnology*, **42**, 625–630 (2006).
- [16] Chen G. Q., Wu Q.: The application of polyhydroxyalkanoates as tissue engineering materials. *Biomaterials*, **26**, 6565–6578 (2005).
- [17] Bonartseva G. A., Myshkina V. L., Nikolaeva D. A., Kevbrina M. V., Kallistova A., Gerasin V. A., Iordanskii A. L., Nozhevnikova A. N.: Aerobic and anaerobic microbial degradation of poly- $\beta$ -hydroxybutyrate produced by *azotobacter chroococcum*. *Applied Biochemistry and Biotechnology*, **109**, 285–302 (2003).
- [18] Akita S., Einaga Y., Miyaki Y., Fujita H.: Properties of poly( $\beta$ -hydroxybutyrate) as a solution. *Macromolecules*, **9**, 774–780 (1976).
- [19] Rebrov A. V., Dubinskii V. A., Nekrasov Y. P., Bonartseva G. A., Shtamm M., Antipov E. M.: Structure phenomena at elastic deformation of highly oriented polyhydroxybutyrate. *Polymer Science (Russian)*, **44**, 347–351 (2002).
- [20] Kassab A. C., Xu K., Denkbass E. B., Dou Y., Zhao S., Piskin E.: Rifampicin carrying PHB microspheres as a potential chemoembolization agent. *Journal of Biomaterial Science, Polymer Edition*, **8**, 947–961 (1997).
- [21] Siepmann J., Siepmann F.: Microparticles used as drug delivery systems. *Progress in Colloid and Polymer Science*, **133**, 15–21 (2006).
- [22] Kosenko R. Y., Pankova Y. N., Iordanskii A. L., Zaikov G. E.: Controlled release of the antiseptic from poly(3-hydroxybutyrate) films. Combination of diffusion and zero order kinetics. *Journal of the Balkan Tribological Association*, **13**, 242–248 (2007).
- [23] Siepmann J., Faisant N., Benoit J.-P.: A new mathematical model quantifying drug release from bioerodible microparticles using Monte Carlo simulations. *Pharmaceutical Research*, **19**, 1885–1893 (2002).
- [24] Siepmann J., Elkharraz K., Siepmann F., Klose D.: How autocatalysis accelerates drug release from PLGA-based microparticles: A quantitative treatment. *Biomacromolecules*, **6**, 2312–2319 (2005).
- [25] Crank J.: *The mathematics of diffusion*. Clarendon Press, Oxford (1975).
- [26] Witt C., Kissel T.: Morphological characterization of microspheres, films and implants prepared from PLGA and ABA triblock copolymers: Is the erosion controlled by degradation, swelling or diffusion? *European Journal of Pharmaceutics and Biopharmaceutics*, **51**, 171–181 (2001).

# Examination of injection moulded thermoplastic maize starch

T. Tábi, J. G. Kovács\*

Department of Polymer Engineering, Budapest University of Technology and Economics, H-1111 Budapest, Hungary

Received 18 July 2007; accepted in revised form 23 October 2007

**Abstract.** This paper focuses on the effect of the different injection moulding parameters and storing methods on injection moulded thermoplastic maize starch (TPS). The glycerol and water plasticized starch was processed in a twin screw extruder and then with an injection moulding machine to produce TPS dumbbell specimens. Different injection moulding set-ups and storing conditions were used to analyse the effects on the properties of thermoplastic starch. Investigated parameters were injection moulding pressure, holding pressure, and for the storage: storage at 50% relative humidity, and under ambient conditions. After processing the mechanical and shrinkage properties of the manufactured TPS were determined as a function of the ageing time. While conditioning, the characteristics of the TPS changed from a soft material to a rigid material. Although this main behaviour remained, the different injection moulding parameters changed the characteristics of TPS. Scanning electron microscope observations revealed the changes in the material on ageing.

**Keywords:** *biodegradable polymers, thermoplastic starch, injection moulding*

## 1. Introduction

In recent years, the research and development on biodegradable polymers has accelerated. This progress is due to the interest of using renewable, natural resources for certain applications in the field of polymer processing [1]. The need for using more renewable resources has grown, because of the shrinking oil reserves, and the environmental friendly consciousness. Biodegradable polymers or biopolymers are capable of biodegradation in certain environments e.g. during composting. These materials represent the highest level of recycling. Biopolymers can be divided into two main groups [2]. One group contains the biodegradable polyesters, which are petroleum based, but they are biodegradable. The other group contains polymers from renewable resources, like thermoplastic starch or poly-lactic-acid (PLA). Both TPS and PLA can

be produced from common, natural resource, and they are readily biodegradable.

Starch can be found in different plants like wheat, maize, potato, rice. This material is in abundance all over the world. Starch has a granular structure, which is built by two main carbohydrate polymers: the linear amylose and the highly branched amylopectin. According to the botanical source the amylose-amylopectin ratio can be different. The granular structure must be totally destructured in order to produce thermoplastic starch. Starch can be processed into thermoplastic starch under the action of both temperature and shearing action [3–5]. Plasticizers like glycerol or water have to be used while processing, because of the low decomposition temperature of the granular starch. Processing usually takes place in an extruder, where the starch granules are disintegrated. After that thermoplastic starch pellets are produced, TPS can

\*Corresponding author, e-mail: [kovacs@pt.bme.hu](mailto:kovacs@pt.bme.hu)  
© BME-PT and GTE

be processed into a biodegradable product by injection moulding or compression moulding.

Although starch is a low-cost material, it has some drawbacks, while using it as a material for biodegradable products. One drawback is the so-called retrogradation or ageing. Many authors reported this behaviour of starch. While ageing, the crystallinity of starch increases, which results in higher stress at elongation and tensile modulus [6–9]. Starch has unfortunately a hydrophilic character, which also retards its widespread industrial applications. While in contact with water, pure starch products swell and then dissolve. Another factor is the low mechanical properties of starch and the high shrinkage values when injection moulded. Although starch possesses these drawbacks, it is a potential material of biodegradable products in the near future. To overcome these drawbacks, a great number of experiments were taken. Many authors reported the behaviour of starch reinforced with natural fibres, like flax, cellulose, jute, ramie, etc. [10–15]. With the reinforcement, the mechanical properties of starch improved, while the ageing, the hydrophilic character, and the shrinkage values decreased. Many authors also reported the behaviour of a starch-based blend. In this case starch was associated with another biopolymer, often with biodegradable polyesters, like polycaprolactone (PCL), polyesteramide (PEA), or with the starch based polylactic acid (PLA) [16–21]. The blending of starch with biodegradable polyesters also decreased the hydrophilic behaviour and the shrinkage values, but it had no effect on the ageing of starch. The mechanical properties of blends vary with the starch-biodegradable polyester content, but unfortunately only some of them are compatible with starch. In recent years, the researches concentrated on the cross linking of starch, and the association of starch with nano-particles [22–27]. With the help of cross-linking or nano-particles, the ageing, and strong hydrophilic character of thermoplastic starch can be reduced.

Starch plays the role of the matrix material in all these biocomposites, constituting the majority component of these blends. When injection moulded, the different injection moulding parameters could affect the long-term behaviour of TPS. This paper focuses on the effect of different injection moulding set-ups on the time dependent behaviour of TPS.

## 2. Experimental

Maize starch was used for the experiments. According to the manufacturer, the amylose-amylopectin ratio is 25:75. Maize starch was plasticized with glycerol (99% purity) and distilled water. The starch:glycerol:water ratio was 70:16:14 and glycerol-mono-stearate was added as a lubricant. A special silicone based screw cleaner material was used to clean the screw of the extruder and injection moulding machine from any contamination (provided by Szilor Ltd., Hungary). The TPS was produced in a two step process. First, the materials were weighted and mixed, then the mixture was processed with a Brabender Plasti-Corder PL 2100 double screw extruder (diameter 25 mm screw,  $L/D = 20$ ) with zone temperatures of 90-130-120-90°C (from hopper to die). The extrudate was granulated, and stored under controlled conditions (50% relative humidity for 4 weeks) before injection moulded. After the storing process, the granules were injection moulded with an Arburg 320 600-250 C injection moulding machine equipped with a diameter 35 mm screw. Table 1 contains the main parameters of the injection moulding process.

Dumbbell test specimens were injection moulded for the tensile and shrinkage measurements. The injection moulding pressure was 1400 bars, and the holding pressure was varied from 600 to 1000 bars to determine the effect of the holding pressure on the time dependence of TPS (Table 2). The injection moulded specimens were stored different ways (at 50% relative humidity and under ambient conditions) and for different time periods to determine the effect of ageing time and different storage type (Table 2).

**Table 1.** The main injection moulding parameters used

Injection moulding parameters		
Injection volume	44	[cm <sup>3</sup> ]
Injection pressure	1400	[bar]
Switch over point	12	[cm <sup>3</sup> ]
Injection rate	50	[cm <sup>3</sup> /s]
Holding pressure	VARIED (600–1000)	[bar]
Holding pressure	20	[s]
Cooling time	15	[s]
Zone temperatures		
1. Zone	110	[°C]
2. Zone	115	[°C]
3. Zone	120	[°C]
4. Zone	125	[°C]
5. Zone	130	[°C]
Mould temperature	25	[°C]

**Table 2.** The investigated parameters

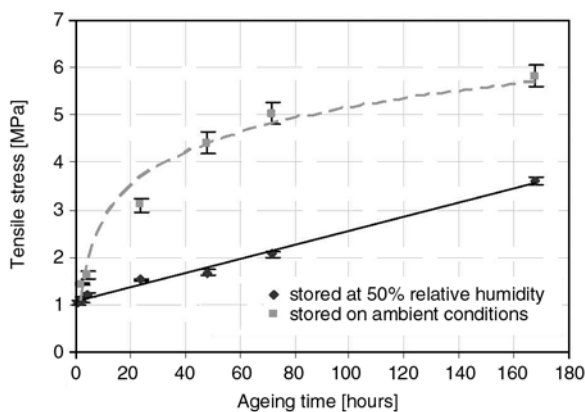
	800 bars of holding pressure	Varied holding pressure
50% relative humidity		×
Varied conditions	×	

Tensile tests (according to standard EN ISO 5275:1999) and shrinkage measurement (according to standard EN ISO 2944:2003) were taken at 1-2-4-24-48-72-168 hours after the injection moulding. A crosshead speed of 50 mm/min was used to determine the tensile properties. Finally, scanning electron microscope (SEM) observations were taken to determine the changes in the TPS material as a function of ageing time.

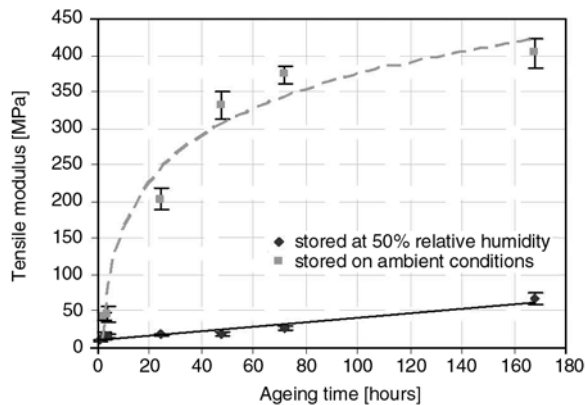
### 3. Results and discussion

Figure 1 and 2 show the evolution of the tensile stress and tensile modulus as the function of the ageing time (holding pressure was 800 bars). Two different storing methods can be distinguished: storing at 50% relative humidity and storing under ambient conditions. Ambient conditions mean that the specimens were stored indoors, in free air (at 40%±10% relative humidity, UV degradation or contact with rain excluded). As it can be observed the type of storage has great effect on the properties of TPS. Storing under ambient conditions accelerates the ageing of TPS, while storing under controlled conditions retarded the ageing. Although the tensile properties increased in time, the strain decreased (Figure 3).

The strain decrease of the specimens stored under ambient conditions is much more intense than the



**Figure 1.** The effect of the different storing conditions on the tensile stress



**Figure 2.** The effect of the different storing conditions on the tensile modulus

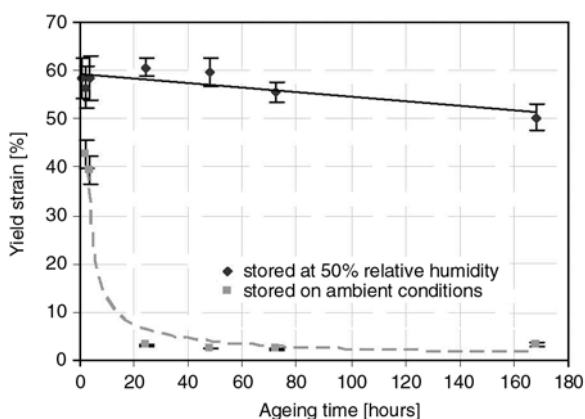


**Figure 3.** The effect of the different storing conditions on the yield strain

strain decrease of the specimens stored at 50% relative humidity.

In time the properties of the material changed from soft to rigid behaviour, as it can be observed on Figure 4.

The holding pressure was varied from 600 to 1000 bars to determine whether this parameter has

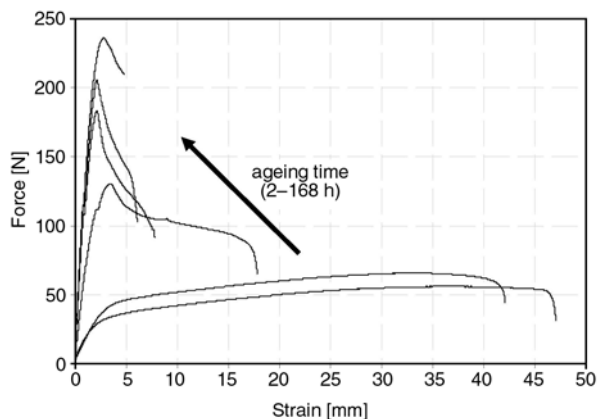


**Figure 4.** The change of tensile diagrams as a function of ageing time (2-4-24-48-72-168 hours, at ambient conditions)

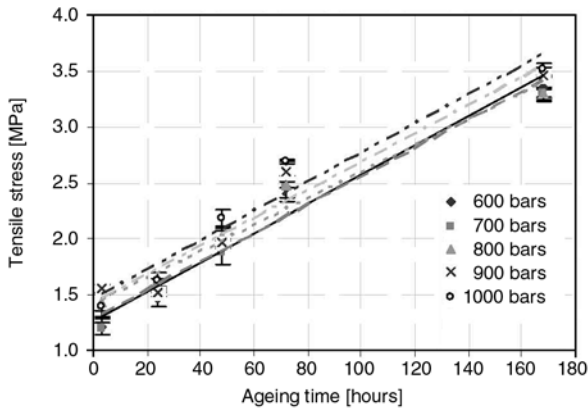


Figure 5. The effect of ageing time on the tensile stress

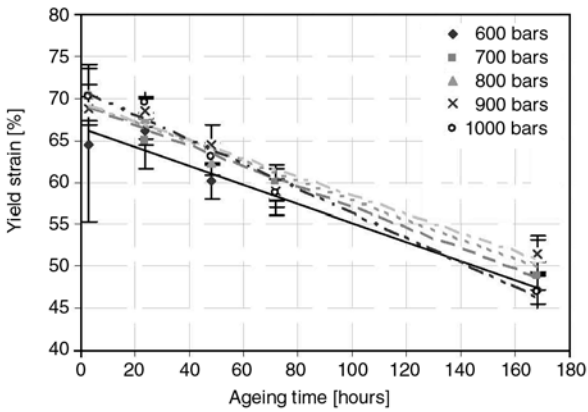


Figure 6. The effect of ageing time on the yield strain

any effect on the time dependent behaviour of TPS or not. The holding pressure had almost no effect on the tensile stress and tensile strain, as it can be seen in Figure 5 and 6.

While the tensile stress increased, the yield strain decreased independently from the holding pressure. The holding pressure had major effect on the tensile modulus (Figure 7) in time.

Although the tensile modulus of the TPS was the same just after injection moulding on all the hold-

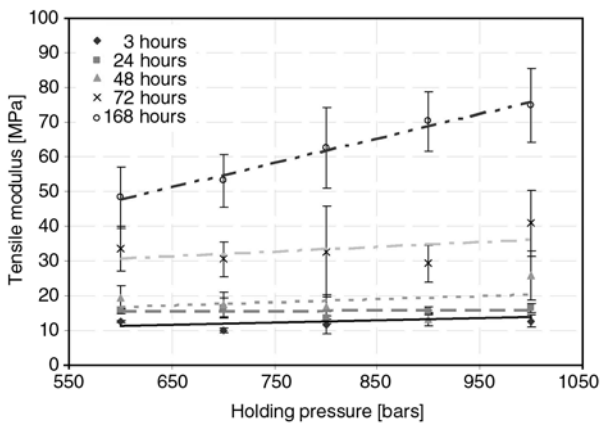


Figure 7. The effect of ageing time on the tensile modulus

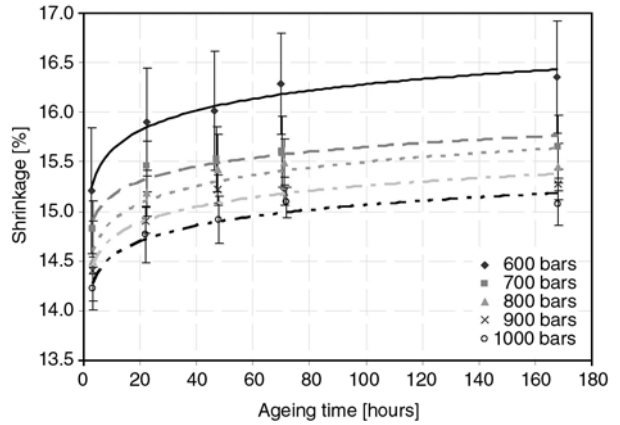


Figure 8. Linear shrinkage as a function of the ageing time

ing pressures, the holding pressure had effect on the time dependent behaviour of TPS. The calculated correlation coefficients demonstrate that even 72 hours after the ejection, the holding pressure history of the specimens had almost no effect on the tensile modulus. 168 hours after the demoulding, the holding pressure history of the specimens was not ignorable, the more the holding pressure applied, the more the measured tensile modulus values raised (even though the scatter was relatively high). This phenomenon is to be further researched in following papers. The effect of the holding pressure on the shrinkage properties can be monitored on Figure 8. Although the shrinkage of TPS is high, it can be lowered by applying higher holding pressure values.

The SEM images revealed that after the first extrusion the TPS pellets still contain some granular starch (Figure 9), which is almost totally disappeared after the injection moulding (Figure 10) or

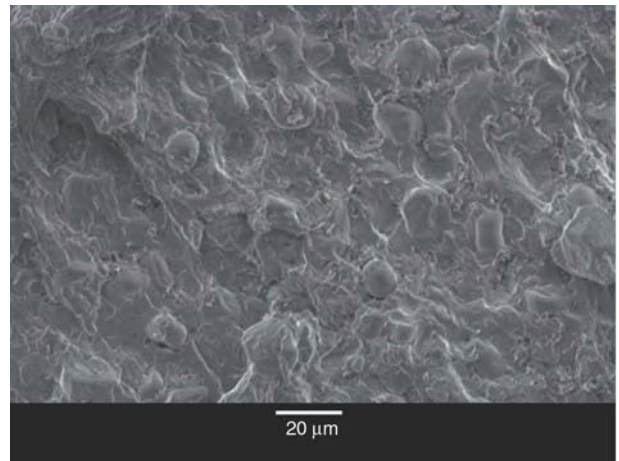
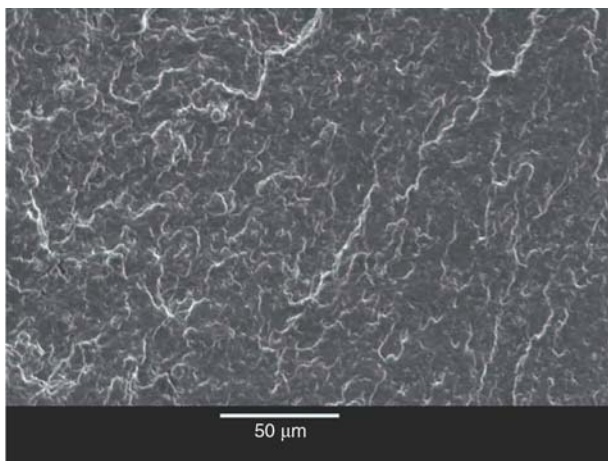
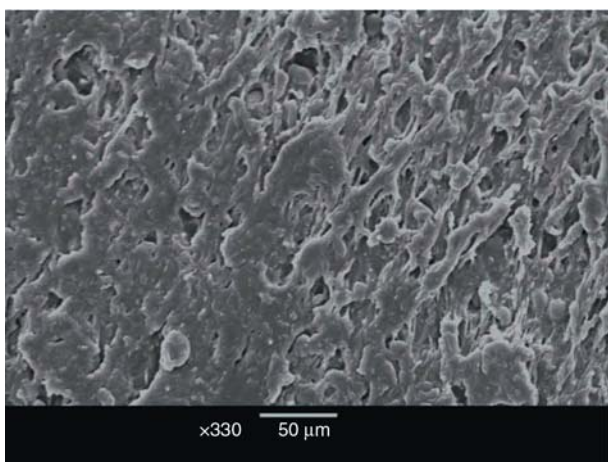


Figure 9. TPS surface after the first extrusion. Native starch pellets still can be found



**Figure 10.** TPS surface after injection moulding. Native starch granules totally destructur



**Figure 11.** TPS surface after a second extrusion process. Native starch granules totally destructured

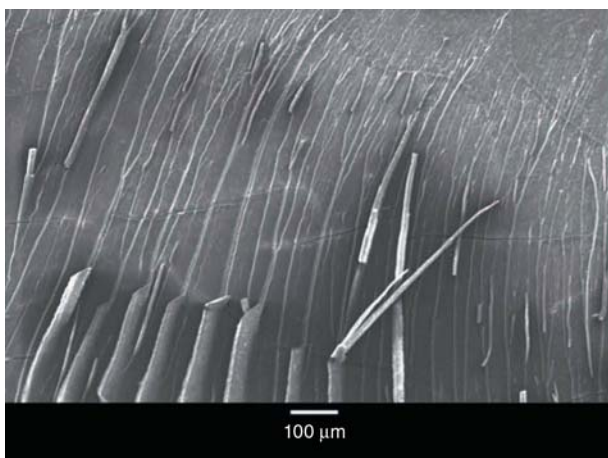


**Figure 12.** Aged TPS fracture surface. Significant quantity of cracks can be found

the second extrusion process (Figure 11). Although wide angle X-ray scattering measurements were taken (was not published in this paper) which indicated that the starch crystallinity disappeared (gran-

ular structure disintegrated), it is inconsistent with the SEM observations.

The SEM images verified that while ageing the material properties changed from rubber like behaviour to rigid. This phenomenon can be observed on the surface of the broken tensile test specimens. The fracture surface of the specimens became smoother and significant quantity of cracks can be detected as a function of ageing (Figure 12).

#### 4. Conclusions

Thermoplastic starch (maize starch:glycerol:water ratio is 70:16:14) was produced by extrusion and injection moulding. The effect of various injection moulding parameters and storing methods (on ambient conditions; at 50% relative humidity) were studied. It was found that ageing occurs much faster when TPS is stored on ambient conditions rather than at 50% relative humidity. The holding pressure had no effect on the tensile stress and on the yield strain of the specimens, but it had on the tensile modulus. The holding pressure history of the specimens had no effect on the tensile modulus for 72 hours. After this time period the holding pressure history of the specimens was not ignorable: the more the holding pressure applied, the more the tensile modulus raised. This phenomenon will be studied further in the future. The further investigation of holding pressure showed that it lowers the relatively high shrinkage values of TPS. The tensile diagrams of TPS showed that the properties of TPS changed from rubber like to a rigid behaviour. SEM images verified this phenomenon. The surface of the broken bars changed, and a rigid fracture surface was observed after 8 weeks of ageing.

#### Acknowledgements

The authors would like to thank Arburg Ltd. for the injection moulding machine, Wittmann Ltd. for mould temperature control unit, Anton Ltd. (Hungary) for the moulds and Szilor Ltd. (Hungary) for the screw cleaner material.

#### References

- [1] Zhang M. Q.: Polymeric materials from natural resources-emerging as the times require. *Express Polymer Letters*, **1**, 406 (2007).

- [2] Avérous L.: Biodegradable multiphase systems based on plasticized starch: A review. *Journal of Macromolecular Science, Part C: Polymer Reviews*, **44**, 231–274 (2004).
- [3] Stepto R. F. T.: Thermoplastic starch. *Macromolecular Symposia*, **152**, 73–82 (2000).
- [4] Stepto R. F. T.: The processing of starch as a thermoplastic. *Macromolecular Symposia*, **201**, 203–212 (2003).
- [5] Czigány T., Romhány G., Kovács J. G.: Starch for injection moulding purposes. in 'Engineering Biopolymers: Homopolymers, Blends, and Composites' (eds.: Fakirov S., Bhattacharyya D.) Hanser, Munich, 81–108 (2007).
- [6] Van Soest J. J. G., Hullemann S. H. D., De Wit D., Vliegthart J. F. G.: Crystallinity in starch bioplastics. *Industrial Crops and Products*, **5**, 11–22 (1996).
- [7] Van Soest J. J. G., Vliegthart J. F. G.: Crystallinity in starch plastics: Consequences for material properties. *Trends in Biotechnology*, **15**, 208–213 (1997).
- [8] Van Soest J. J. G., Hullemann S. H. D., De Wit D., Vliegthart J. F. G.: Changes in the mechanical properties of thermoplastic potato starch in relation with changes in B-type crystallinity. *Carbohydrate Polymers*, **29**, 225–232 (1996).
- [9] Kuutti L., Peltonen J., Myllärinen P., Telemann O., Forsell P.: AFM in studies of thermoplastic starches during ageing. *Carbohydrate Polymers*, **37**, 7–12 (1998).
- [10] Wollerdorfer M., Bader H.: Influence of natural fibres on the mechanical properties of biodegradable polymers. *Industrial Crops and Products*, **8**, 105–112 (1998).
- [11] Avérous L., Boquillon N.: Biocomposites based on plasticized starch: thermal and mechanical behaviours. *Carbohydrate Polymers*, **56**, 111–122 (2004).
- [12] Avérous L., Fringant C., Moro L.: Plasticized starch-cellulose interactions in polysaccharide composites. *Polymer*, **42**, 6565–6572 (2001).
- [13] Gáspár M., Benkő Zs., Dogossy G., Réczey K., Czigány T.: Reducing water absorption in compostable starch-based plastics. *Polymer Degradation and Stability*, **90**, 563–569 (2005).
- [14] Ma X., Yu J., Kennedy J. F.: Studies on the properties of natural fiber-reinforced thermoplastic starch composites. *Carbohydrate Polymers*, **62**, 19–24 (2005).
- [15] Bodros E., Pillin I., Montrelay N., Baley C.: Could biopolymers reinforced by randomly scattered flax fibre be used in structural applications? *Composites Science and Technology*, **67**, 462–470 (2007).
- [16] Martin O., Avérous L.: Poly(lactic acid): plasticization and properties of biodegradable multiphase systems. *Polymer*, **42**, 6209–6219 (2001).
- [17] Avérous L., Moro L., Dole P., Fringant C.: Properties of thermoplastic blends: starch-polycaprolactone. *Polymer*, **41**, 4157–4167 (2000).
- [18] Avérous L., Fringant C.: Association between plasticized starch and polyesters: processing and performances of injected biodegradable systems. *Polymer Engineering and Science*, **41**, 727–734 (2001).
- [19] Huneault M. A., Li H.: Morphology and properties of compatibilized polylactide/thermoplastic starch blends. *Polymer*, **48**, 270–280 (2007).
- [20] Avérous L., Fauconnier N., Moro L., Fringant C.: Blends of thermoplastic starch and polyesteramide: processing and properties. *Journal of Applied Polymer Science*, **76**, 1117–1128 (2000).
- [21] Schwach E., Avérous L.: Starch-based biodegradable blends: Morphology and interface properties. *Polymer International*, **53**, 2115–2124 (2004).
- [22] Huang M-f., Yu J-g., Ma X-f., Jin P.: High performance biodegradable thermoplastic starch-EMMT nanoplastics. *Polymer*, **46**, 3157–3162 (2005).
- [23] Huang M., Yu J., Ma X.: High mechanical performance MMT-urea and formamide-plasticized thermoplastic cornstarch biodegradable nanocomposites. *Carbohydrate Polymers*, **63**, 393–399 (2006).
- [24] Huang M-F., Yu J-G., Ma X-F.: Studies on the properties of montmorillonite reinforced thermoplastic starch composites. *Polymer*, **45**, 7017–7023 (2004).
- [25] Delville J., Joly C., Dole P., Bliard C.: Influence of photocrosslinking on the retrogradation of wheat starch based films. *Carbohydrate Polymers*, **53**, 373–381 (2003).
- [26] Zhai M., Yoshii F., Kume T.: Radiation modification of starch-based plastic sheets. *Carbohydrate Polymers*, **52**, 311–317 (2003).
- [27] Silva M. C., Ibezim E. C., Ribeiro T. A. A., Carvalho C. W. P., Andrade C. T.: Reactive processing and mechanical properties of cross-linked maize starch. *Industrial Crops and Products*, **24**, 46–51 (2006).

# Machining of glass fiber reinforced polyamide

F. Quadrini, E. A. Squeo\*, V. Tagliaferri

Department of Mechanical Engineering, University of Rome Tor Vergata, Via del Politecnico n°1, 00133 Rome, Italy

Received 27 July 2007; accepted in revised form 24 October 2007

**Abstract.** The machinability of a 30 wt% glass fiber reinforced polyamide (PA) was investigated by means of drilling tests. A disk was cut from an extruded rod and drilled on the flat surface: thrust was acquired during drilling at different drilling speed, feed rate and drill diameter. Differential scanning calorimetry (DSC) and indentation were used to characterize PA so as to evaluate the intrinsic lack of homogeneity of the extruded material. In conclusion, it was observed that the chip formation mechanism affects the thrust dependence on the machining parameters. A traditional modeling approach is able to predict thrust only in presence of a continuous chip. In some conditions, thrust increases as drilling speed increases and feed rate decreases; this evidence suggests not to consider the general scientific approach which deals the machining of plastics in analogy with metals. Moreover, the thrust can be significantly affected by the workpiece fabrication effect, as well as by the machining parameters; therefore, the fabrication effect is not negligible in the definition of an optimum for the machining process.

**Keywords:** polymer composites, machining, drilling, cutting forces

## 1. Introduction

Machining of polymers is employed when the quantity of items does not justify the cost for molds, or when a product needs a costly dimensional accuracy. As high performance polymers have been increasingly used for a large number of industrial applications, the machining quality is becoming a central factor for the development of new processes and materials. Nevertheless, the knowledge about the polymer behavior under machining is very limited, as well as the definition of suitable models for the prediction of cutting forces. In the scientific literature, machining of plastics is poorly treated. In the oldest references, an experimental approach is preferred, assuming that plastics behave as metals. In 1967, a significant effort was given by Kobayashi, who collected several experimental observations in his book ‘Machining of plastics’ [1]. This text has been considered a reference for a long time in this field. Also the latest scientific reviews mention it to show the dependence of the

cutting forces on process parameters. For example, in 1977, Roy and Basu defined generalized equations for evaluating the main cutting force and the surface roughness in terms of cutting speed, feed, depth of cut and tool-nose-radius in turning Nylon 6 and Teflon [2]. In conclusion, they assessed that, in general, turning of thermoplastics does not differ greatly from turning of metals. Nowadays, this statement seems to be absolutely erroneous as polymers behave in a completely different way as compared to metals. However, a significant contribution in the study of polymer behavior was given by Ferry in his book ‘Viscoelastic properties of polymers’. Even if it does not deal directly with machining, a lot of experimental and theoretical observations are reported in this book. Those are not in agreement with the assumption of a similar behavior of polymers and metals under machining; for polymers, it is mandatory to consider the time-dependent properties, the time-temperature superposition and the never neg-

\*Corresponding author, e-mail: [squeo@ing.uniroma2.it](mailto:squeo@ing.uniroma2.it)  
© BME-PT and GTE

ligible viscous behavior [3]. Probably, this effort could not be completely received by Kobayashi, who was studying polymer machining in the same period, as well as by Roy and Basu that continued the same experimental approach. Nevertheless, it is very singular that also subsequently the analogy between plastics and metals continued to exist.

In 1993 Hocheng *et al.* studied the machinability of some reinforced thermosets and thermoplastics in drilling [4]. They discussed the chip characteristics and the specific cutting energy to reveal the mechanism of material removal. They observed that the level for fiber loading and the deformation behavior of matrix polymer determine the extent of plasticity in chip formation and the chip length. In a further study, they also observed that, drilling fiber reinforced-thermoplastics, the edge quality is generally fine except in the case of concentrated heat accumulation at tool lips, which is generated by high cutting speed and low feed rate [5].

In 1995, Alauddin *et al.* summarized a lot of experimental observations in their review, without any correlation between the result of a machining operation and the machined material properties [6]. In 1999, Eriksen studied the influence of cutting parameters on the surface roughness of a machined short fiber reinforced thermoplastic [7] that was in turn correlated with the mechanical strength [8].

Recently, in 2002, Xiao and Zhang investigated the role of viscous deformation in machining of polymers, but all the theoretical treatment was derived from metals [9]. Moreover, the viscous effect was taken into account only by means of the glass transition temperature. It is evident that this parameter is not sufficient to completely justify the complex mechanisms at the basis of polymer behavior under machining. Because of the emerging interest about high performance polymers, in 2005, Kim *et al.* studied the effect of the consolidation process on the drilling performance and machinability of PIXA-M and PEEK thermoplastic composites [10]. They observed that the fabrication process can significantly affect the material machinability, as the induction-processed composite material produced equivalent or better holes than the autoclave-processed composites. Moreover they also discussed unique chip characteristics during drilling both autoclaved and induction heat-pressed thermoplastic composites. In 2006 Mata *et al.* studied the physical cutting of polyamide composites by means of the theoretical model of Merchant [11].

This study was extended in 2007 by Davim *et al.* [12]. Turning tests were carried out on large diameter rods (50 mm) of unfilled PA6 and 30 wt% glass fiber filled PA66. However, they did not consider the effect of fiber orientation distribution on cutting forces. In 2003 Sanomura had already discussed this aspect [13]. Studying the fiber orientation of short-fiber reinforced thermoplastics, he observed a change in radial distribution in the extruded materials. In such cases, few fibers perpendicular to the extrusion direction are present in the central region and many fibers parallel to the extrusion direction are present in the surface region.

As previously mentioned, almost only the reported works are available on the machining of thermoplastics. Also in these cases, plastics to machine are never analyzed by means of the techniques typical for polymers (as the differential scanning calorimetry) because of the analogy with metals, that are generally studied by means of different techniques. In the traditional approach [2], the thrust force  $F$  could be modeled as a function of the cutting speed ( $v$ ) and feed rate ( $f$ ) by Equation (1):

$$F = Kv^\alpha f^\beta \quad (1)$$

where  $K$ ,  $\alpha$ , and  $\beta$  are constant.

Many more studies deal with machining of continuous fiber composites with thermosetting matrix. For example, a significant contribution was already given in 1990–91 in the study of drilling glass fiber [14] and aramid [15, 16] composites.

In this work, the authors studied the machinability of a glass fiber reinforced polyamide by means of drilling tests. As a complex fiber orientation distribution is expected in the material, drills were performed on the same disk and in two different configurations: along the disk radius at constant cutting speed and feed rate, and along the external periphery at different values of cutting speed and feed rate. Calorimetry and indentation were used to quantify the lack of homogeneity of the material. A significant trend in mechanical properties was measured along the workpiece because of the fabrication process; cutting forces seem to be strongly dependent on this property distribution. In conclusion it was also observed that the chip formation mechanism significantly affects the machining result in terms of machined part quality and cutting forces. A traditional approach, Equation (1), was used for modeling thrust and its validity was discussed.

## 2. Materials and methods

A commercial glass fiber reinforced polyamide was used for experimentation (commercially, Tecamid 66 GF30®). A 30 wt% glass fiber content was expected from datasheet as well as a density of 1.35 g/cm<sup>3</sup>, a tensile modulus of 9.7 GPa, a tensile strength of 200 MPa, a thermal conductivity of 0.27 W·m<sup>-1</sup>·°C<sup>-1</sup> and a specific heat capacity of 1.5 J·g<sup>-1</sup>·°C<sup>-1</sup>.

A disk 30 mm thick was cut from a round bar (70 mm of diameter) and used for drilling and characterization tests. In order to make a comparison, a disk of unfilled PA66 with the same dimensions was also used in the experimentation.

In Figure 1 the configuration of the drilling tests is shown (Figure 1a) together with the experimental apparatus used (Figure 1c) and a typical acquired drilling curve (Figure 1b). A vertical-spindle knee-and-column type milling machine was used, equipped with a 24 kW high speed spindle. The spindle rotational speed was changed by means of an inverter and measured by an optical system. Therefore both drilling speed and feed rate could be changed during experimentation. Two drills were used having diameter of 5 and 2.5 mm; the drilling speeds were 2500, 5000, 10 000 and 20 000 rpm; the feed rates were 29, 57.5 and 100.5 mm/min. All the combinations of the mentioned parameters were considered making holes in proximity of the external disk circumference. Fixing the drilling speed at 2500 rpm and the feed rate at 100.5 mm/min, the holes were also made along two disk radii using both drills. Because of the difference in diameter, 4 holes were made by the 5 mm drill and 8 holes by the 2.5 mm drill. No coolant was used. A load cell

(Kistler 9273) was placed on the table of the milling machine to measure the thrust during drilling. The workpiece was clamped to a vice, which was in turn fixed to the load cell. The load cell signal was amplified and sent to a data acquisition system. A single thrust value was extracted from each test, performing the average of the acquired cutting data, except for the initial and the final stages.

DSC tests were performed on 10 samples extracted along the disk radius, from the center to the external circumference. The DSC scans (by Netzsch DSC 200 PC) were carried out from room temperature to 280°C at 10°C/min, and peak temperature and area (i. e. the melting temperature and heat) were extracted. The instrument uncertainty can be estimated to be about 1°C for the temperature measurement and 5% of the measured value for the melting heat.

In order to locally characterize the workpiece mechanical properties, indentation tests [17, 18] were carried out along the disk diameter using a universal material testing machine (MTS Alliance RT/50), equipped with an indenter holder. A flat WC indenter with a diameter of 1 mm was set in the holder and 23 indentations were performed, 3 mm spaced each one from the other. During the tests, the applied load and the penetration depth were acquired. The instrument uncertainty for the force evaluation was 0.05% of the measured value. The indentations were performed at the test rate of 10 mm/min and the penetration depth was 1.2 mm. A pre-load of 50 N was applied; this value was optimized to reduce the initial non-linearity of the curves, due to the absence of a perfect parallelism

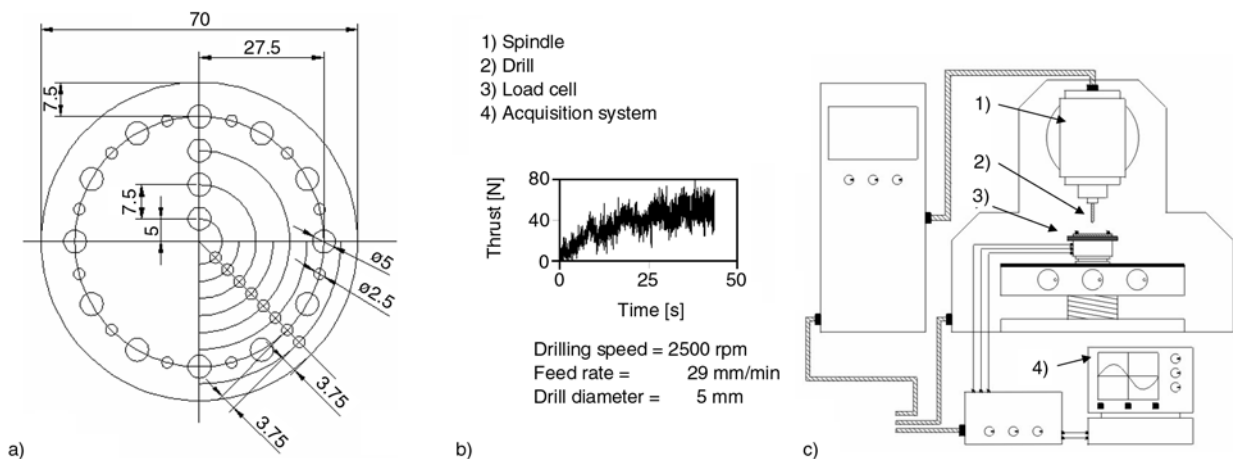


**Figure 1.** Drilling tests: a) configuration of tests; b) typical acquired curve during drilling; c) experimental apparatus for drilling

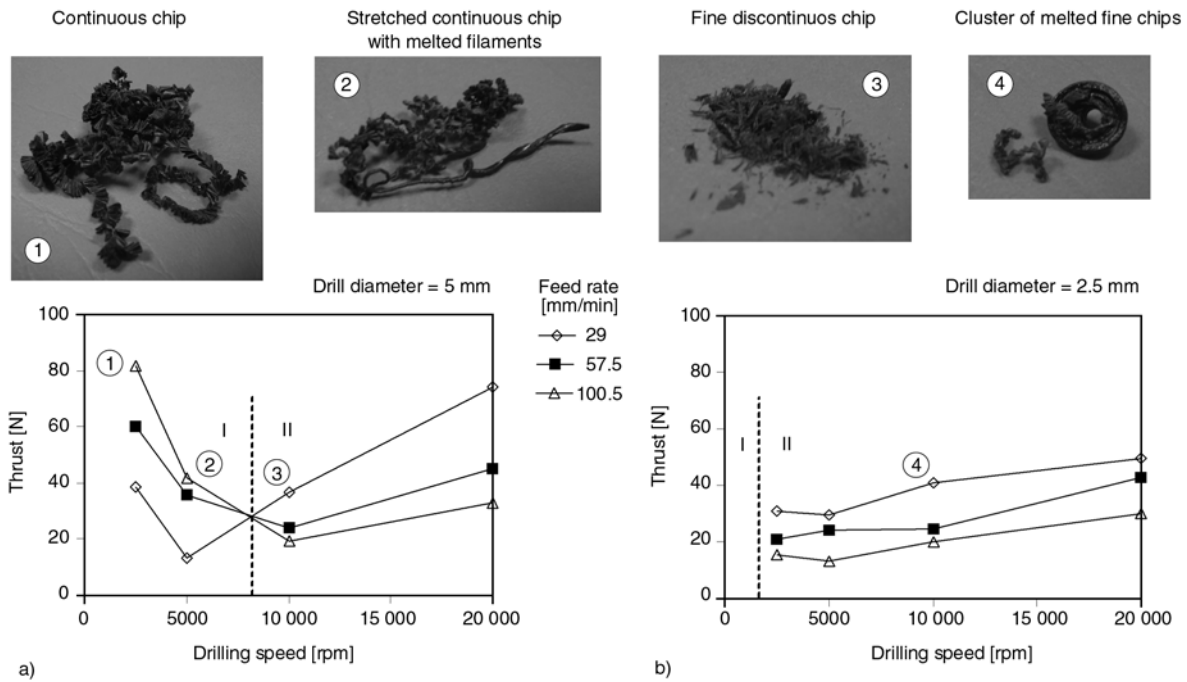


**Figure 2.** Drilling test results and aspect of the chip: thrust dependence on cutting speed and feed rate for the drill with diameter of a) 5 mm and b) 2.5 mm

between the disk and the indenter surfaces. From indentation curves, the initial curve slope (in the range 0–0.1 mm) and the load at the penetration depth of 1 mm were extracted.

### 3. Experimental results

Figure 2 shows the results of the drilling tests performed at the same distance from the center (27.5 mm), changing drill diameter, drilling speed and feed rate. In the same figure the typical aspect of the chip is also reported. Four different chip shapes were observed during tests. A continuous chip was obtained at low drilling speeds only for the 5 mm drill. Increasing the drilling speed, the chip tends to be highly stretched and, in some cases, starts to melt. Increasing again the drilling speed, the chip is discontinuous and enormously reduced in size. In the considered range for the drilling speed and feed rate, a continuous chip was never observed for the 2.5 mm drill. At drilling speed of 2500 rpm, the chip is already discontinuous and, increasing the drilling speed, the heat generation is so severe to cause the chip agglomeration in a cluster. This cluster can remain fixed to the drill or to the workpiece, affecting significantly the surface quality of the hole.

In Figure 3 the thrust is reported as a function of the distance from the disk center for both drills. In this case the drilling speed was fixed at 2500 rpm and

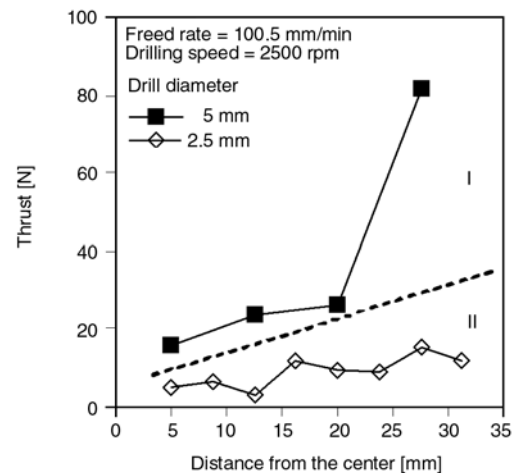


**Figure 3.** Drilling test results: thrust dependence on the distance from the disk center

the feed rate at 100.5 mm/min. In these machining conditions, a continuous chip was observed for the 5 mm drill and a discontinuous chip for the 2.5 mm drill.

DSC test results are summarized in Figure 4 where the scans are compared (Figure 4a) and the peak temperature and melting heat are extracted (Figure 4b). Finally, in Figure 5 the indentation results are shown. A comparison is given between two curves for which a high difference was observed (Figure 5a). Moreover, the trends of the indentation load at 1 mm and the indentation curve slope are both presented (Figure 5b and 5c).

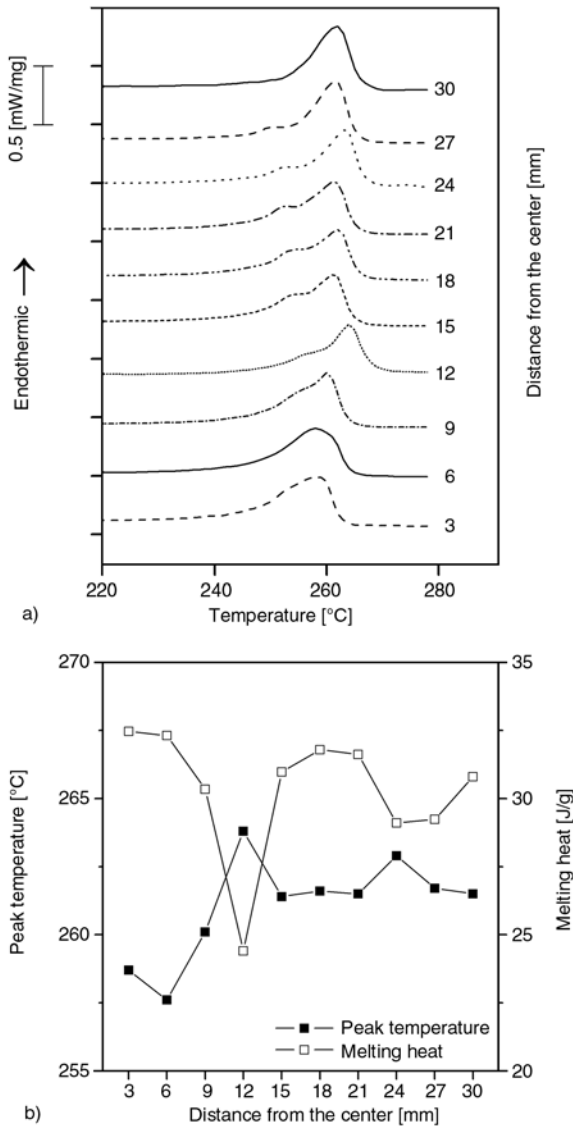


**Figure 4.** DSC test results: effect of the distance from the center on a) the melting peak shape and b) the peak temperature and area

Drilling and indentation tests were performed also on the unfilled PA disk. The disk was drilled along the radius at the drilling speed of 5000 rpm and the feed rate of 100.5 mm/min by using a drill of 5 mm. The cutting conditions were chosen to have a continuous chip but a significant trend was not observed. A thrust of  $25.4 \pm 0.5$  N was measured (for 4 holes), and an indentation load of  $465 \pm 7$  N (for 23 indentations).

#### 4. Discussion

The behavior of a polymer under machining is quite complex and the addition of a structural filler is a further complication. Generally for metals, cutting forces increase when the feed rate increases and the drilling speed decreases, as a higher amount of material is removed. For the reinforced PA considered in this study, the chip formation mechanism seems to play a significant role in determining the cutting forces, in disagreement with metals. Drilling at the same distance from the center, the same mechanical properties are expected in the workpiece material, therefore it is possible to assume that the observed differences in thrust are only dependent on the process parameters. Using a 5 mm drill, at low drilling speeds (up to 5000 rpm), the thrust dependence on the feed rate and drilling speed is in agreement with metals (Figure 2a). The thrust increases by increasing the feed rate or by decreasing the cutting speed. In these machining conditions, a continuous fluent chip is obtained. Increasing the drilling speed over 5000 rpm, the thrust suddenly increases and higher values are obtained at lower values of feed rate. In these conditions the chip is small and discontinuous. Evidently, the chip is too small to provide a good heat

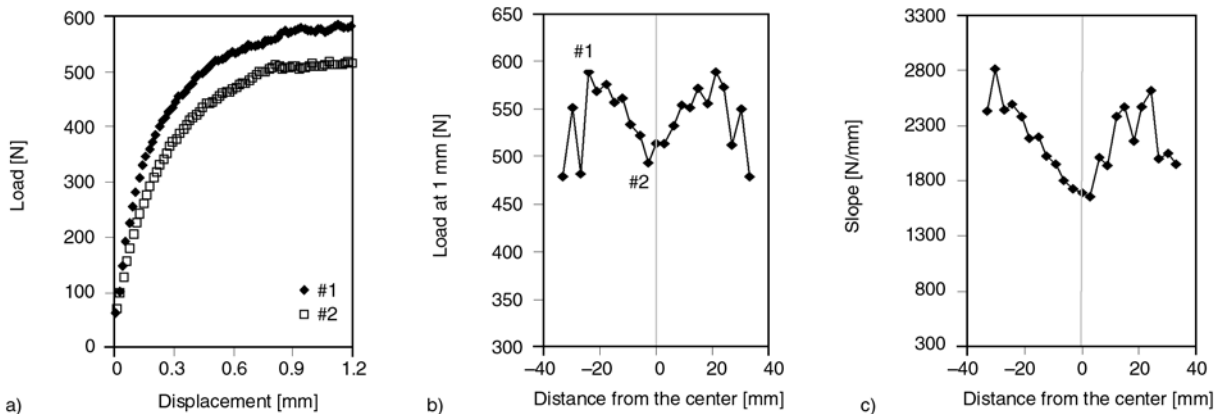


**Figure 5.** Indentation test results: a) comparison between two indentation curves at different distance from the disk center; b) indentation load at 1 mm and c) indentation curve slope as a function of the distance from the disk center

removal from the machining zone and the cutting mechanism is significantly affected by the excessive temperature increase. It is possible to recognize two main chip formation mechanisms: (I) a continuous chip and (II) a discontinuous chip. The transition between the two mechanisms is not sharp as the chip appears, in some cases, highly stretched and with some melted filaments. At very high drilling speeds, the temperature increase in the machining zone can be so severe to generate a cluster of melted chips that damages the hole quality.

Using a 2.5 mm drill (Figure 2b), a drilling speed of 2500 rpm is already too high to have a continuous chip and only the chip formation mechanism (II) is observed. In this case, thrust increases with the drilling speed and decreases with the feed rate, in opposition to metals.

The effect of the workpiece fabrication process is not negligible in the definition of the cutting forces. Making holes along the disk radius, a higher thrust is measured far from the center (Figure 3). This result was obtained for both drills, even if in the case of the 2.5 mm drill the trend is probably altered by the poor chip formation mechanism. Using the 5 mm drill, the dependence is clear and the thrust can be 8 times higher in the disk periphery compared to the center. A similar trend was not observed for the unfilled PA for which thrust seems to be not dependent on the distance from the center. The higher homogeneity of the unfilled PA was also shown by the indentation results. This occurrence suggests that the thrust mainly depends on the fiber distribution.

In order to investigate the experimental evidence of the thrust increase along the radius, DSC and indentation tests were carried out. Moving from the center toward the periphery, the melting peak is significantly different in shape (Figure 4a). A double melting peak is generally present in all the scans, but the peaks are more separated in the half radius zone. The melting temperature is lower near the center and increases toward the periphery, even if a plateau is already reached at half radius. As the material was extruded through a very thick die, a large difference in crystallization speed between the core and the skin is expected. This phenomenon, together with the local concentration and orientation of fibers, affects the DSC results.

The lack of homogeneity observed by means of DSC was confirmed by the indentation tests. In Figure 5a, a comparison is given between two

indentation curves: the first performed near the disk periphery and the second near the center. In detail, the penetration load at 1 mm (Figure 5b) and the initial curve slope (Figure 5c) were taken into account. The indentation load shows a symmetric distribution along the diameter with the maximum toward the half radius; the curve slope trend is similar, even if the symmetry of the results is affected by data scattering. Because of the heterogeneous nature of the material and because of the small dimension of the indenter, data scattering is not eliminable. However, from the comparison between Figures 5b and 5c a clear trend in mechanical properties can be extracted, with a minimum toward the center and a maximum toward the half radius. The trend of the indentation load is probably dependent on the fiber distribution and orientation. In fact reported data are in agreement with the distribution orientation discussed in [13] except for the sudden drop near the disk periphery.

In the external periphery, in the last 10 mm, another minimum is observed. Considering that this external part was not completely involved in drilling, the trend of the thrust in Figure 3 is analogous to the trend of the indentation load in Figure 5b.

The typical approach for modeling is not able to predict the thrust dependence on cutting speed and feed rate in the case of chip formation (II). This occurrence was never discussed in the scientific literature and depends on the combination of several factors: the viscoelastic behavior of the material, the temperature increase during machining and its effect on the material viscosity, the fiber orientation and distribution. However, Equation (1) can be used for the prediction of thrust in the case of continuous chip (I). In fact Figure 6 shows the comparison between experimental and numerical predicted data by means of (1). Only 6 experimental points are present as in the other cases a discontinuous chip was observed. In Figure 6, the equation used for the prediction of the thrust is also reported; the correlation coefficient between experimental and numerical data is 0.93.

## 5. Conclusions

Polymers behave unlike metals and this difference has to be considered in all the aspects of their processing, also for machining. Performing drilling tests, it was obtained that the dependence of the thrust on the process parameters is significantly affected by the chip formation mechanism. If the

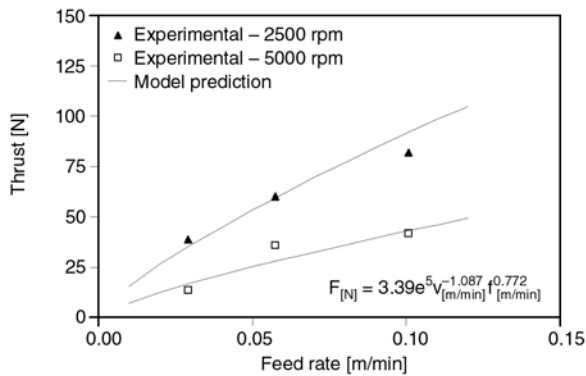


**Figure 6.** Experimental results and numerical predictions in the case of continuous chip (drill of 5 mm)

chip is discontinuous, thrust increases with drilling speed and decreases with feed rate. This occurrence was never discussed in the scientific literature. Unlike metals, increasing cutting speed does not result in a better machining process. In such conditions, i. e. for a continuous chip, a traditional model (typical of metals) can be used for the prediction of cutting forces. If a different mechanism of chip formation is activated, the traditional approach can lead to significant errors.

Moreover, the fabrication effect of the workpiece can influence the cutting forces more than the process parameters. The thrust increases by a factor of 8 from the center of the considered disk toward the external circumference, due to fiber orientation and distribution. If turning tests are used for the definition of a cutting load, this occurrence could significantly affect results. However, local indentation tests can help to enhance the effectiveness of modeling procedures and machining processes. If the material behavior under machining is not taken into account, poor tolerances would be obtained and the total cost of the part production would be unacceptable.

### Acknowledgements

The authors are grateful to Dr Gianluca Palazzo for his support in experimentation.

### References

[1] Kobayashi A.: Machining of plastics. McGraw-Hill, New York (1967).  
 [2] Roy P. K., Basu S. K.: Evaluation of processing factors on turning of thermoplastics. *Polymer Engineering and Science*, **17**, 751–757 (1977).

[3] Ferry J. D.: Viscoelastic properties of polymers, 3<sup>rd</sup> edition. Wiley, New York (1980).  
 [4] Hocheng H., Pwu H. Y., Yao K. C.: On drilling characteristics of fiber-reinforced thermoset and thermoplastics. *Materials and Manufacturing Processes*, **8**, 653–682 (1993).  
 [5] Hocheng H., Puw H. Y.: Machinability of fiber-reinforced thermoplastics in drilling. *Journal of Engineering Materials and Technology*, **115**, 146–149 (1993).  
 [6] Alauddin M., Choundhury I. A., El Baradie M. A., Hashmi M. S. J.: Plastics and their machining: a review. *Journal of Materials Processing Technology*, **54**, 40–46 (1995).  
 [7] Eriksen E.: Influence from production parameters on the surface roughness of a machined short fibre reinforced thermoplastic. *International Journal of Machine Tools and Manufacture*, **39**, 1611–1618 (1999).  
 [8] Eriksen E.: The influence of surface roughness on the mechanical strength properties of machined short-fibre-reinforced thermoplastics. *Composites Science and Technology*, **60**, 107–113 (2000).  
 [9] Xiao K. Q., Zhang L. C.: The role of viscous deformation in the machining of polymers. *International Journal of Mechanical Sciences*, **44**, 2317–2336 (2002).  
 [10] Kim D., Ramulu M., Doan X.: Influence of consolidation process on the drilling performance and machinability of PIXA-M and PEEK thermoplastic composites. *Journal of Thermoplastic Composite Materials*, **18**, 195–217 (2005).  
 [11] Mata F., Reis P., Davim J. P.: Physical cutting model of polyamide composites (PA66 GF30). *Materials Science Forum*, **514–516**, 643–647 (2006).  
 [12] Davim J. P., Mata F.: A comparative evaluation of the turning of reinforced and unreinforced polyamide. *International Journal of Advanced Manufacturing Technology*, **33**, 911–914 (2007).  
 [13] Sanomura Y., Kawamura M.: Fiber orientation control of short-fiber reinforced thermoplastics by ram extrusion. *Polymer Composites*, **24**, 587–596 (2003).  
 [14] Tagliaferri V., Caprino G., Diterlizzi A.: Effect of drilling parameters on the finish and mechanical properties of GFRP composites. *International Journal of Machine Tools and Manufacturing*, **30**, 77–86 (1990).  
 [15] Di Ilio A., Tagliaferri V., Veniali F.: Cutting mechanisms in drilling of aramid composites. *International Journal of Machine Tools and Manufacturing*, **31**, 155–165 (1991).  
 [16] Di Ilio A., Tagliaferri V., Veniali F.: Tool life and hole quality in drilling aramid and fibrous composites. *Composite Material Technology*, **37**, 203–207 (1991).  
 [17] Cheng L., Xia X., Yu W., Scriven L. E., Gerberich W. W.: Flat-punch indentation of viscoelastic material. *Journal of Polymer Science, Part B: Polymer Physics*, **38**, 10–22 (2000).  
 [18] Benabdallah H. S., Bui V. T.: Indentation of poly(formaldehyde), reinforced nylons and poly(ethyl terephthalate). *Polymer Engineering and Science*, **44**, 1439–1447 (2004).

# Injection molding of bushes made of tribological PEEK composites

F. Quadrini\*, E. A. Squeo

Department of Mechanical Engineering, University of Rome Tor Vergata Via del Politecnico n°1, 00133 Rome, Italy

Received 27 July 2007; accepted in revised form 24 October 2007

**Abstract.** Polyetheretherketone (PEEK) composites have been extensively studied because of the excellent tribological behavior among plastics. However, laboratory specimens and tests are generally discussed, whereas application studies on industrial components are infrequent. In this paper, an injection molded bush made of tribological PEEK was analyzed to correlate wear behavior and molded material structure. Bushes were tested under unlubricated sliding conditions by means of a short wear test. Surface analysis, differential scanning calorimetry (DSC) and optical microscopy were used to evaluate the distribution of the different composite fillers (polytetrafluoroethylene, PTFE, graphite particles and carbon micro-fibers) and their effect on the final bush behavior. A significant lack of homogeneity was observed in the molded bush and black bands appeared on the shaft surface after testing due to the sliding. The bush geometry and the injection molding process should be optimized to allow the best tribological behavior of the molded material under working conditions.

**Keywords:** polymer composites, injection molding, PEEK, bushes

## 1. Introduction

High performance polymers are used for a lot of industrial applications because of their excellent mechanical properties that are preserved also at high temperatures. Polyetheretherketone is probably the most attractive among high performance polymers, even if its use is limited by the high cost of supplying and processing and by the high sensitivity to the molding processes. PEEK is generally used as matrix for high performance composites. Tribological components (such as bushes and gears) can be fabricated by injection molding of a PEEK matrix composite, filled with polytetrafluoroethylene (PTFE), graphite particles and carbon micro-fibers. The maximum amount of filler is generally limited to 30 wt% to avoid problems during injection; PTFE and graphite enhance the tribological behavior of the molded part, whereas the carbon

fibers are responsible for the high mechanical performances.

Injection molding is not the only method for making slide-bearing bushes of PEEK composites. In many industrial applications, machining is preferred because of the maintenance and the small-medium scale production series. Injection molded parts are often not allowed to operate due to uneven stress distribution, whereas machined parts tribologically perform better. However, for large scale production series, the injection molding is the only possible choice for bush making and problems related to the lower performances could limit significantly the use of these materials.

In the scientific literature there are a lot of works about the tribology of PEEK, its blends and its composites because of the high industrial interest in these materials. These materials are generally tested under dry sliding conditions [1–4]. Solid particle erosion behavior during sliding [5] and the

\*Corresponding author, e-mail: [quadrini@ing.uniroma2.it](mailto:quadrini@ing.uniroma2.it)  
© BME-PT and GTE

correlation between mechanical properties and tribology performance [6, 7] were also deeply discussed. Due to the complexity of the problem, statistical techniques [8] and neural networks [9] were used to study the effect of test parameters on the dry sliding tribological behavior. Moreover, thermal aging can significantly affect the tribological performance of PEEK and short fiber reinforced PEEK composites [10].

The investigation on the tribology performance of PEEK, PEEK blends and composites was also extended to water lubricated sliding contacts [11–15], different wear modes [16] and harsh operating conditions [17]. In order to obtain the best tribological behavior, the effect of nano-fillers was discussed (SiC [18, 19], alumina [20–21] and PTFE [20] nano-particles, carbon nanofibers [22], nanotubes and nano-onions [20]).

The mentioned papers show that PEEK composites have excellent tribological performance among plastics, but the correlation between the injection molding technology and the tribological performance of the molded part has never been investigated. Small laboratory specimens are generally preferred. In 2002, Zsidai *et al.* deeply discussed advantages and disadvantages of small-scale tribotesting [23]. In 2005, Samyn and De Baets studied the friction and wear of acetal, focusing on the effect of the specimen scale on the final measured properties [24]. They assessed that to obtain relevant data for practical design of polymer sliding parts, it is necessary to simulate real working conditions as close as possible on laboratory scale. However, they did not discuss that, besides the specimen scale, also the molding process can affect the result of friction and wear tests. In order to avoid scale problems, a purely experimental approach is often used. Plastic gears made of carbon fiber reinforced PEEK [25–26] or acetal [27–28] were directly tested in working-like conditions. A similar study was never performed on slide-bearing bushes.

In the current work, the authors investigate the capability of a bush made of PEEK composite to substitute a traditional bush made of brass. All the mentioned scientific papers show the high tribological properties of this material, but they do not discuss application cases. Therefore, it is not obvious that injection molded bush behavior under working conditions could be satisfactory.

## 2. Materials and methods

Commercial bushes were acquired by a manufacturer who started to produce the component depicted in Figure 1 in several high performance polymers. This bush was designed for small size electric motors instead of a traditional brass because of the low weight and production time. The two cavity mold was adapted to injection mold the bush in PEEK 450 FC 30 (by Victrex, USA) which is a 10 wt% carbon fiber, 10 wt% graphite, 10 wt% PTFE filled PEEK. PEEK 450 FC 30 is a commercial material developed for injection molding and investigated in some scientific studies [4–6, 14]. At room temperature, it has a tensile modulus of 10.1 GPa, a tensile strength of 134 MPa, a thermal conductivity of  $0.78 \text{ W}\cdot\text{m}^{-1}\cdot\text{C}^{-1}$  and a specific heat capacity of  $1.8 \text{ kJ}\cdot\text{kg}^{-1}\cdot\text{C}^{-1}$ . The manufacturer assured that the molding conditions suggested by the material supplier were observed (mainly the melt temperature of  $380^\circ\text{C}$  and the mold temperature of  $180^\circ\text{C}$ ).

The bushes were used for a short wear test and for material analyses. The wear test was carried out keeping the bush in a standstill position and matching a stainless steel shaft (Figure 2). The shaft was fixed coaxially to the rotor of an electric motor and was put into rotation at 3000 rpm for 10 min. As the shaft diameter was 6 mm, the resulting sliding speed was 0.942 m/s. The bush was mounted on the shaft without interference, therefore a minimum load was present on it in dependence of the weight of the electric motor that was shared by the supports. As an approximation, the load on the bush was about 10 N and the consequent  $p\dot{v}$  (pressure-speed) value was  $0.10 \text{ MPa}\cdot\text{m/s}$ .

During the test, the bush temperature was acquired by means of a BS1843 standard type K thermocou-

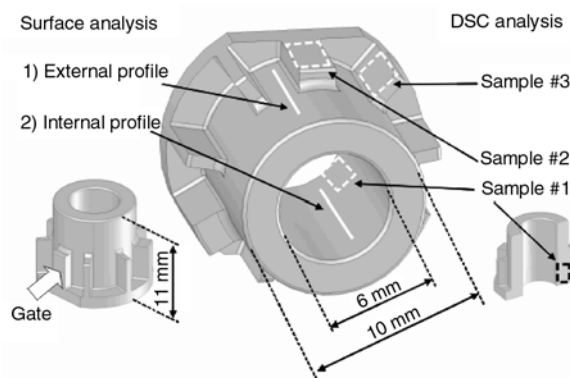


**Figure 1.** Molded bush dimensions and position of surface and DSC analyses

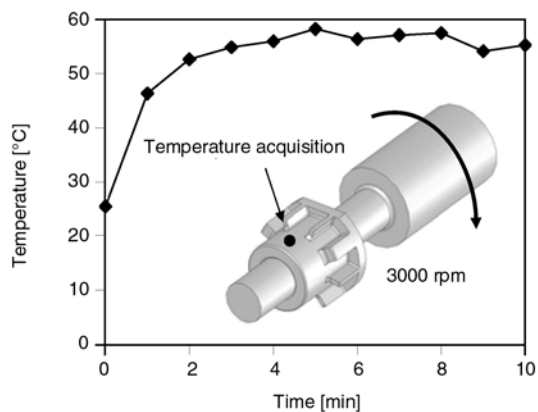


**Figure 2.** Configuration of the short wear test and temperature acquisition during the test

ple placed on the external surface. A typical temperature curve is reported in Figure 2; after 5 min a plateau is already reached about 55°C, which is relatively low for this material (the continuous mechanical use temperature without impact is 240°C). Ten bush-shaft couples were used in the short wear test. A surface analysis was performed on a bush by means of a scanning surface topography instrument (by Taylor Hobson, Talysurf CLI 2000). As Figure 1 shows, two external lines were chosen for the profile acquisition, the first along the height of the internal cylindrical surface and the second along the height of the external surface. The internal profile was acquired both before and after the short wear test. Also the shaft profile was acquired along the height of the bearing zone.

Some samples were extracted from a bush to carry out DSC tests (by Netzsch DSC 200 PC). In Figure 1 the position of the samples is shown. DSC tests were carried out from room temperature to 400°C at 10°C/min. Other bushes were cut and prepared for optical microscopy.

### 3. Experimental results

Several bush-shaft couples were used in the short wear test and always the same result was obtained for the shaft: some black bands appeared on the shaft after a few seconds during the test. These bands were not removable by conventional clean-

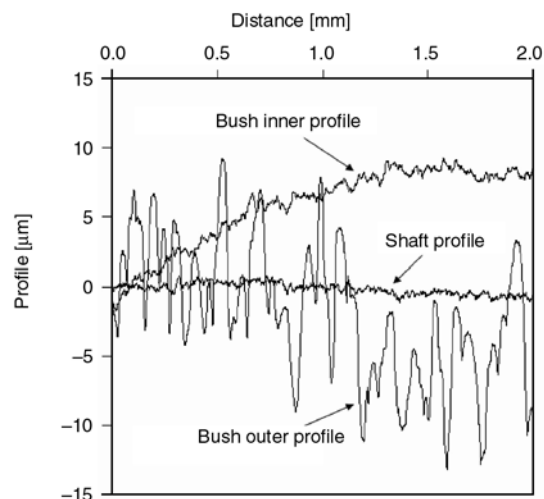


**Figure 3.** Acquired profiles of the molded bush and the steel shaft before the short wear test

ing techniques (such as ultrasounds) but only by machining. The same bushes were used for the microscopical analyses.

The roughness profiles of a bush and a shaft, acquired before the short wear test, are reported in Figure 3. In this figure, the raw data are shown without any filtering and the sample positioning is responsible for the trend. In Table 1 the roughness data extracted from the profiles are collected before and after the test. In Figure 4 the DSC scans performed on 3 samples extracted from the bush are shown. In Figure 5 one of these scans (sample #1 of Figure 1) was compared with two scans performed

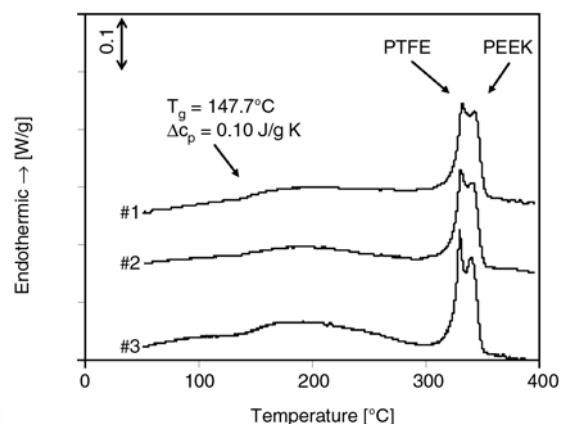


**Figure 4.** DSC scans performed on samples extracted in different points of the bush

**Table 1.** Results from surface analysis of the bush, before and after the short wear test

	Bush profile			Shaft	
	External	Internal		(Before test)	(After test)
		(Before test)	(After test)		
$R_a$ [µm]	2.53	0.597	0.627	0.174	0.15
$R_t$ [µm]	18	9.73	10.4	2.02	1.42

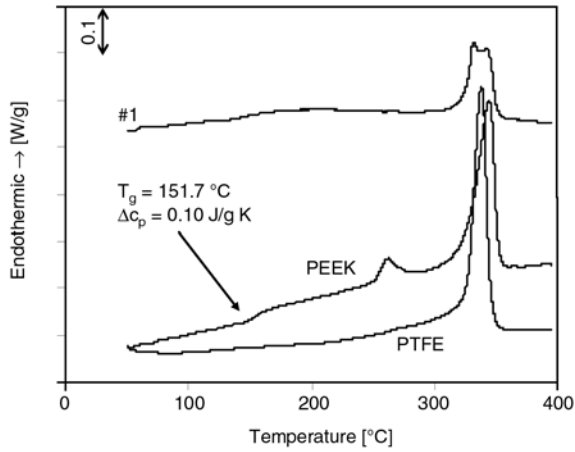


**Figure 5.** Comparison between a DSC scan of a sample extracted from the bush and the scans of PEEK and PTFE bulk samples

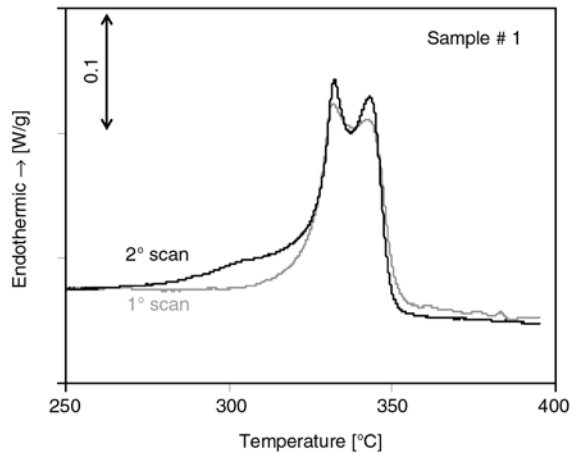


**Figure 6.** Comparison between the first and second DSC scans carried out on the same sample

on bulk PTFE and PEEK that were extracted from commercial bars. In Figure 6 another comparison is shown between two successive DSC scans of the same sample #1. From all the curves of Figures 4–6 both the area of the peak and the temperature of the peak were extracted and reported in Figure 7. The area was calculated after the baseline correction and corresponds to the material melting heat, whereas the temperature is the melting temperature. A double melting peak was observed for all the samples extracted from the bush, therefore two different temperatures are reported for each sample. Figures 8, 9 and 10 show respectively the structure of the molded material in the bulk, the bearing zone and the external surface; in Figure 9 the aspect of the shaft is also superimposed. In conclusion, Figure 11 shows a magnification of the composite structure near the external surface (a) and the bearing zone (b-c).

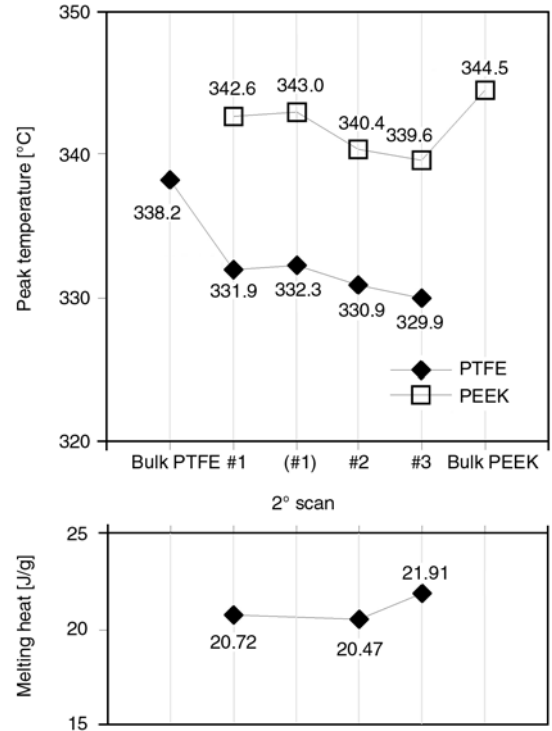


**Figure 7.** Temperature of the peak and melting heat extracted from the DSC scans

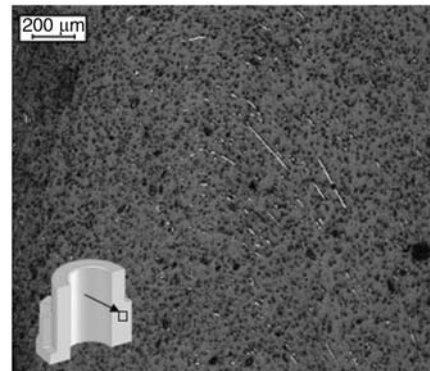


**Figure 8.** Optical micrograph of the bulk molded material

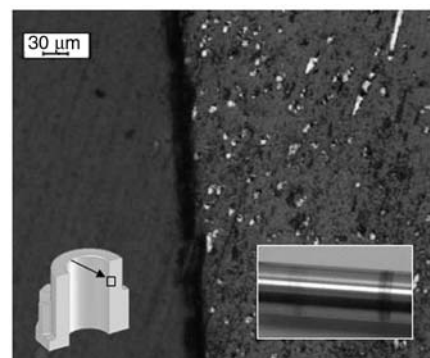


**Figure 9.** Optical micrograph in the bush bearing zone and aspect of the shaft after the wear test

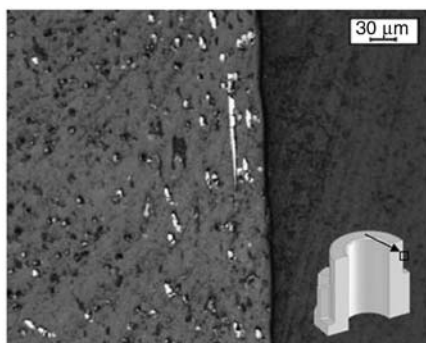


**Figure 10.** Optical micrograph near the bush external surface

#### 4. Discussion

During the wear test, the temperature increases up to 55°C in the first 4 min and then it is almost constant. The temperature is low enough to exclude any possible degradation of the material. Nevertheless a strong interaction occurs between the shaft and the bush due to deposition of PEEK composite debris on the shaft surface.

As expected, the acquired profiles of the bush and the shaft are very different from one another (Figure 3). The shaft profile is the smoothest; the bush internal profile is rougher but enormously smoother than the external profile. Comparing data before and after the test (Table 1), the shaft roughness (in terms of  $R_a$  and  $R_t$ ) decreases because of the test, whereas the bush inner profile becomes rougher. A small amount of material is transferred from the bush to the shaft; the bush is minimally damaged, therefore its roughness increases; the valleys of the shaft profile are filled with the plastic material and so the shaft roughness decreases. This is a typical phenomenon that can be observed during the sliding of steel on a polymeric surface under unlubricated running conditions. A similar phenomenon

was already discussed by Jacobs *et al.* for the same PEEK composite [14]. A transfer film containing carbon fiber debris can form on the steel counterpart and modify the wear curve. They also discussed that in aqueous environment the formation of the transfer film seems to be disturbed by tribo-corrosion. However, the testing conditions were very different in terms of wear test (a ball on-prism tribometer) and sliding speed (28.2 mm/s), even if the  $pv$  term is almost comparable.

DSC analysis allows studying the effect of the injection molding process on the molded material. All the samples present the inflection point related to the PEEK glass transition (at about 150°C) and a double melting peak (Figure 4). The shape of a DSC scan depends, among other things, on the core-skin effect; however the double peak is related to the presence, inside the PEEK matrix, of PTFE which melts at a lower temperature. In fact, in Figure 5 the scan of sample #1 is plotted together with the scan of samples of pure PEEK and pure PTFE. The superposition of the bulk PEEK and PTFE peaks is very similar to the shape of the melting peak of sample #1. Figure 6 shows the comparison between the first and second DSC scans performed on the sample #1. In both scans, two peaks are visible and the difference is negligible. As the first sample melting does not eliminate the presence and the position of the two peaks, these have to be related to the material composition and not to the core-skin effect.

Observing Figure 4, the extent of the PTFE peak is dependent on the amount of PTFE in the sample. PTFE content differs from point to point. This occurrence was never discussed before. The lowest PTFE peak is visible in sample #1, i. e. in the bearing zone. The peak increases in the large rib (sam-

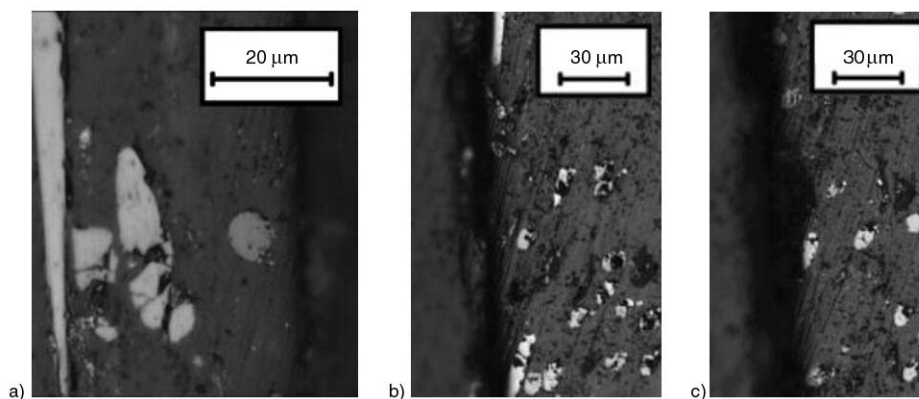


**Figure 11.** Magnification of the micrographs of the bushes after testing: near the external surface (a) and the bearing zone (b–c)

ple #2) and has a maximum in the small rib (sample #3). Actually, the ribs were inserted in the bush geometry only to reproduce the shape of a typical bush made of metal. In fact, many industrial applications deal with the substitution of metallic parts with plastic parts having the same shape, above all for commercial reasons, but also to allow the substitution without any modification in the assembly procedure. A lack of homogeneity in the PTFE distribution can occur because of the complex shape of the bush and other factors, such as the ratio between the viscosities of PEEK and PTFE. Moreover, considering the gate position (Figure 1), during molding carbon fibers are pushed against the bearing zone, rather than toward the ribs. Carbon fibers are present in tribological PEEK mainly to enhance the structural properties; their agglomeration in the bearing zone could be dangerous, PTFE or graphite would be better. DSC data of Figure 7 confirm this statement, as the highest melting heat is measured for sample #3. In fact, melting heat is related to PTFE and PEEK content in the sample, as only these two materials can melt. From Figure 7, it is also clear that the temperatures of the peak are almost constant along the bush, for both materials. Nevertheless, the highest values are observed for the bulk materials, because of the different nature of the polymers.

The injection stage affects the homogeneity of the molded tribological PEEK, as the PTFE, that should help the sliding, is far from the sliding zone, whereas the carbon fibers, that should guarantee the bulk strength, are close to the bearing zone. In order to deepen this aspect, optical microscopy was used to investigate the structure of the molded bushes. In Figure 8 the micrograph of the bulk material is shown: the heterogeneous nature of the PEEK composite is clear. As discussed in [6], the black dots correspond to PTFE; the small shining particles to graphite; the shining filaments to carbon fibers. Due to the injection phase, the carbon fiber orientation is complex. Dealing with PEEK 450 FC 30, previous papers have never investigated the effect of the fiber orientation on transfer film formation and tribological behavior. It is well-known that fibers strongly contribute to the definition of the tribology system but it is hard to understand which is the best orientation distribution. For this reason, testing the real bush in working-like conditions seems to be the only way to investigate its suitability for industrial applications.

In Figure 9 the structure of the composite material near the bearing zone is shown, together with the aspect of the steel shaft after test. After the test, some black parallel bands appear on the shaft due to the transfer film. In Figure 10 the same structure is observed near the external surface. Figures 9 and 10 seem similar, but this similarity disappears after magnification. In the external wall, all the carbon fibers are covered by a thin film of plastic (Figure 11a). In the bearing zone, after a few seconds under working conditions, the same plastic film is removed from the surface by the shaft sliding and the carbon fibers rise (Figures 11b and c). Observing the rising carbon fibers at the internal wall, it is clear that they were leveled by sliding. The transfer film formation damages the bush roughness and alter the aspect of the shaft.

## 5. Conclusions

In the scientific literature, industrial bushes were never investigated; in this paper, a short wear test was performed on a bush made of composite PEEK. The material showed the expected high properties by limiting the maximum bush temperature reached during the test. The transfer film formation was observed, as well as an increase in the bush roughness. Even if the transfer film could improve the tribological behavior of the bush-shaft system, the presence of debris and the increase of the bush roughness could be negative factors. Moreover, in working conditions, tribo-corrosion could occur in aqueous environment, in dependence of the shaft alloy. These phenomena should be taken into account to evaluate the suitability of the PEEK composite bush for industrial applications. For many industrial applications, it is mandatory that no traces can be left by the bush on the shaft surface. In this case, this kind of material should be avoided. However, even if the deposition of a transfer film is accepted, the molding process of the bush in tribological PEEK should be optimized to maximize the expected performance of the composite; on the contrary, in the industrial practice, the molding process is designed only to obtain the desired geometrical tolerances of the molded part. The heterogeneous nature of the composite material could damage the tribological behavior of the bush; after molding, the PTFE and graphite particles (useful to reduce friction) should be agglomerated near the bearing zone; instead the carbon fibers

should be far enough from there. Injection stage and bush geometry have to be designed carefully. The bush geometry used in this study does not seem to be recommendable for industrial application.

## References

- [1] Eiss N. S. J., Hanchi J.: Tribological behavior of polyetheretherketone, a thermotropic liquid crystalline polymer and in situ composites based on their blends under dry sliding conditions at elevated temperatures. *Wear*, **200**, 105–121 (1996).
- [2] Stuart B. H.: Tribological studies of poly(ether ether ketone) blends. *Tribology International*, **31**, 647–651 (1998).
- [3] Zhang M. Q., Zai P. L., Friedrich K.: Thermal analysis of the wear debris of polyetheretherketone. *Tribology International*, **30**, 103–111 (1997).
- [4] Harsha A. P., Tewari U. S.: Tribo performance of polyaryletherketone composites. *Polymer Testing*, **21**, 697–709 (2002).
- [5] Harsha A. P., Tewari U. S., Venkatraman B.: Solid particle erosion behaviour of various polyaryletherketone composites. *Wear*, **254**, 693–712 (2003).
- [6] Zhang Z., Breidt C., Chang L., Friedrich K.: Wear of PEEK composites related to their mechanical performances. *Tribology International*, **37**, 271–277 (2004).
- [7] Long C-G., Wang X-Y.: Mechanical properties and tribology performance of the Ekonol-PEEK composite. *Journal of Reinforced Plastics and Composites*, **23**, 1575–1582 (2004).
- [8] Davim J. P., Cardoso R.: Tribological behaviour of the composite PEEK-CF30 at dry sliding against steel using statistical techniques. *Materials and Design*, **27**, 338–342 (2006).
- [9] LiuJie X., Davim J. P., Cardoso R.: Prediction on tribological behaviour of composite PEEK-CF30 using artificial neural networks. *Journal of Materials Processing Technology*, **189**, 374–378 (2007).
- [10] Sinmazçelik T., Yilmaz T.: Thermal aging effects on mechanical and tribological performance of PEEK and short fiber reinforced PEEK composites. *Materials and Design*, **28**, 641–648 (2007).
- [11] Yamamoto Y., Takashima T.: Friction and wear of water lubricated PEEK and PPS sliding contacts. *Wear*, **253**, 820–826 (2002).
- [12] Yamamoto Y., Hashimoto M.: Friction and wear of water lubricated PEEK and PPS sliding contacts. Part 2. Composites with carbon or glass fibre. *Wear*, **257**, 181–189 (2004).
- [13] Jia J., Chen J., Zhiu H., Hu L.: Comparative study on tribological behaviors of polyetheretherketone composite reinforced with carbon fiber and polytetrafluoroethylene under water-lubricated and dry-sliding against stainless steel. *Tribology Letters*, **17**, 231–238 (2004).
- [14] Jacobs O., Jaskulka R., Yan C., Wu W.: On the effect of counterface material and aqueous environment on the sliding wear of various PEEK compounds. *Tribology Letters*, **18**, 359–372 (2005).
- [15] Unal H., Mimaroglu A.: Friction and wear characteristics of PEEK and its composite under water lubrication. *Journal of Reinforced Plastics and Composites*, **25**, 1659–1667 (2006).
- [16] Bijwe J., Sen S., Ghosh A.: Influence of PTFE content in PEEK-PTFE blends on mechanical properties and tribo-performance in various wear modes. *Wear*, **258**, 1536–1542 (2005).
- [17] Lal B., Alam S., Mathur G. N.: Tribo-investigation on PTFE lubricated PEEK in harsh operating conditions. *Tribology Letters*, **25**, 71–77 (2006).
- [18] Wang Q-H., Xu J., Shen W., Xue Q.: The effect of nanometer SiC filler on the tribological behavior of PEEK. *Wear*, **209**, 316–321 (1997).
- [19] Wang Q-H., Xue Q-J., Liu W-M., Chen J-M.: Effect of nanometer SiC filler on the tribological behavior of PEEK under distilled water lubrication. *Journal of Applied Polymer Science*, **78**, 609–614 (2000).
- [20] McCook N. L., Hamilton M. A., Burris D. L., Sawyer W. G.: Tribological results of PEEK nanocomposites in dry sliding against 440C in various gas environments. *Wear*, **262**, 1511–1515 (2007).
- [21] Qiao H-B., Guo Q., Tian A-G., Pan G-L., Xu L-B.: A study on friction and wear characteristics of nanometer Al<sub>2</sub>O<sub>3</sub>/PEEK composites under the dry sliding condition. *Tribology International*, **40**, 105–110 (2007).
- [22] Werner P., Alstädt V., Jaskulka R., Jacobs O., Sandler J. K. W., Shaffer M. S. P., Windle A. H.: Tribological behaviour of carbon-nanofibre-reinforced poly(ether ether ketone). *Wear*, **257**, 1006–1014 (2004).
- [23] Zsidai L., De Baets P., Samyn P., Kalácska G., Van Peterghen A. P., Van Parys F.: The tribological behavior of engineering plastics during sliding friction investigated with small-scale specimens. *Wear*, **253**, 673–688 (2002).
- [24] Samyn P., De Baets P.: Friction and wear of acetal: A matter of scale. *Wear*, **259**, 697–702 (2005).
- [25] Kurokawa M., Uchiyama Y., Nagai S.: Performance of plastic gear made of carbon fiber reinforced polyether-ether-ketone. *Tribology International*, **32**, 491–497 (1999).
- [26] Kurokawa M., Uchiyama Y., Nagai S.: Performance of plastic gear made of carbon fiber reinforced polyether-ether-ketone: Part 2. *Tribology International*, **33**, 715–721 (2000).
- [27] Kim C. H.: Durability improvement method for plastic spur gears. *Tribology International*, **39**, 1454–1461 (2006).
- [28] Mao K., Hooke C. J., Walton D.: Acetal gear wear and performance prediction under unlubricated running condition. *Journal of Synthetic Lubrication*, **23**, 137–152 (2006).

# Synthesis and characterization of rubbery epoxy/organoclay hectorite nanocomposites

A. Boukerrou<sup>1\*</sup>, J. Duchet<sup>2</sup>, S. Fellahi<sup>3</sup>, H. Djidjelli<sup>1</sup>, M. Kaci<sup>1</sup>, H. Sautereau<sup>2</sup>

<sup>1</sup>Laboratoire des Matériaux Organiques, Université Abderrahmane Mira, Bejaia 06000, Algeria

<sup>2</sup>Laboratoire des Matériaux Macromoléculaires de l'INSA de Lyon, 20 Avenue Albert Einstein, 69621 Villeurbanne-Lyon, France

<sup>3</sup>Département de Génie des Polymères, Institut Algérien du Pétrole (IAP) de Boumerdès 35000, Algeria

Received 2 September 2007; accepted in revised form 6 November 2007

**Abstract.** The present research investigates the morphology, the mechanical, and the viscoelastic properties of rubbery epoxy/clay nanocomposites synthesized by in situ polymerisation of a prepolymer diglycidyl ether of bisphenol-A crosslinked with an aliphatic diamine based on a polyoxypropylene backbone. The inorganic phase was hectorite, exchanged with octadecylammonium ions in order to give organophilic properties to the phyllosilicate. An ultrasonicator was used to disperse the silicate clay layer into epoxy-amine matrix. The morphology of epoxy-hectorite nanocomposites examined by transmission electron microscopy (TEM) showed that mixed delamination or intercalation or microdispersion could occur depending on type of organoclay. Moreover, the mechanical and viscoelastic properties were found to be improved with only the treated hectorite.

**Keywords:** nanocomposites, epoxy, hectorite, organoclay

## 1. Introduction

The utility of using nanosize layered silicate (organically modified clays) as reinforcements in organic polymers to obtain polymer/clay nanocomposites has been well reported over the past decade [1]. Good improvement in properties can be achieved in such materials due to the high surface contact area of the reinforcing filler which causes high strength, modulus and other properties at low clay loading level usually (<5 wt%). Our work is aimed to study epoxy-hectorite nanocomposites due to the wide applications of epoxy prepolymers as structural matrices and adhesives in electronic, electrical products and other items [1]. Therefore, epoxy prepolymers are some of the most commonly studied polymers in the preparation of nanocomposites with layered silicates because the polar epoxy monomers can easily diffuse into the

clay galleries [2, 3]. In fact, the matrix/filler type system used, the extent of filler adhesion to the matrix, and the levels of dispersion of the filler throughout the matrix degree are among the parameters which mainly determine any enhancement of a particular property of nanocomposites [4]. Moreover, the nature of the surfactant as well as the curing conditions, especially the temperature is expected to play a role in the exfoliation process [2]. In this respect, Kornman *et al.* [5] reported recently that a long chain alkylamine, having a chain of more than eight carbon atoms, could significantly result in an exfoliated clay structure. Furthermore, a balance between the intragallery and extragallery polymerization rates is essential to exfoliate the clay in an epoxy system [6]. According to the literature data [7–12], there are three different methods to synthesize polymer-clay nano-

\*Corresponding author, e-mail: [aboukerrou@yahoo.fr](mailto:aboukerrou@yahoo.fr)  
© BME-PT and GTE

composites: melt intercalation process for thermoplastic polymers, solution method, where both organoclay and polymer precursors are dissolved in a polar organic solvent and in situ polymerization technique. However, the latter one was found to be the most effective technique for thermoset polymer matrix nanocomposites [6].

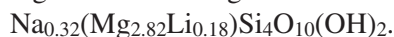
On the other hand, the commonly used techniques for processing clay-epoxy nanocomposites are direct mixing and solution mixing [13]. However, these techniques produce intercalated or intercalated/exfoliated composites rather than exfoliated composites. According to Vaia *et al.* [14], the degree of exfoliation can be improved through the aid of conventional shear devices such as extruders, mixers, ultrasonicators, etc.

In this paper, ultrasonication was used as a means of applying external shearing forces to disperse and exfoliate the silicate clay layers in the epoxy matrix. The procedure consisted firstly of swelling the clays in the curing agent due to its low viscosity allowing better diffusion into the intragallery space. The epoxy prepolymer was added, and under these conditions, the occurrence of a complete exfoliation was expected. It is worthwhile to point out that the nanosilicate used to carry out this study was a natural hectorite (called HECT) because literature data on its application in the epoxy-nanocomposites system are rather scarce.

## 2. Experimental

### 2.1. Materials used

The clay was a natural hectorite (called HECT) supplied by Süd-Chemie (from Germany) whose trade name is Optigel SH. It was a sodic silicate containing mainly magnesium and lithium according to the following chemical formula:



The cation exchange capacity (CEC) of the clay was 120 mequ/100 g.

The organic system was based on epoxy/amine, the prepolymer diglycidyl ether of bisphenol A (DGEBA) is manufactured by Vantico (France) under the grade name DGEBA LY 556 with the following characteristics: an  $n$  (polymerization degree) value of 0.15 and a number-average molecular weight of 382.6 g/mol. The curing agent is an aliphatic diamine with a polyoxypropylene backbone supplied by Huntsman (Belgium) under the

trade name Jeffamine D2000 with a number-average molecular weight of 1970 g/mol.

### 2.2. Organoclay preparation

The method of organoclay preparation is similar to that used by Le Pluart *et al.* [7]. The silicates were exchanged with octadecylammonium ions at 80°C with two CEC's (cation exchange capacity) amine/clay ratio. 0.2 moles of octadecylamine were dissolved in 20 l of 0.01 N of hydrochloric acid solution (based on deionised water). The solution was stirred at 80°C for three hours. Then, 100 g of clay were added to the solution and the whole was stirred at the same temperature for three more hours. The solution was filtered and the silicates were further washed 6 times more with hot deionised water and once with a hot ethanol: water (1:1) mixture so that no chloride was detected up on adding 0.1 m aqueous  $\text{AgNO}_3$ .

The resulting organoclay was then dried at 85°C for 36 hours and kept dry in a vacuum box. After modification, the organomodified silicates are called HECTC18.

### 2.3. Preparation of epoxy-nanocomposites

The silicate clays 5 per hundred resin (5 phr) and the curing agent were initially sonicated at 80°C for 10 min using an ultrasonic processor device at a frequency of 20 kHz, an amplitude of 6  $\mu\text{m}$  and electric power of 130 watts. The temperature of 80°C corresponded to the first curing temperature of the reactive agents. The epoxy prepolymer was then added to the mixture, and the whole was stirred for 15 min more. Then, the blend was poured into a steel mold and cured for 2 hours at 80°C, this was followed by postcuring for 3 hours at 120°C. The stoichiometric mass ratio of DGEBA to D2000 was calculated, and the value was 2.65 according to the the diamine functionality, which was itself determined by chloridric acid in dioxane (3.54) [15].

### 2.4. Nanocomposite characterization

#### 2.4.1. Wide angle X-ray diffraction

Wide angle X-ray diffraction (WAXD) measurements were performed at room temperature on a SIEMENS D500 diffractometer (Germany) with a Brentano Bragg geometry goniometer with  $\text{CuK}\alpha$

radiation (wavelength = 1.54 Å), operating at 40 kV and 30 mA. The diffraction patterns were collected between angles  $2\theta$  of 1 and 70° for unmodified HECT and 1–10° for modified HECT, at a scanning rate and step size of 5°/min and 0.02°, respectively.

#### 2.4.2. Transmission electronic microscopy

The different nanocomposites samples were ultramicrotomed with a diamond knife on a Leica (Bannock-burn IL) Ultracut UCT microtome at –70°C to give sections with a nominal thickness of 70 nm. The sections were transferred from dry conditions (–70°C) to carbon-coated 200-mesh Cu grids. The transmission electronic microscopy (TEM) images were obtained at 120 kV under low dose conditions, with a Philips CM120 electron microscope (Netherlands).

#### 2.4.3. Tensile testing

The stress – strain parameters were measured according to NF T 51-034 method, on a tensile machine 2/M which belongs to the MTS Society (France). The specimen has the shape H3 having the dimensions 2×4×10 mm, while the measurements were carried out at room temperature with a crosshead speed of 5 mm/min. An average value of 5 samples was determined.

The theory of rubber elasticity [16] was used to relate the state of deformation at the molecular level to the externally applied deformation. In the case of uniaxial deformation, the true stress (force divided by the deformed area) is defined, for dry networks formed in the bulk state as Equation (1):

$$\sigma = \rho \frac{RT}{M_c} \cdot (\lambda^2 - \lambda^{-1}) \quad (1)$$

where  $\sigma$  is the true stress,  $\rho$  is the network density,  $T$  is the absolute temperature,  $M_c$  is the average molecular weight of chains between crosslinks and  $\lambda$  is the extension ratio defined as the ratio of the final length of the sample in the direction of stretch to the initial length before deformation.

#### 2.4.4. Dynamic mechanical thermal analysis

The dynamic mechanical thermal analysis of the nanocomposite properties was determined with a Rheometric Dynamic Analyzer (Paris, France). The tests were carried out in the torsion deformation

mode, at a frequency of 1 Hz, with a temperature program ranging from –100 to 50°C at a heating rate of 3°C/min under a controlled strain of 0.17% corresponding to the linear portion of the viscoelastic domain of the material.

### 3. Results and discussion

#### 3.1. Organophilic modification of hectorite

The X-ray diffraction spectra gathered in Figure 1 already reveals that a first peak located on the spectrum characterizes the repetition of platelet in the direction (001), i. e. d-spacing and the other peaks allow to identify the silicate host structure. Although hectorite is a natural silicate, the diffraction peaks are less resolved. The shoulder at 12.03 Å reveals the lack of platelet organization on long distances.

After the cationic exchange, the silicate surface properties are modified. Taking into account the lack of crystalline organization for pristine hectorite, it is impossible to characterize the intercalation of organic chains between hectorite platelets by WAXS (Figure 2).

The thermal stability of clay before modification, analyzed by TGA from the weight loss derivative ( $dm/dT$ ) as a function of the temperature, is reported in Figure 3. Three areas of weight loss on DTG curves can be observed. The first volatile departure at temperatures lower than 150°C is associated with the vaporization of free water (between

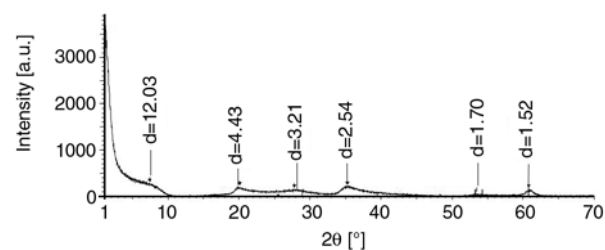


**Figure 1.** WAXD patterns of unmodified hectorite. The distance is given in Å

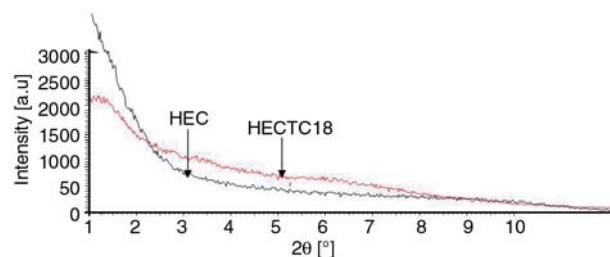


**Figure 2.** WAXD patterns of unmodified and modified hectorite. The distance is given in Å

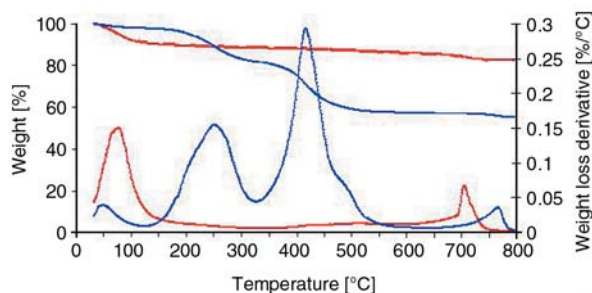


**Figure 3.** Weight loss and weight loss derivative of modified and unmodified hectorite

pores and aggregates). The second area is attributed to departure of intercalated water on a temperature range included between 350 and 670°C, and for higher temperatures between 650 and 750°C, the dehydroxylation of silicates is observed [17].

In Figure 3, the thermogravimetric analysis (TGA) of clay after modification, reveals several peaks linked to a volatile departure. The low-temperature peak, located between 40 and 70°C, is associated to the vaporization of free water and water bonded to the cations by hydrogen bonds. The following decompositions are related to alkylammonium ions. It was shown previously [17], that the first decomposition step is due to adsorbed octadecylammonium ions. In fact, after the cationic exchange, some ions remain adsorbed on hydroxyl groups on platelets edges and are not intercalated between the nanoplatelets. The thermal decomposition takes place in the range to 200–350°C range. The well intercalated modifying ions show higher thermal stability and the decomposition temperature included between 350–500°C depends on interactions between different organic groups and the platelet surface. At temperatures higher than 700°C, the dehydroxylation of the silicates takes place [18]. Thus the organophilic clays display organic chains both inside galleries as intercalated species and outside platelets as adsorbed species. This later category could be a wettability aid of nanofillers for being introduced into organic medium. The cationic exchange capacity was measured from the amount of intercalated ions determined after careful washing and the value is 120 meq/100 g indicating the high intercalated ions ratio inside galleries. These results indicate clearly that the organic modification of HECT occurs by ion exchange of the sodium ions present on HECT with organic alkyl ammonium ions leading to an intercalation.

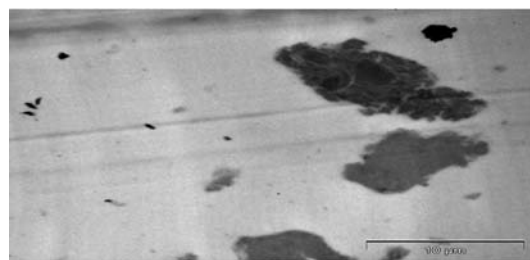


**Figure 4.** Transmission electronic microscopy (TEM) of DGEBA/D2000/HECT nanocomposites

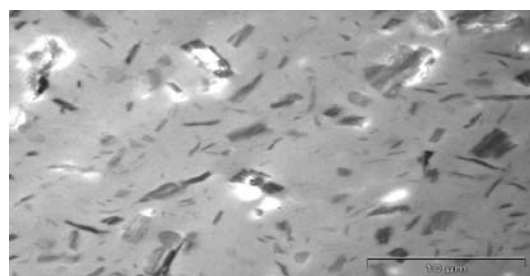


**Figure 5.** Transmission electronic microscopy (TEM) of DGEBA/D2000/HECTC18 nanocomposites

### 3.2. Morphology

Figures 4 and 5 show the transmission electron micrograph (TEM) images of HECT and HECTC18 nanocomposites, respectively. In Figure 5, it is observed the formation of agglomerates indicating clearly the poor dispersion of the clays in the epoxy matrix, because of the poor interactions between a polar unmodified HECT and the organic matrix. In contrast, Figure 5 illustrates a good dispersion of the clay particles and layers in the matrix resulting from the swelling of the HECTC18 in the nanocomposites, indicating a good compatibility between organophilic modified hectorite and the organic matrix [19].

### 3.3. Mechanical properties

Figure 6 shows the curves of the true stress as a function of  $(\lambda^2 - \lambda^{-1})$  for HECT and HECTC18 nanocomposites. The general form of the curves fits a linear relationship that is described by the following equation:  $\sigma = E(\lambda^2 - \lambda^{-1})$ , where  $E$  represents the slope of the curve defined as a rubber elasticity modulus [16]. In both samples, the stiffness is improved, however more pronounced in the case of HECTC18 nanocomposites. In fact, this property is increased by 16 and 55% for HECT and HECTC18 nanocomposites, respectively. This result is in agreement with that obtained by Wang *et al.* [20] who reported that the addition of 5 wt%

**Table 1.** Mechanical properties of the nanocomposites based on the DGEBA/D2000 matrix.  $E_0$ , elastic modulus of the neat matrix,  $\epsilon_r$ , elongation at break,  $W_0$ , energy at break of the neat matrix,  $W_b$ , energy at break of the nanocomposite,  $\sigma_r$ , stress at break. Those parameters were measured at 22°C.

Matrix DGEBA/D2000	E [MPa]	E/E <sub>0</sub>	$\sigma_r$ [MPa]	$\epsilon_r$ [%]	W <sub>b</sub> [10 <sup>-3</sup> J]	W <sub>b</sub> /W <sub>0</sub>
Unloaded	0.51	1	0.8 ± 0.05	69 ± 5	26 ± 2	1
HECT (5 phr)	0.59	1.16	0.58 ± 0.05	10 ± 3	50 ± 3	1.92
HECTC18 (5 phr)	0.79	1.55	1.03 ± 0.07	88 ± 3	118 ± 2	4.54

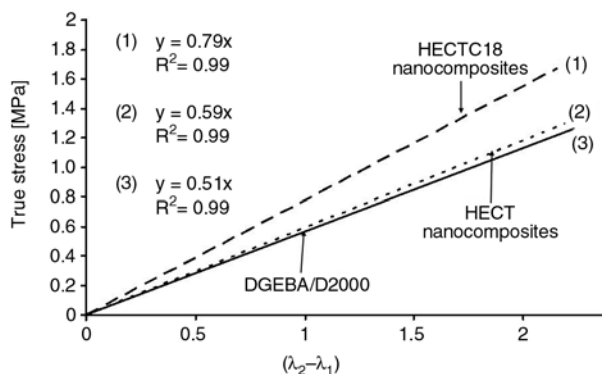


**Figure 6.** True stress as function of  $(\lambda^2 - \lambda^{-1})$  of DGEBA/D2000 matrix, HECT and HECTC18 nanocomposites

of nanoclay in epoxy amine matrix leads to an increase by twice of the rubber elasticity of the nanocomposites compared to that of the matrix. The  $E$  values are reported in details in Table 1. The stiffness, stress, strain and energy at break values of the epoxy matrix (DGEBA/D2000), HECT and HECTC18 nanocomposites are reported in details in Table 1. An increase of both the stress and the energy at break is observed in HECTC18 nanocomposite samples compared with the epoxy matrix. The increase of these two parameters could be attributed to better dispersion of organophilic nanosilicate in the nanocomposites compared to unmodified hectorite nanocomposites. These results are consistent with those obtained by TEM. When the dispersion of organoclays in the matrix DGEBA/D2000 is carried out manually, the mechanical properties do not increase significantly, compared with the results obtained with ultrasound mixing process. The improvement of mechanical properties might be linked to the state of dispersion at the micron and the nanometer scale level [7].

### 3.4. Dynamic thermal mechanical analysis

The dynamic mechanical properties of HECT and HECTC18 nanocomposites have been studied over a wide range (-100 to 50°C). The variation of  $\tan\delta$  as a function of temperature for both materials is

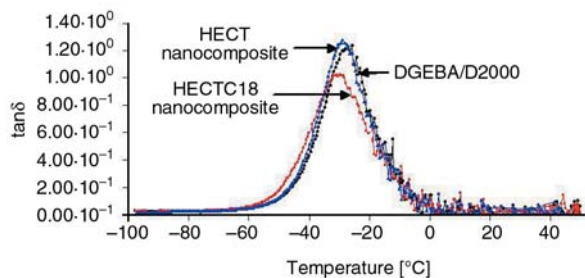


**Figure 7.**  $\tan\delta$  as a function of temperature for DGEBA/D2000 matrix, HECT and HECTC18 nanocomposites

reported in Figure 7. In this figure, it is observed one relaxation peak corresponding to the mechanical transition temperature which slightly decreases in the presence of the organosilicate. According to the literature [21], this behaviour is explained in terms of a reduction of the polymer volume fraction in the presence of the filler. This means that at low temperatures, the polymer matrix by itself is responsible for a high proportion of energy dissipation, while the nanoparticles strongly absorb any energy. Moreover, the  $\tan\delta$  peak seems to shift slightly to higher temperatures upon adding the nanoclay from -31 to -29°C. According to Lopez-Manchado [22], these results are due to the occurrence of a strong adhesion between the nanoclay and the matrix. This interaction reduces the mobil-

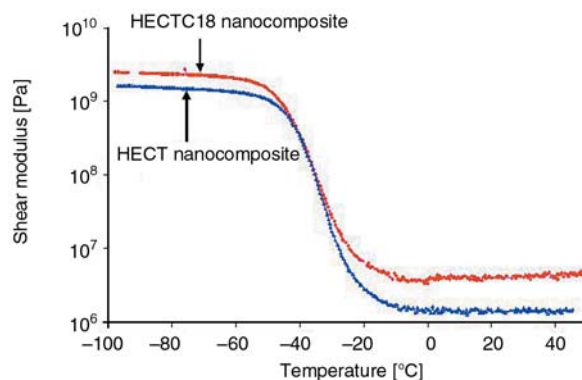


**Figure 8.** Storage modulus as a function of temperature for DGEBA/D2000 matrix, HECT and HECTC18 nanocomposites, measured at 1 Hz

**Table 2.** Values of the shear modulus ( $G'$ ), mechanical transition temperature ( $T_m$ ), and  $\tan\delta$  of various samples based on DGEBA/D2000 matrix, HECT and HECTC18 nanocomposites recorded at 1 Hz, measured between  $-100$  and  $50^\circ\text{C}$

Formulation codes	$G'$ at $25^\circ\text{C}$ [MPa]	$T_m$ [ $^\circ\text{C}$ ]	$\tan\delta$
DGEBA/D2000	1.23	$-31$	1.2
HECT/DGEBA/D2000	1.30	$-30$	1.1
HECTC18/DGEBA/D2000	4.26	$-29$	1.0

ity of the rubber epoxy chains, resulting in elevated transition temperature.

Figure 8 shows the shear modulus of HECT and HECTC18 nanocomposites as a function of temperature. It is noted that the organoclay induces a slight increase in modulus value of HECTC18 nanocomposites compared with the epoxy matrix which is attributed to the interaction of epoxy and HECTC18 [23]. All the data are reported in details in Table 2.

#### 4. Conclusions

From the study, the following conclusions can be drawn. Hectorite is a natural silicate, the diffraction peaks are less resolved. The shoulder at  $12.03 \text{ \AA}$  reveals the lack of platelet organization on long distances.

The modification of the surface of HECT by octadecylammonium ions to HECTC18 produces an intercalation as demonstrated by the TG/DTG thermograms. The addition of HECTC18 to the epoxy matrix in the proportion of 5 phr and the application of a sonicator as a device to ensure a good stirring leads to an exfoliation. As a result, a significant improvement of both the stress – strain parameters at break and the viscoelastic properties is observed. Finally, the HECTC18 increases considerably both the stiffness and the energy at break of the nanocomposites, although it is not easy to obtain a compromise between the two parameters. However, in the case of the nanocomposites studied, i. e. DGEBA/D2000/HECTC18, the homogeneity of the morphology results in a significant increase of both the stiffness by almost 55% and the energy at break by more than 350%.

#### References

- [1] Boukerrou A., Duchet J., Fellahi S., Sautereau H.: Effect of geometry and surface properties of silicates on nanostructuring of suspension in precursors of an epoxy/amine network. *Journal of Applied Polymer Science*, **102**, 1380–1390 (2006).
- [2] Kornmann X., Lindberg H., Berglund L. A.: Synthesis of epoxy-clay nanocomposites. Influence of the nature of the curing agent on structure. *Polymer*, **42**, 4493–4499 (2001).
- [3] Chin I-J., Thurn-Albrecht T., Kim H-C., Russel T. P., Wang J.: On exfoliation of montmorillonite in epoxy. *Polymer*, **42**, 5947–5952 (2001).
- [4] Evora V. M. F., Shukla A.: Fabrication, characterization and dynamic behavior of polyester/TiO<sub>2</sub> nanocomposites. *Material Science and Engineering: A*, **363**, 358–366 (2003).
- [5] Kornmann X., Lindberg H., Berglund L. A.: Synthesis of epoxy-clay nanocomposites: Influence of the nature of the clay on the structure. *Polymer*, **42**, 1303–1310 (2001).
- [6] Nigam V., Setua D. K., Matur G. N., Kar K. K.: Epoxy-montmorillonite clay nanocomposites: Synthesis and characterization. *Journal of Applied Polymer Science*, **93**, 2201–2210 (2004).
- [7] Le Pluart L., Duchet J., Sautereau H.: Epoxy/montmorillonite nanocomposites: Influence of organophilic treatment on reactivity, morphology and fracture properties. *Polymer*, **46**, 12267–12278 (2005).
- [8] Chow W. S.: Water absorption of epoxy/glass fiber/ organo-montmorillonite nanocomposites. *Express Polymer Letters*, **1**, 104–108 (2007).
- [9] Pegoretti A., Dorigato A., Penati A.: Tensile mechanical response of polyethylene-clay nanocomposites. *Express Polymer Letters*, **1**, 123–131 (2007).
- [10] Da Z. L., Zhang Q. Q., Wu D. M., Yang D. Y., Qiu F. X.: Synthesis, characterization and thermal properties of inorganic-organic hybrid. *Express Polymer Letters*, **1**, 698–703 (2007).
- [11] Zammarano M., Bellayer S., Gilman J. W., Franceschi M., Beyer F. L., Harris R. H., Meriani S.: Delamination of organo-modified layered double hydroxides in polyamide 6 by melt processing. *Polymer*, **47**, 652–662 (2006).
- [12] Cai L. F., Mai Y. L., Rong M. Z., Ruan W. H., Zhang M. Q.: Interfacial effects in nano-silica/polypropylene composites fabricated by in-situ chemical blowing. *Express Polymer Letters*, **1**, 2–7 (2007).
- [13] Asma Y., Jandro L. A., Issac M. D.: Processing of clay-epoxy nanocomposites by shear mixing. *Scripta Materialia*, **40**, 81–86 (2003).
- [14] Vaia R. A., Ishii H., Giannelis E. P.: Synthesis and properties of two dimensional monostructures by direct intercalation of polymer melts in layered silicates. *Chemical Materials*, **5**, 1694–1696 (1993).
- [15] Lan T., Pinavaia T. J.: Clay-reinforced epoxy nanocomposites. *Chemical Materials*, **6**, 2216–2219 (1994).

- [16] Bokobza L.: Reinforcement of elastomeric network by fillers. *Macromolecule Symposia*, **171**, 163–170 (2001).
- [17] Xie W., Gao Z., Pan W-P., Hunter G., Singh A., Vaia R.: Thermal degradation chemistry of alkyl quaternary ammonium montmorillonite. *Chemical Materials*, **13**, 2979–2990 (2001).
- [18] Le Pluart L., Duchet J., Sautereau H., Gérard J. F.: Surface modification of montmorillonite for tailored interfaces in nanocomposites. *Journal of Adhesion*, **78**, 645–662 (2002).
- [19] Boukerrou A., Duchet J., Fellahi S., Sautereau H.: Processing of mica/epoxy nanocomposites by ultrasound mixing. *Journal of Applied Polymer Science*, **105**, 1420–1425 (2007).
- [20] Wang Z., Pinnavaia T. J.: Hybrid organic-inorganic nanocomposites/exfoliation of magadiite nanolayers in an elastomeric epoxy polymer. *Chemical Materials*, **10**, 1820–1826 (1998).
- [21] Wang M. S., Pinnavaia T. J.: Clay-polymer nanocomposites formed from acidic derivatives of montmorillonite and an epoxy resin. *Chemical Materials*, **6**, 468–474 (1994).
- [22] Lopez-Manchado M. A., Herrero B., Arroyo M.: Organoclay-natural rubber nanocomposites synthesized by mechanical and solution mixing methods. *Polymer International*, **53**, 1766–1772 (2004).
- [23] Chow W. S., Mohd Ishak Z. A.: Mechanical, morphological and rheological properties of polyamide 6/ organo-montmorillonite nanocomposites. *Express Polymer Letters*, **1**, 77–83 (2007).

# Fiber reinforced silicon-containing arylacetylene resin composites

J. Zhang, J. Huang, W. Zhou, F. Huang\*, L. Du

School of Material Science and Engineering, Key Laboratory for Ultrafine Materials of Ministry of Education, East China University of Science and Technology, 130 Meilong Road, Shanghai 200237, P. R. China

Received 27 July 2007; accepted in revised form 8 November 2007

**Abstract.** A silicon-containing arylacetylene resin (SAR), a poly(dimethylsilyleneethynylene phenyleneethynylene) (PMSEPE), was synthesized. The PMSEPE is a solid resin at ambient temperature with a softening temperature about 60°C and soluble in some solvents like tetrahydrofuran. The melt viscosity of the PMSEPE resin is less than 1 Pa·s. The resin could cure at the temperature of lower than 200°C. Fiber reinforced PMSEPE composites were prepared from prepregs which were made by the impregnation of fibers in PMSEPE resin solution. The composites exhibit good mechanical properties at room temperature and 250°C. The observation on fracture surfaces of the composites reinforced by glass fibers and carbon fibers demonstrates that the adhesion between the fibers and resin is good. The results from an oxyacetylene flame test show that the composites have good ablation performance and XRD analyses indicate that SiC forms in the residues during the ablation of the composites.

**Keywords:** thermosetting resins, silicon-containing arylacetylene resin, high performance composites, advanced polymer composite, heat and ablation resistance

## 1. Introduction

In recent years, many studies have focused on silicon-containing polymers because of the highly potential applications of the polymers as coatings, adhesives, ceramic precursors, composite matrices, and even conducting materials to aerospace and astronautics, electronics, high-technologies, construction, and so on due to special properties and high thermal stability [1–5]. The silicon-containing polymers with ethynyl or ethynylene groups are interesting and important polymers. Some silicon-containing polymers with  $[-SiR_2-C\equiv C-]$  and  $[-SiR_2-C\equiv C-Ar-C\equiv C-]$  units (R = alkyl or phenyl) have been explored and developed. Itoh, *et al.* [6–9] firstly prepared poly(phenylsilyleneethynylene-1,3-phenyleneethynylene) (abbreviated as MSP) by a dehydrogenative coupling polymerization reaction between phenylsilane and *m*-diethynyl-

benzene in the presence of a magnesia base catalyst. The decomposition temperature of cured MSP resin at 5% weight loss is 860°C and the decomposition residue at 1000°C is 94%. Buvat, *et al.* [10, 11] synthesized poly(silyleneethynylene-phenyleneethynylene) terminated with phenylacetylene (abbreviated as BLJ) by polycondensation reaction of dichlorosilane, diethynylbenzene, and phenyl acetylene. The BLJ resin possesses good processability and high heat resistance ( $T_g > 450^\circ\text{C}$  residue  $> 80\%$  at 1000°C).

Recently, our laboratory has been making an effort to develop a kind of silicon-containing arylacetylene resin (SARs). The investigation on poly(dimethylsilyleneethynylene-phenyleneethynylene)s terminated with phenylacetylene was reported, which could cure at the temperature about 230°C and shows good processability and high heat

\*Corresponding author, e-mail: [fhuanglab@ecust.edu.cn](mailto:fhuanglab@ecust.edu.cn)  
© BME-PT and GTE

resistance [12, 13]. In this paper, a poly(dimethylsilyleneethynylenephenyleneethynylene) (PMSEPE) resin and fiber reinforced PMSEPE composites were prepared and characterized.

## 2. Experimental

### 2.1. Raw materials

Dimethyldichlorosilane and ethyl bromide (Shanghai No.1 Reagent Factory) were freshly distilled before used. Diethynylbenzene was synthesized and supplied by the Laboratory of Fine Chemicals in East China University of Science and Technology. Magnesium ribbons (Shanghai No.1 Reagents Company) were treated before used. Tetrahydrofuran (THF) and toluene (Shanghai No.1 Reagent Company) were dried over sodium and distilled before used. A plain T300 carbon fabric (T300/3K-200P, Toray), a plain glass fabric (SW160-90, Nanjing Glass Fibers Company), T700 unidirectional carbon fibers (Toray), rayon-based carbon fibers (NCF-2, Liaoyuan Chemical Materials Company), and high SiO<sub>2</sub> glass fibers (Huatae Glass Fiber Company) were used as reinforcements.

### 2.2. Analyses and tests

The molten resin was coated on the a KBr wafer. The Fourier Transform Infrared (FT-IR) spectrum for the resin was recorded with 32 scans on Nicolet Magna 550. <sup>1</sup>H-NMR and <sup>29</sup>Si-NMR analyses were carried out on a Bruker AVANCE 500 (500 MHz) spectrometer. Rheological behavior of a resin was traced on a RheoStress RS600 Rheometer at 2°C/min and a shear rate of 0.1 s<sup>-1</sup>. The flexural property of a composite laminate sample was measured with a Shimadzu AG-50kNE universal tester and MTS Alliance RF/100 tester (USA) according to China Standard GB 3356. The crosshead speed for the tests is 2 mm/min. The sample dimension was 80.0×12.5×2.0 mm<sup>3</sup>. The flexural properties for composites at 250, 300, 400 and 500°C are measured separately in a in-situ temperature-controlled chamber attached to the testers. For the high temperature tests, the samples were kept at the measuring temperature like 400°C for 10 minutes before the measure started. XRD analyses were conducted on a Rigaku D/Max 250 VB/PC diffractometer. Scanning electron microscopy (SEM) images were obtained with a JEOL JSM-6360LV

microscope. An oxyacetylene flame test for ablation property was performed according to China Standard GJB323A-96 standard on an oxyacetylene ablation apparatus. The pressure and flux of acetylene gas were 0.095 MPa and 1.11 m<sup>3</sup>/h and those of oxygen gas 0.40 MPa and 1.50 m<sup>3</sup>/h for the test, respectively. The temperature of the oxyacetylene flame was measured using an optical pyrometer and reached as high as 2800°C. The distance between the flame outlet and the sample was 10 mm. The ablation time was 20 second. The sample for the ablation test was a disk with diameter of φ30 mm and thickness of 10 mm.

### 2.3. Synthesis of

#### poly(dimethylsilyleneethynylenephenylene ethynylene) (PMSEPE) resin

The PMSEPE resin was synthesized by reference to the preparation procedure described in a published article [12]. The treated magnesium ribbons were cut into small pieces. Then 6.00 g magnesium pieces and 50 ml THF were charged into a three-necked round bottom flask equipped with a condenser, a dropping funnel, a bypass of inert gas and a stirrer. To the flask, 21.6 g ethyl bromide in 50 ml THF was added dropwise under agitation to produce ethylmagnesium bromide. To the reaction flask, a solution of 11.35 g diethynylbenzene in 50 ml THF was added dropwise at room temperature for 1 h and the reaction was continued for an additional 2 hours at the refluxing condition. A solution of 9.29 g dimethyldichlorosilane in 50 ml THF was dropwise added to the above flask at room temperature over a period of 1 h with stirring. The reaction was developed for another 2 hours with refluxing. All reactions were carried out under dry nitrogen. After treated by neutralization, abstraction, separation, wash, and distillation, an orange crude resin product was obtained. The yield was 88%. The structure of the synthetic resin is shown in Figure 1. The FT-IR spectrum for the resin is shown in Figure 2. The absorption at 3300 cm<sup>-1</sup> is attributed to the vibration of the group ≡C-H. The characteristic peak at 2156 cm<sup>-1</sup> belongs to the stretching vibration of C≡C bond. There is a characteristic absorption peak at 1253 cm<sup>-1</sup> for the stretching vibration of Si-CH<sub>3</sub> bond. Other analysis results as follows. <sup>1</sup>H-NMR (CDCl<sub>3</sub>, TMS): 3.05(s, ≡CH), 0.37(s, Si-CH<sub>3</sub>),

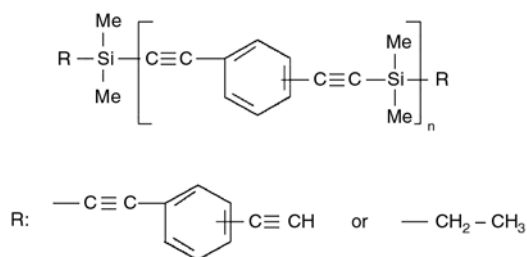


**Figure 1.** The chemical structure for the PMSEPE resin

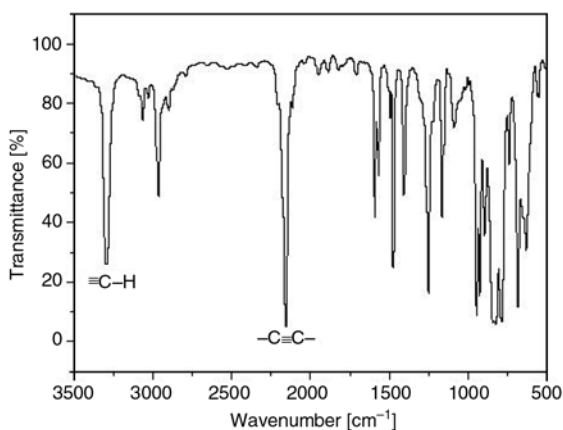


**Figure 2.** The FT-IR spectrum for the PMSEPE resin

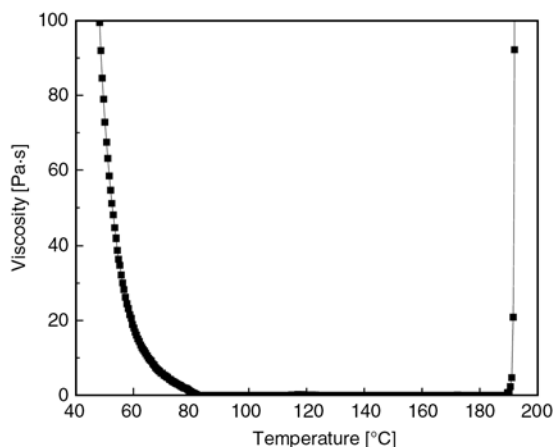


**Figure 3.** Viscosity-temperature curve of the PMSEPE resin

7.2–7.7(m, Ar-H).  $^{29}\text{Si}$ -NMR ( $\text{CDCl}_3$ , TMS):  $-39.0$ (s,  $\text{C} \equiv \text{C}-\text{Si}$ ).

The viscosity response of PMSEPE resin to the temperature ramping at a heating rate of  $2^\circ\text{C}/\text{min}$  by the rheometer analysis is shown in Figure 3. The viscosity of the resin in the temperature range of 80 to  $190^\circ\text{C}$  is less than  $1 \text{ Pa}\cdot\text{s}$ , which would be suitable for the RTM process. Resin viscosity increases rapidly at temperature above  $190^\circ\text{C}$  due to the further polymerization of the resin. Thereafter, the gelation of the resin occurs.

## 2.4. Preparation of composites

The fabrics (glass: 2D fabric, plain, low alkali E-glass; carbon: 2D fabric, plain, T300) were impregnated with PMSEPE resin solution (37 wt% resin in THF) and dried in air. An unidirectional prepreg was prepared from unidirectional carbon fibers (T700) and the PMSEPE resin solution by using a drum winding technique. The prepreg was dried on the mandrel to evaporate the solvent and then removed from the drum. The prepreps with good tack and drape were obtained. The content of PMSEPE resin for these prepreps was 35 wt% (ca). The prepreps were then directionally piled up and further dried in a vacuum oven to remove the solvent further if necessary. The piled prepreps were put into a mold and pressed at  $170^\circ\text{C}$  for 2 h,  $210^\circ\text{C}$  2 h, and  $250^\circ\text{C}$  4 h in order under the pressure of 2 MPa, successively. For unidirectional composites, an additional treatment process, i. e.,  $300^\circ\text{C}$  2 h under the pressure of 2 MPa, was applied. Finally, laminated composite boards with thickness of 2.0 mm (ca) were obtained and the content of cured PMSEPE resin in the composites was 33 wt% (ca). The composite samples for the oxyacetylene flame tests were made from bulk molding compounds (BMC) of PMSEPE resin and short fibers. The short carbon fibers (rayon-based carbon fiber) and short glass fibers (high  $\text{SiO}_2$  content) with the length of 20–30 mm were used. The content of the resin in the composite sample was 40 wt% (ca). The BMC was pressed in a mold at  $170^\circ\text{C}$  for 2 h,  $210^\circ\text{C}$  2 h, and  $250^\circ\text{C}$  4 h in order under the pressure of 5–6 MPa. The composite composed of glass fibers and PMSEPE resin is denoted as GF-PMSEPE and the composite composed of carbon fibers and PMSEPE resin as CF-PMSEPE. The attached number indicate the dimension of fiber distribution in composites: 1 stands for unidirectional fibers, 2 for plain woven fabrics, 3 for disorder short fibers.

## 3. Results and discussion

### 3.1. Mechanical properties of composites

The flexural strength and modulus of fiber reinforced PMSEPE composites at different conditions are shown in Table 1. The flexural strength of GF-PMSEPE-2 composite (248 MPa) at ambient temperature is lower than that of CF-PMSEPE-2 composite (275 MPa), which could result from high

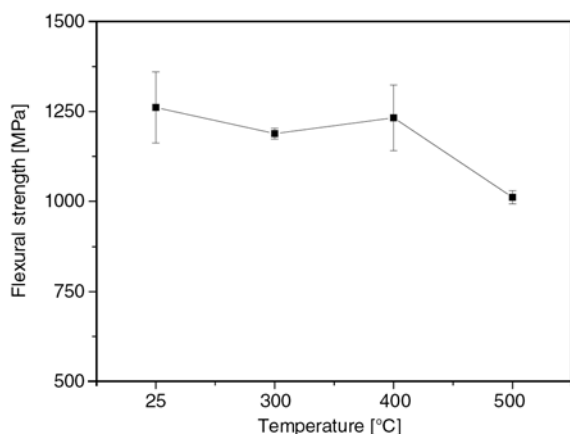
**Table 1.** Flexural properties of composites

Specimen	Reinforcements	Flexural strength [MPa]		Flexural modulus [GPa]	
		RT	250°C	RT	250°C
GF-PMSEPE-2	glass fabric(2D)	248	268	23.9	20.6
CF-PMSEPE-2	T300 carbon fabric(2D)	275	315	59.8	70.4
CF-PMSEPE-1	T700 unidirectional carbon fibers	1495	1202	118.1	105.6

strength of the carbon fiber and good wetting of the resin to carbon fibers. The flexural strength of GF-PMSEPE-2 and CF-PMSEPE-2 composites at 250°C is a bit higher than that at room temperature probably due to the further curing of the resin at higher temperature, which correspond to the research results of Itoh's group [14]. The modulus for CF-PMSEPE-2 composite increases while GF-PMSEPE-2 composite decreases with the temperature rising. This is probably caused by the limit of heat resistance and the decrease of the property for the glass fiber at 250°C (the softening point is ~550°C). Nevertheless, the flexural properties of the CF-PMSEPE-1 composite decreased with the temperature as usual. Further investigation on the reinforcing behaviour of the composites will be

undertaken. Whether or not, those results indicate PMSEPE composites have high heat resistance.

The flexural properties for CF-PMSEPE-1 composite at 300, 400 and 500°C are measured separately in a temperature-controlled chamber attached to a testing machine. Temperature dependence of flexural strength of CF-PMSEPE-1 composite is shown in Figure 4. The strength of the composites changes a little in the range of 25 to 400°C. Although the flexural strength decreases as the temperature increases further, the values of the strength for CF-PMSEPE-1 composite at 400 and 500°C arrive at as high as 1260 and 985 MPa, respectively. This indicates that the composite has excellent mechanical properties at 400–500°C and could be expected for the applications at 400°C.

**Figure 4.** Temperature dependence of flexural strength of the CF-PMSEPE-1 composite

### 3.2. The fracture morphology of composites

Figure 5 shows the micrographs of the fracture surface of the composites reinforced by glass fabric (GF-PMSEPE-2) and carbon fabric (CF-PMSEPE-2). As shown in Figure 5, the surfaces of the fibers and the fracture surfaces of PMSEPE resin on the fracture area of the composites are obviously observed. However, visible separation of the interfaces between the fibers and the resin does not occur. This indicates that the interface adhesion between the fibers and the resin is good, which illustrates that the composites possess high mechanical strength. In addition, more non-wetted fibers in

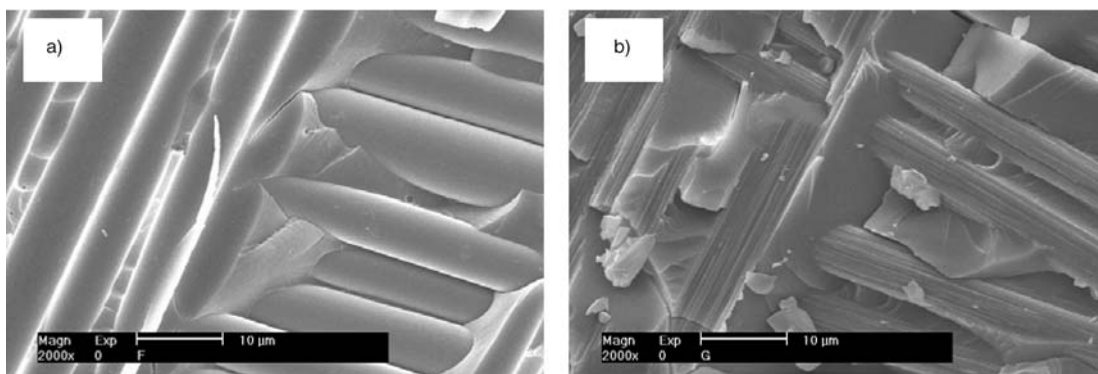
**Figure 5.** The micrographs of the fracture surface of the composites: a) GF-PMSEPE-2 composite; b) CF-PMSEPE-2 composite

Figure 5a are observed. This means that the PMSEPE resin wets carbon fibers easier than glass fibers, i. e., the adhesion of the resin to glass fibers is weaker than that to carbon fibers. This also indicates that the PMSEPE resin has more tendency to wet nonpolar fibers like carbon fibers.

### 3.3. Ablative properties of composites

The oxyacetylene flame test was used to evaluate the ablation performance of the composites. Table 2 lists the oxyacetylene flame (ablation) test results for the composites with different reinforcements. As shown in Table 2, the erosion rate of the composites is low, which indicates the PMSEPE resin composites possess good ablation performance. As compared with CF-PMSEPE-3 composite, GF-PMSEPE-3 composite has the higher erosion

rates. This probably results from the melting of the glass fibers during the test.

X-ray diffraction analysis results for ablated composites are shown in Figure 6. As shown in Figure 6, there are three sharp peaks (at  $2\theta = 35.58$ ,  $60.02$  and  $71.78^\circ$ ) attributed to SiC crystals. The peaks for the ablated CF-PMSEPE-3 composite are more intense than that for the ablated GF-PMSEPE-3 composite. This indicates that inorganic SiC ceramic formed after the composites were ablated in the oxyacetylene flame test and the CF-PMSEPE-3 composite was easier to produce SiC than GF-PMSEPE-3 composite during the ablation. Formation of SiC with excellent thermal stability would increase the ablation resistance of the composites. In addition, there are broad peaks at  $25$ ,  $35$  and  $43^\circ$  which are related to amorphous  $\text{SiO}_2$  and carbon in Figure 6. Therefore, amorphous  $\text{SiO}_2$  and carbon are also present in the ablated products.

**Table 2.** Ablative properties of composites

Specimen <sup>a</sup>	Reinforcement	Density [g/cm <sup>3</sup> ]	Line erosion rate [mm/s]	Mass erosion rate [mg/s]
GF-PMSEPE-3	Glass fibers	1.49	0.122	31.4
CF-PMSEPE-3	Carbon fibers	1.26	0.040	15.3

<sup>a</sup>The composites made from the dough molding compound of the resin and short fibers

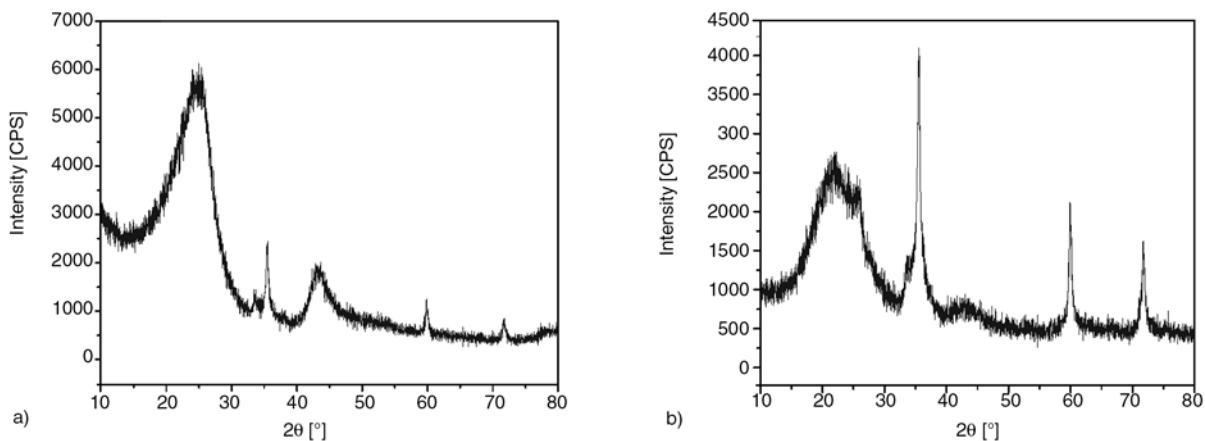


**Figure 6.** XRD spectrogram of the ablated composites: a) GF-PMSEPE-3; b) CF-PMSEPE-3

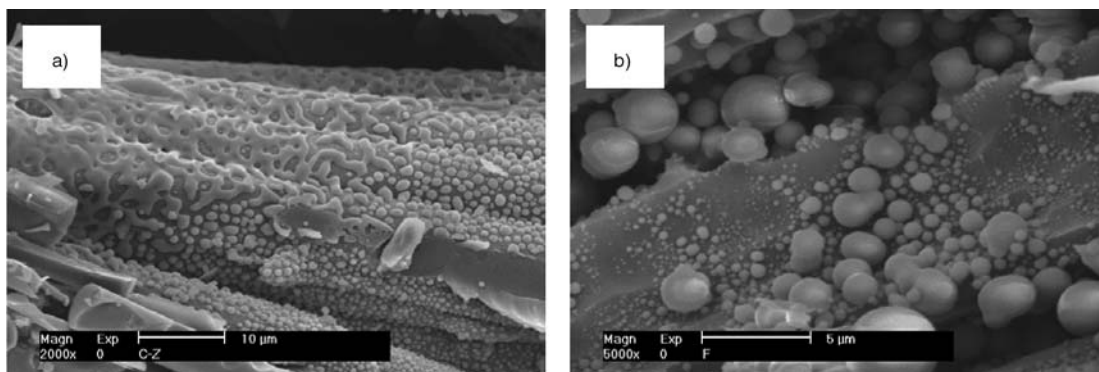


**Figure 7.** SEM of the ablated composites: a) GF-PMSEPE-3; b) CF-PMSEPE-3

The morphology of the ablated composites was observed by scanning electron microscopy (SEM). The micrographs are shown in Figure 7. As shown in Figure 7a, there are some particles and network substances like aggregated melt liquid drops on the surface of glass fibers after the ablation of GF-PMSEPE-3 composite, which possibly results from partially melted glass fibers. Figure 7b shows that there are particles with different sizes on the surface of carbon fibers or among the carbon fibers and that some carbon fibers have been ablated. Therefore, the destruction of composites occurs due to the decomposition of PMSEPE resin and the melting or burning of the fibers. The particles produced would be SiC, SiO<sub>2</sub>, etc. Further analyses and determination of the particles are under the way.

#### 4. Conclusions

Poly(dimethylsilyleneethynylphenyleneethynylene) (PMSEPE) resin was synthesized and the resin composites reinforced by different fibers were prepared. The fibers reinforced PMSEPE composites show good mechanical properties at room temperature and 250–400°C and good ablation performance. The resin could be expected to be used as an important high performance matrix for advanced composite materials.

#### Acknowledgements

The authors gratefully thank the National Basic Research Program of China (Grant No. 51318020006) and the National High Technology Research and Development Program of China (Grant No. 2002AA305205) for the financial supports.

#### References

- [1] Ichitani M., Nakamura K.: Cured product of carborene-containing silicon-base resin. Japanese patent, JP 2000309635, Japan (2000).
- [2] Ito M., Inoue K., Hirayama N., Sugimoto M., Seguchi T.: Fiber reinforced composites with a new heat-resistant polymer matrix containing silicon. *Journal of the Japan Society for Composite Materials (in Japanese)*, **27**, 188–193 (2001).
- [3] Buvat P., Jousse F., Gerard J-F., Nony F.: Compositions with poly(ethynylene phenylene ethynylene silylenes). French Patent, FR 2836922, France (2003).
- [4] Narisawa M., Tanaka E., Nishimura R., Okamura K., Itoh M., Kamiyama T.: Synthesis and characterization of carbon-based hybrid ceramics in coating form from thermosetting resin-alkoxide mixtures. *Key Engineering Materials: Advanced Ceramics and Composites*, **247**, 137–140 (2003).
- [5] Inoue K., Iwata K., Ishikawa J., Fujikake S., Itoh M.: Silicon-containing polymers for manufacture of ceramic moldings. Japanese patent, JP 19970428, Japan (2003).
- [6] Itoh M., Inoue K., Iwata K., Mitsuzuka M., Kakigano T.: New highly heat-resistant polymers containing silicon: Poly(silyleneethynylphenyleneethynylene)s. *Macromolecules*, **30**, 694–701 (1997).
- [7] Itoh M., Mitsuzuka M., Iwata K., Inoue K.: Silicon-containing carbon materials. Japanese patent, JP 19941124, Japan (1994).
- [8] Itoh M., Mitsuzuka M., Iwata K., Inoue K.: Silicon-containing fire-resistant materials. Japanese patent, JP 19940712, Japan (1994).
- [9] Itoh M., Inoue K., Iwata K., Mitsuzuka M., Nara R., Hirayama N.: Highly heat-resistant polymers containing silicon: poly(silyleneethynylphenyleneethynylene)s. *Journal of Network Polymer (in Japanese)*, **17**, 161–168 (1996).
- [10] Buvat P., Jousse F., Delnaud L., Levassort C.: Synthesis and properties of new processable type polyarylacetylenes. in 'International SAMPE Symposium and Exhibition 2001, Long Beach, USA' 134–144 (2001).
- [11] Buvat P., Levassort C., Jousse F.: Poly(silyleneethynylphenyleneethynylene) and methods for preparing same. French Patent, FR 2798662, France (2001).
- [12] Wang F., Zhang J., Huang J., Yan H., Huang F., Du L.: Synthesis and characterization of poly(dimethylsilyleneethynylphenyleneethynylene) terminated with phenylacetylene. *Polymer Bulletin*, **56**, 19–26 (2006).
- [13] Zhang J., Zhou W., Huang J. X., Wang F., Gao F., Huang F. R., Du L.: The property investigation of a novel silicon-containing arylacetylene resin and its composite. in 'Proceeding of 14<sup>th</sup> National Conference on Composite Materials of China, Wuhan, China' (in Chinese) 472–476 (2006).
- [14] Itoh M., Inoue K., Hirayama N., Sugimoto M., Seguchi T.: Fiber reinforced plastics using a new heat-resistant silicon based polymer. *Journal of Materials Science*, **37**, 3795–3801 (2002).

# Relaxation phenomena in rubber/layered silicate nanocomposites

G. C. Psarras<sup>1\*</sup>, K. G. Gatos<sup>2</sup>, P. K. Karahaliou<sup>1,3</sup>, S. N. Georga<sup>3</sup>, C. A. Krontiras<sup>3</sup>,  
J. Karger-Kocsis<sup>2</sup>

<sup>1</sup>Department of Materials Science, School of Natural Sciences, University of Patras, Patras 26504, Greece

<sup>2</sup>Institute for Composite Materials, Kaiserslautern University of Technology, Erwin Schrödinger Str., Kaiserslautern, D-67663, Germany

<sup>3</sup>Department of Physics, School of Natural Sciences, University of Patras, Patras 26504, Greece

Received 27 July 2007; accepted in revised form 10 November 2007

**Abstract.** Broadband Dielectric Spectroscopy (BDS) is employed in order to investigate relaxation phenomena occurring in natural rubber (NR), polyurethane rubber (PUR) and PUR/NR blend based nanocomposites, reinforced by 10 parts per hundred (phr) Layered Silicates (LS). Nanocomposites and matrices were examined under identical conditions in a wide frequency ( $10^{-1}$  to  $10^6$  Hz) and temperature ( $-100$  to  $50^\circ\text{C}$ ) range. Experimental data are analyzed in terms of electric modulus formalism. The recorded relaxation phenomena include contributions from both the polymer matrices and the nanofiller. Natural rubber is a non-polar material and its performance is only slightly affected by the presence of layered silicates. Polyurethane rubber exhibits four distinct relaxation processes attributed, with ascending relaxation rate, to Interfacial Polarization (IP), glass/rubber transition ( $\alpha$ -mode), local motions of polar side groups and small segments of the polymer chain ( $\beta$ ,  $\gamma$ -mode). The same processes have been detected in all systems containing PUR. IP is present in all nanocomposites being the slowest recorded process. Finally, pronounced interfacial relaxation phenomena, occurring in the PUR+10 phr LS spectra, are attributed to nanoscale effects of intercalation and exfoliation.

**Keywords:** polymer composites, nanocomposites, dielectric spectroscopy, relaxations, rubber

## 1. Introduction

The impact of nanomaterials and/or nanostructured materials is well known and well appreciated [1–4], mostly due to their potential applications based on their thermo-mechanical performance, flame resistance, electrical properties etc. Polymer matrix nanocomposites can be prepared by dispersing a small amount of nanometer size filler within the host medium. Rubber/Layered Silicate (LS) nanocomposites are increasingly attracting scientific and technological attention, because of the high reinforcing efficiency of the LS, even at very low loading. Polymer matrix/LS nanocomposites exhibit three different configurations: (a) microphase sepa-

rated composites, where polymer matrix and layered silicates remain immiscible, (b) intercalated structures, where polymer molecules are inserted between the silicate layers, and (c) exfoliated structures, where individual silicate layers are dispersed in the polymer matrix.

Polymer matrix nanocomposites are expected to be useful in replacing conventional insulating materials providing tailored performance, by simply controlling the type and the concentration of nanoinclusions [5–8]. ‘Nanodielectrics’ is a rather new term associating dielectrics with nanotechnology [9]. Nanoinclusions could be able to serve as inherent nanocapacitors. Charging and discharging

\*Corresponding author, e-mail: [G.C.Psarras@upatras.gr](mailto:G.C.Psarras@upatras.gr)  
© BME-PT and GTE

under control the embedded in a matrix nanocapacitors, defines an energy storing procedure at the nanoscale level introducing a new type of nanodevices.

Broadband Dielectric Spectroscopy (BDS) is a powerful tool for the investigation of molecular mobility, phase transitions, conductivity mechanisms and interfacial effects in polymers and complex systems [10]. In the present study, natural rubber, polyurethane rubber and natural/polyurethane blend based nanocomposites were prepared by adding a pristine synthetic layered silicate (sodium fluorohectorite) in 10 parts per hundred parts rubber, following the latex compounding route. The dielectric properties, of the produced nanocomposites, were examined by means of BDS at temperatures varying from –100 to 50°C.

## 2. Experimental

A synthetic sodium fluorohectorite (Somasif ME-100) of Co-op Chemicals (Tokyo, Japan) was used as LS. This LS has an intergallery distance of 0.95 nm and exhibits a very high aspect ratio, viz. >1000. Sulfur prevulcanized NR latex was procured from the Rubber Research Institute of India (Kottayam, Kerala, India). PUR latex (Impranil DLP-R) containing ca. 50% polyester-based polyurethane was supplied by Bayer AG (Leverkusen, Germany). The produced nanocomposites were all containing the same amount of nanofiller (10 phr of LS). Further information concerning the preparation route of the nanocomposites, morphology detection and thermal characterization can be found elsewhere [11, 12].

Broadband dielectric measurements were performed, in the frequency range of 10<sup>-1</sup> to 10<sup>6</sup> Hz, by means of an Alpha-N Frequency Response

Analyser, supplied by Novocontrol Technologies GmbH (Hundsangen, Germany). The BDS-1200, parallel-plate capacitor with two gold-plated electrodes supplied also by Novocontrol Technologies, was used as test cell. The dielectric cell was electrically shielded in nitrogen gas atmosphere and isothermal frequency scans were conducted for each of the examined specimens. Temperature was controlled by the Quattro system within ±0.1°C and varied between –100 and 50°C in steps of 5°C. The examined systems were: NR, PUR, PUR/NR, NR+10 phr LS, PUR+10 phr LS, PUR/NR+10 phr LS.

## 3. Results and discussion

Dielectric data can be analysed by means of different formalisms such as permittivity mode, modulus mode and ac conductivity mode. Electric modulus is defined as the inverse quantity of complex permittivity by the Equation (1):

$$M^* = \frac{1}{\epsilon^*} = \frac{1}{\epsilon' - j\epsilon''} = \frac{\epsilon'}{\epsilon'^2 + \epsilon''^2} + j \frac{\epsilon''}{\epsilon'^2 + \epsilon''^2} = M' + jM'' \tag{1}$$

where  $\epsilon'$ ,  $M'$  are the real and  $\epsilon''$ ,  $M''$  the imaginary parts of dielectric permittivity and electric modulus, respectively. In the present study, experimental data were analysed via the electric modulus formalism. The interpretation of relaxation phenomena via the electric modulus formalism offers some advantages upon other treatments, since large variations in the permittivity and loss at low frequencies and high temperatures are minimized. Further, difficulties occurring from the electrode nature, the electrode-specimen contact and the injection of space charges and absorbed impurities can be neglected. Arguments concerning the resulting benefits

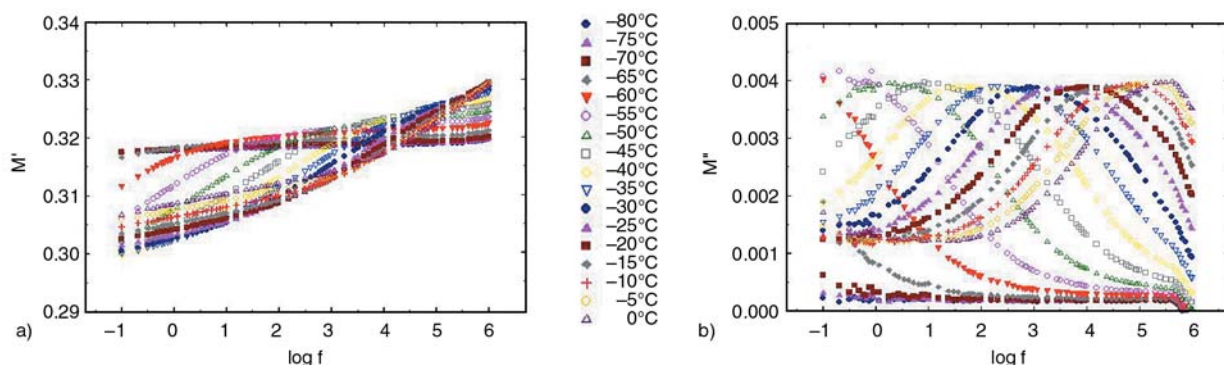
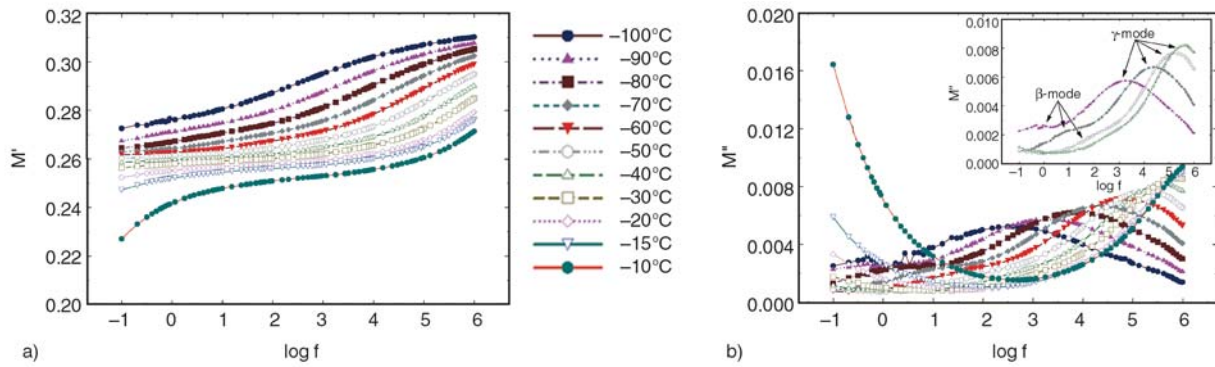


Figure 1. Real (a) and imaginary (b) part of electric modulus as a function of frequency for the NR specimen, in the low temperature range



**Figure 2.** Real (a) and imaginary (b) part of electric modulus as a function of frequency for the PUR specimen, in the low temperature range. Inset presents isothermal plots at four selected temperatures

of the electric modulus presentation have been presented elsewhere [13–15].

The dielectric response of NR in the low temperature range is presented in Figure 1. NR is a non-polar polymer with glass transition temperature ( $T_g$ ) very close to  $-64^\circ\text{C}$  [12]. In the isothermal dielectric scans of NR (Figure 1) only one relaxation process is present. This process is recorded in the low temperature range, as expected, and is related to the glass/rubber transition of NR. Since no other processes are observed in the dielectric spectra of NR, its high temperature response is not presented here for the sake of brevity. Figures 2 and 3 depict the dielectric response of pure PUR in the low and high temperature ranges respectively. As it can be seen, PUR is a dielectrically active polymer exhibiting four distinct relaxation processes. All the recorded processes become evident via the step like transition from low to high values of the real part of electric modulus ( $M'$ ) and the corresponding peak of the imaginary part of electric modulus ( $M''$ ). In some cases adjacent peaks are superimposed and the resulting dielectric spectrum consists of a ‘shoulder-like’ peak next to

a well defined one. In the low temperature range, (Figure 2), two relatively fast processes occur, which are attributed, with descending frequency, to a ‘crankshaft’ type motion of the  $(\text{CH}_2)_n$  sequence in the soft part of PUR ( $\gamma$ -mode) and to re-orientation of polar side groups of the main chain ( $\beta$ -mode). Inset in Figure 2b provides isothermal plots of  $M''$  versus frequency at four selected temperatures. The relaxation peak of  $\gamma$ -mode is clearly formed at high frequencies, while  $\beta$ -mode is recorded in the low frequency edge. At higher temperatures, (Figure 3), two more mechanisms are clearly recorded. The one at higher frequencies, is ascribed to glass/rubber transition of PUR ( $\alpha$ -mode), while the slow process is attributed to Interfacial Polarization (IP) or Maxwell-Wagner-Sillars (MWS) effect. Since electrode polarization is neglected in the electric modulus formalism [13–15] and the conductivity of all the tested specimens was low (Table 1) the slower process is unambiguously assigned to IP. IP appears in media exhibiting heterogeneity due to the accumulation of charges at the interfaces and the formation of large dipoles, which attempt to follow the alternation of the

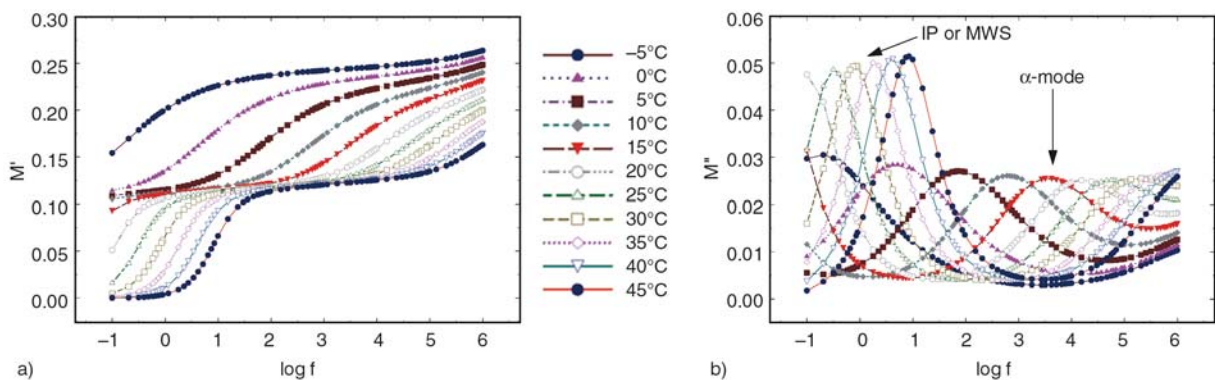


**Figure 3.** Real (a) and imaginary (b) part of electric modulus as a function of frequency for the PUR specimen, in the high temperature range

**Table 1.** Values of conductivity ( $\sigma$ )\*, at three temperatures, for all the examined systems

Sample	$\sigma$ [S·cm <sup>-1</sup> ]		
	-50°C	0°C	50°C
NR	2.06·10 <sup>-15</sup>	1.01·10 <sup>-15</sup>	1.07·10 <sup>-13</sup>
PUR	7.40·10 <sup>-16</sup>	3.83·10 <sup>-14</sup>	7.21·10 <sup>-11</sup>
PUR/NR	8.89·10 <sup>-16</sup>	1.44·10 <sup>-14</sup>	6.79·10 <sup>-11</sup>
NR+10 phr LS	2.99·10 <sup>-15</sup>	6.82·10 <sup>-15</sup>	3.62·10 <sup>-12</sup>
PUR+10 phr LS	2.63·10 <sup>-14</sup>	8.93·10 <sup>-13</sup>	8.99·10 <sup>-11</sup>
PUR/NR+10 phr LS	8.89·10 <sup>-16</sup>	1.44·10 <sup>-14</sup>	6.79·10 <sup>-11</sup>

\*Conductivity values correspond to the lowest measured frequency of 10<sup>-1</sup> Hz

applied electric field. IP is a slow relaxation process because of the inertia of the formed dipoles to acquire the orientation of the field. The repeat unit of PUR chain is composed by stiff, rigid blocks and soft rubbery blocks. In that sense IP arises from ionic polarization occurring at the interface of hard and soft regions as well as from variations of the morphology between amorphous and crystalline segments [16–18].

The dielectric spectra of the PUR/NR blend include contributions from both polymers, and thus in the

low temperature range (Figure 4) the fast processes of local motions of small parts ( $\beta$  and  $\gamma$ -modes) of the PUR chain as well as the  $\alpha$ -mode of NR are present. All three mechanisms occur, more or less, in the same frequency range and since the rate of peak shift with temperature varies from mode to mode, in many isothermal scans, peaks of different modes are superimposed, resulting in a complex curve. Furthermore, in the high temperature region, (Figure 5), two sets of peaks are obvious, corresponding to PUR's  $\alpha$ -mode and IP respectively.

The real ( $M'$ ) and imaginary ( $M''$ ) part of electric modulus for the NR+10 phr LS specimen, at low temperatures, is depicted in Figure 6. The dielectric profile of the LS reinforced NR resembles to that of the pure matrix. Besides glass/rubber transition of NR ( $\alpha$ -mode) a second mechanism becomes apparent through the formation of broad or double peaks in the loss modulus ( $M''$ ) index. The existence of an additional phase (viz. LS) introduces heterogeneity to the system leading to the appearance of IP. Previous work [11, 12] has shown that LS is less intercalated by NR than by PUR. Thus it is reasonable

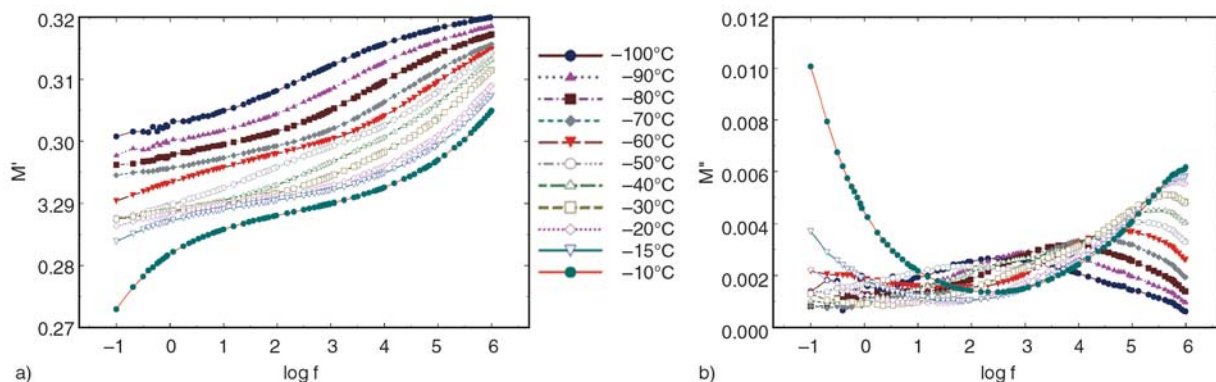


**Figure 4.** Real (a) and imaginary (b) part of electric modulus as a function of frequency for the PUR/NR specimen, in the low temperature range

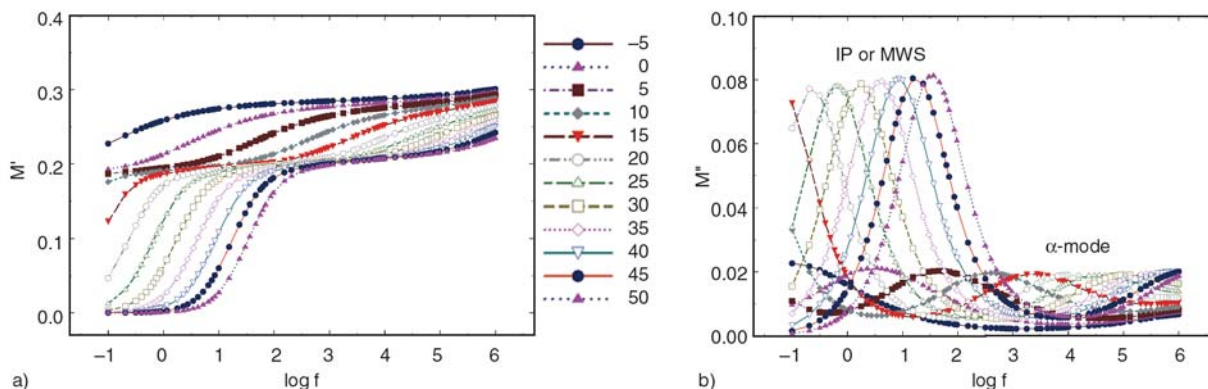


**Figure 5.** Real (a) and imaginary (b) part of electric modulus as a function of frequency for the PUR/NR specimen, in the high temperature range

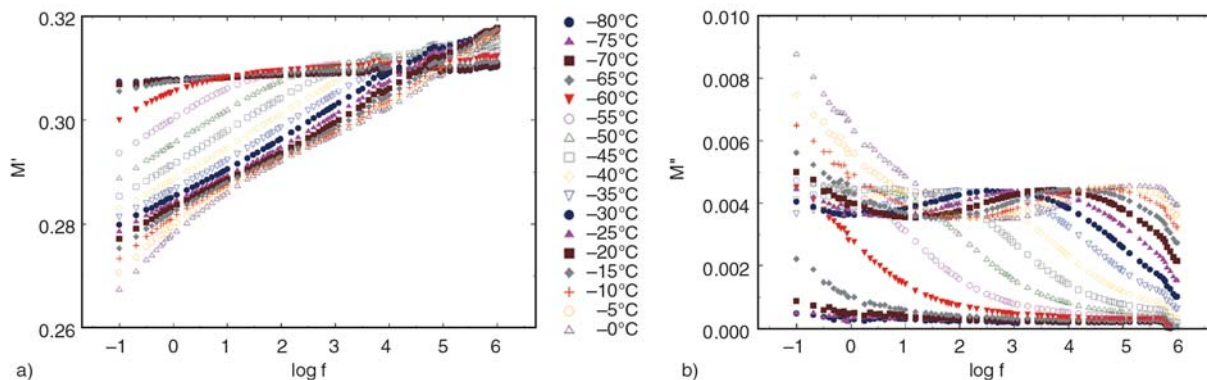


**Figure 6.** Real (a) and imaginary (b) part of electric modulus as a function of frequency for the NR+10 phr LS specimen, in the low temperature range

to suggest the co-existence of regions where LS remain immiscible with NR, leading to microphase separated composite structure, and regions where LS is intercalated by NR. These different morphologies affect both IP and  $\alpha$ -mode. The interface between non-intercalated galleries of LS and NR gives rise to the formation of large dipoles, enhancing the electrical inertia of interfacial relaxation phenomenon, leading to slower motion or greater relaxation time. On the other hand, the interface between NR and intercalated LS results in the formation of relatively smaller dipoles allowing faster motion. Consequently, it is possible that the observed IP or MWS effect consists of two contributions, which differ in their relaxation rate. In addition, intercalation of polymer chains within the layers results in increased relaxation rate or lower glass transition temperature [12, 19, 20], since the isolated polymer molecules are not involved in cooperative molecular motions. The influence of all the above contributions is reflected in the broad and complex shape of the loss modulus ( $M''$ ) curve with frequency (Figure 6b). For the same reasons, as in

the case of pure NR, the high temperature dielectric response of NR+10 phr LS is omitted.

Figures 7 and 8 depict the dielectric behaviour of the PUR/NR+10 phr LS nanocomposite in the low and high temperature range respectively. Relaxations arising from IP as well as the contributions from both polymers (NR  $\alpha$ -mode, PUR  $\alpha$ ,  $\beta$  and  $\gamma$ -modes) are recorded in the dielectric spectra. Finally, in Figures 9 and 10, the response of the PUR+10 phr LS nanocomposite is shown. The recorded relaxation mechanisms are, from the slower to the faster one, IP, glass/rubber transition ( $\alpha$ -mode), and local motions of small parts of the polymer chain ( $\beta$  and  $\gamma$ -mode), as expected. In the low temperature region, (Figure 9), the existence of two processes becomes evident mostly via the transitions of the real part of electric modulus ( $M'$ ), from low to high values, with frequency. The shape of the transitions, or more generally speaking, the variation of  $M'$  with frequency resembles that of PUR. In the plots of electric modulus loss index ( $M''$ ), (Figure 9b), broad peaks are formed, with the location of their maxima shifted to lower frequen-

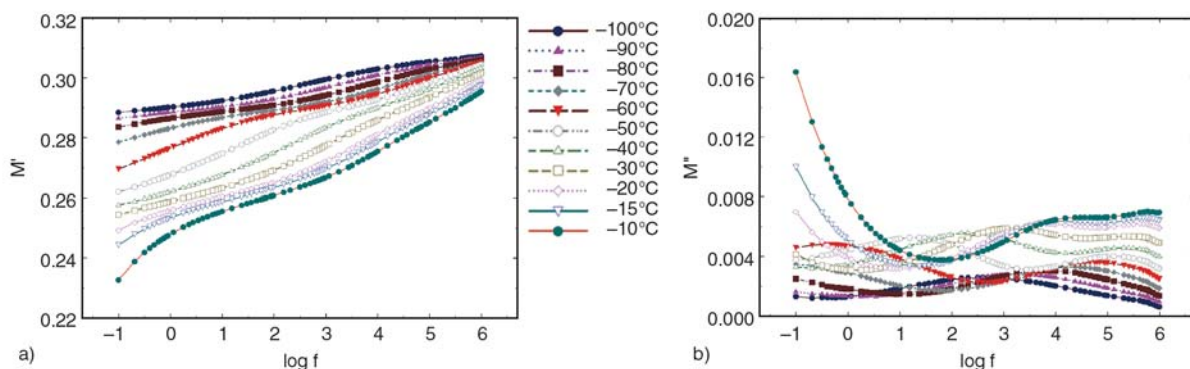


**Figure 7.** Real (a) and imaginary (b) part of electric modulus as a function of frequency for the PUR/NR+10 phr LS specimen, in the low temperature range

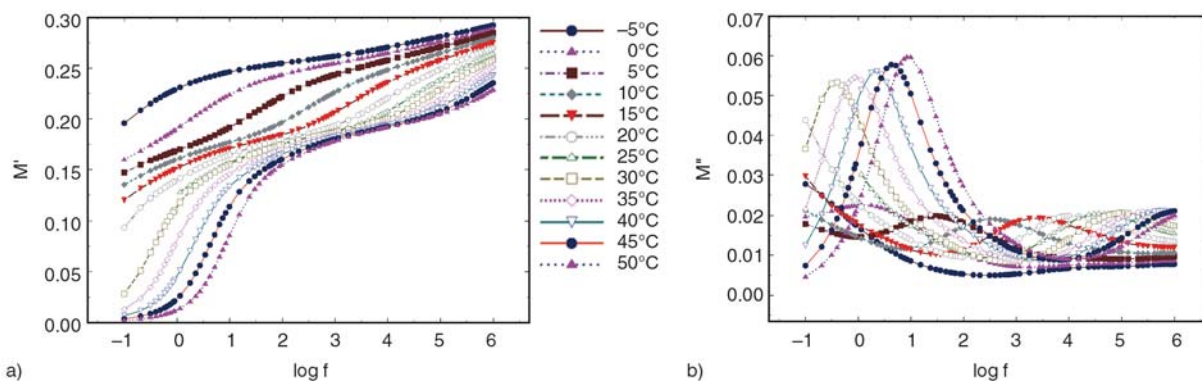


**Figure 8.** Real (a) and imaginary (b) part of electric modulus as a function of frequency for the PUR/NR+10 phr LS specimen, in the high temperature range

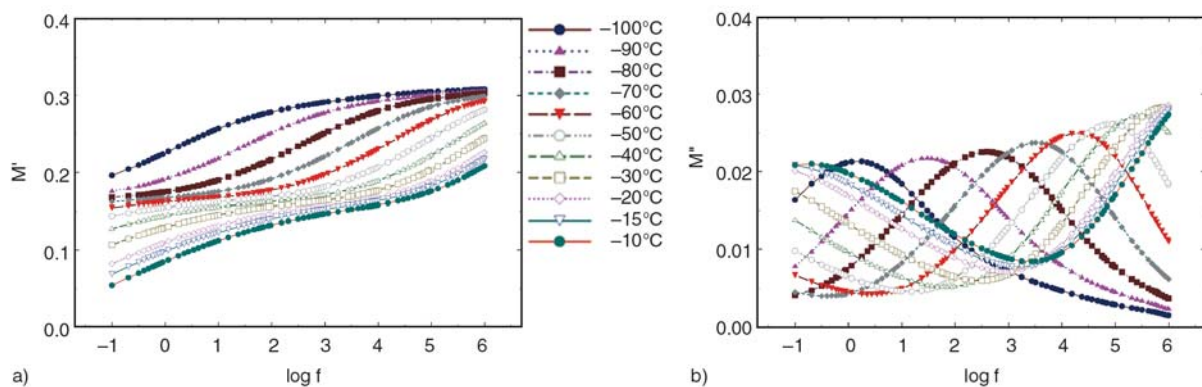


**Figure 9.** Real (a) and imaginary (b) part of electric modulus as a function of frequency for the PUR+10 phr LS specimen, in the low temperature range

cies compared to the corresponding peaks of PUR. In the case of pure PUR,  $\gamma$ -mode is more pronounced and  $\beta$ -mode is evident, at lower frequencies, as a shoulder-like peak. On the contrary, loss spectra of PUR+10 phr LS nanocomposite exhibit a clear peak in the same frequency range where  $\beta$ -mode is observed in PUR. This peak is superimposed with the peak of  $\gamma$ -mode on the high frequency edge. The inversion of the relative intensity between  $\beta$  and  $\gamma$ -modes could be an initial indication that the presence of LS restricts the evolution of  $\gamma$ -process. Since,  $\gamma$ -mode has been attributed to a ‘crankshaft’ type motion of the  $(\text{CH}_2)_n$  sequence in the soft part of PUR chain, intercalated polymer molecules might not be able to follow the alternation of the field, repealing, up to a point, the motion of methyl groups. In the high temperature dielectric spectra of PUR+10 phr LS, IP and  $\alpha$ -mode are detected. However, the behaviour differs in PUR+10 phr LS since this is the only case where the amplitude of the recorded IP peak is lower than the corresponding of glass/rubber relaxation ( $\alpha$ -mode). Interfacial relaxation phenomena are prominent in

the low frequency range and relatively high temperatures, resulting in high values of both real and imaginary part of dielectric permittivity [14, 15, 21]. Further increase of the intensity of interfacial effects results in even higher values of  $(\epsilon')$  and  $(\epsilon'')$ . On the other hand, in the electric modulus presentation, the increase of intensity of IP (MWS effect) is demonstrated by reduced values of  $M'$  and  $M''$ . Thus it can be concluded that the lower values of the modulus loss index ( $M''$ ) is a strong indication for the existence of pronounced interfacial phenomena in the PUR+10 phr LS system (Figure 10b). Additionally, the broadness of the corresponding peak should be related to interactions between the constituents of the nanocomposite. Previous studies [11, 12] upon the morphology of PUR+10 phr LS have shown the existence of two intercalated populations with different interlayer distances, namely 1.23 and 1.73 nm. Moreover, the presence of isolated silicate layers due to partial exfoliation cannot be excluded. Under this point of view, interfaces with varying geometrical characteristics contribute to interfacial relaxation phe-

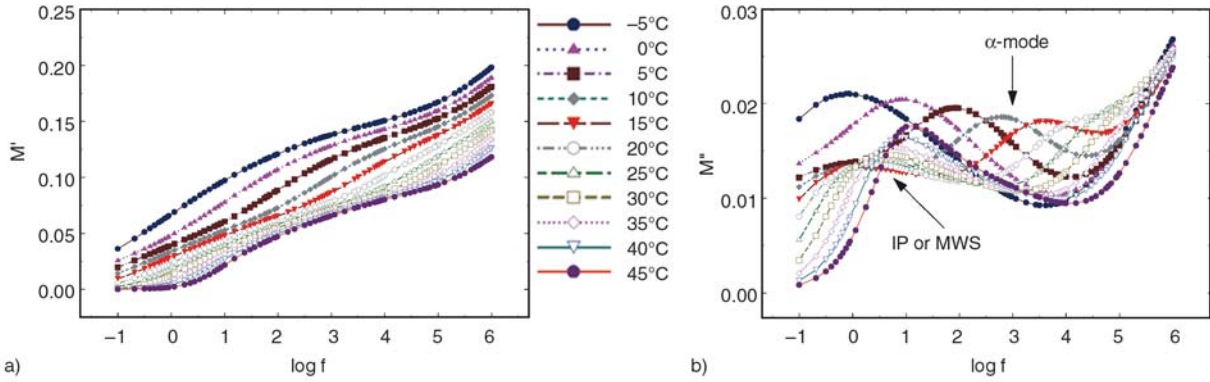


**Figure 10.** Real (a) and imaginary (b) part of electric modulus as a function of frequency for the PUR+10 phr LS specimen, in the high temperature range

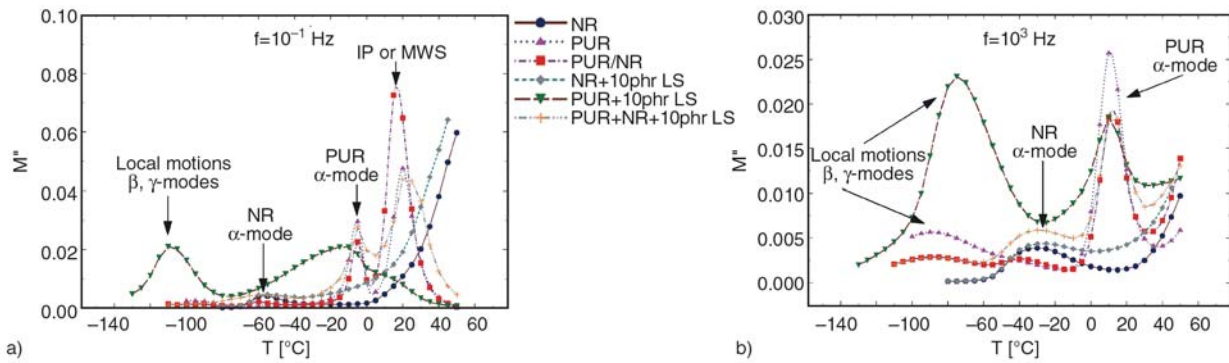


**Figure 11.** Imaginary part of electric modulus as a function of temperature for all the examined specimens at (a)  $f = 10^{-1}$  Hz and (b)  $f = 10^3$  Hz

nomena with different dynamics or relaxation times. Superposition of all interfacial effects forms the recorded broad peak.

For reasons of comparison, isochronal plots of all the examined systems are presented in Figure 11. The occurring relaxation mechanisms are indicated by arrows, and a direct comparison, supporting the above discussion, can be easily conducted.

It is well known, from dielectric theory, that the frequency-temperature superposition shifts the loss peak position of relaxation processes to higher frequencies with increasing temperature. The temperature dependence of the electric modulus loss ( $M''$ ) maxima loci for both IP and  $\alpha$ -mode, is depicted in Figure 12, for all the examined systems. The temperature dependence of peak shift is a measure of the relaxation rate of the specific process. IP follows the Arrhenius type temperature dependence, which is expressed by the Equation (2):

$$f = f_0 \exp\left(-\frac{E_A}{k_B T}\right) \quad (2)$$

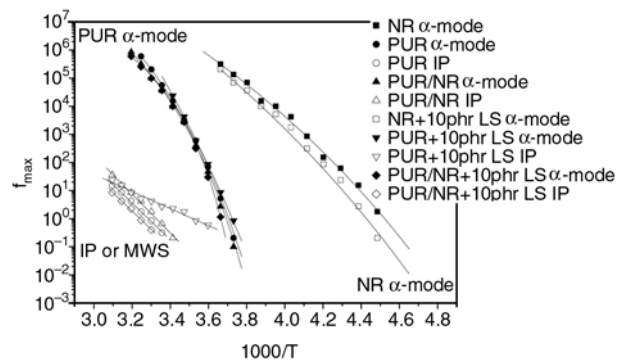


**Figure 12.** Loss peak position as a function of inverse temperature of the slow processes (IP and  $\alpha$ -mode), for all the examined specimens

where  $E_A$  is the activation energy,  $f_0$  pre-exponential constant and  $k_B$  the Boltzmann constant. In contrary, the temperature dependence of  $\alpha$ -mode deviates from Equation (2) following the Vogel-Fulcher-Tamann (VTF) equation, which considers that relaxation rate increases rapidly at lower temperatures because of the reduction of the free volume.

VTF equation is given by (3):

**Table 2.** Values of activation energy, calculated via Equation (2), for the IP mode and fitting parameters of Equation (3) for  $\alpha$ -mode

Sample	A [K <sup>-1</sup> ]	T <sub>0</sub> [K]	E <sub>A</sub> [eV]
NR	25.7	128	–
PUR	8.3	215	1.29
PUR/NR	5.8	225	1.37
NR+10 phr LS	35.0	120	–
PUR+10 phr LS	33.0	165	0.60
PUR/NR+10 phr LS	2.4	246	1.29

$$f = f_0 \exp\left(-\frac{AT_0}{T - T_0}\right) \quad (3)$$

where  $f_0$  is a pre-exponential factor,  $A$  a constant (being a measure of the activation energy), and  $T_0$  Vogel temperature or ideal glass transition temperature. The values of activation energy for IP-mode, calculated via linear regression, as well as all fitted parameters of Equation (3), for each of the tested systems, are listed in Table 2. Going back to Figure 12 three sets of curves can be distinguished. The first one, recorded at the higher temperatures, corresponds to IP. As it can be seen, all curves display proximity with the only exception of PUR+10 phr LS nanocomposite. The slope of this curve deviates remarkably leading to a significantly lower value of activation energy (Table 2) implying an easier activated relaxation process. The second set of curves corresponds to  $\alpha$ -mode of PUR and is recorded at intermediate temperatures. Finally, the third set recorded at low temperatures, corresponds to  $\alpha$ -mode of NR.

#### 4. Conclusions

Based on the experimental data from dielectric spectroscopy and the analysis carried out the following conclusions can be drawn. NR is a material of low dielectric permittivity and loss, and its  $\alpha$ -mode is recorded in the low temperature range due to its low glass transition temperature. PUR is a dielectrically active polymer exhibiting four distinct relaxation processes, namely IP, glass/rubber transition ( $\alpha$ -mode),  $\beta$ - and  $\gamma$ -relaxation modes resulting from the motion of polar side groups and local motions of small chain segments (motions of the  $(\text{CH}_2)_n$  sequences). The same processes can be detected in all systems containing PUR. Interfacial Polarization is present in all nanocomposites and is

detected in the low frequency range and relatively high temperatures, being the slowest recorded process. Finally, pronounced interfacial relaxation phenomena, occurring in the PUR+10 phr LS spectra, are attributed to the existence of different intercalated populations and to possible partial exfoliation of LS.

#### Acknowledgements

This work was supported by the PPP IKYDA 2005 program between DAAD and IKY (Greek State Scholarships Foundation).

#### References

- [1] Thostenson E. T., Ren Z., Chou T-W.: Advances in the science and technology of carbon nanotubes and their composites: A review. *Composites Science and Technology*, **61**, 1899–1912 (2001).
- [2] Karger-Kocsis J., Wu C-M.: Thermoset rubber/layered silicate nanocomposites. Status and future trends. *Polymer Engineering and Science*, **44**, 1083–1093 (2004).
- [3] Jordan J., Jacob K. I., Tannenbaum R., Sharaf M. A., Jasiuk I.: Experimental trends in polymer nanocomposites: A review. *Materials Science and Engineering, Part A: Structural Materials*, **393**, 1–11 (2005).
- [4] Auad M. L., Nutt S. R., Pettarin V., Frontini P. M.: Synthesis and properties of epoxy-phenolic clay nanocomposites. *Express Polymer Letters*, **1**, 629–639 (2007).
- [5] Tanaka T., Montari G. C., Mülhaupt R.: Polymer nanocomposites as dielectrics and electrical insulation-perspectives for processing technologies, materials characterization and future applications. *IEEE Transactions on Dielectrics and Electrical Insulation*, **11**, 763–783 (2004).
- [6] Montari G. C., Fabiani D., Palmieri F., Kaempfer D., Thomann R., Mülhaupt R.: Modification of electrical properties and performance of EVA and PP insulation through nanostructure by organophilic silicates. *IEEE Transactions on Dielectrics and Electrical Insulation*, **11**, 754–762 (2004).
- [7] Pegoretti A., Dorigato A., Penati A.: Tensile mechanical response of polyethylene-clay nanocomposites. *Express Polymer Letters*, **1**, 123–131 (2007).
- [8] Abacha N., Kubouchi M., Tsuda K., Sakai T.: Performance of epoxy-nanocomposite under corrosive environment. *Express Polymer Letters*, **1**, 364–369 (2007).
- [9] Fréchet M. F., Trudeau M., Alamdari H. D., Boily S.: Introductory remarks on nanodielectrics. in 'IEEE Conference on Electrical Insulation and Dielectric Phenomena (CEIDP). Kitchener, Canada', 92–99 (2001).

- [10] Kremer F., Schönhals A.: Broadband dielectric measurement techniques ( $10^{-6}$  Hz to  $10^{12}$  Hz). in 'Broadband dielectric spectroscopy' (ed(s): Kremer F., Schönhals A.) Springer, Berlin, 35–64 (2003).
- [11] Varghese S., Gatos K. G., Apostolov A. A., Karger-Kocsis J.: Morphology and mechanical properties of layered silicate reinforced natural and polyurethane rubber blends produced by latex compounding. *Journal of Applied Polymer Science*, **92**, 543–551 (2004).
- [12] Psarras G. C., Gatos K. G., Karger-Kocsis J.: Dielectric properties of layered silicate reinforced natural and polyurethane rubber nanocomposites. *Journal of Applied Polymer Science*, **106**, 1405–1411 (2007).
- [13] Tsangaris G. M., Psarras G. C., Kouloumbi N.: Electric modulus and interfacial polarization in composite polymeric systems. *Journal of Materials Science*, **33**, 2027–2037 (1998).
- [14] Psarras G. C., Manolakaki E., Tsangaris G. M.: Electrical relaxations in polymeric particulate composites of epoxy resin and metal particles. *Composites, Part A: Applied Science and Manufacturing*, **33**, 375–384 (2002).
- [15] Psarras G. C., Manolakaki E., Tsangaris G. M.: Dielectric dispersion and ac conductivity in-iron particles loaded-polymer composites. *Composites, Part A: Applied Science and Manufacturing*, **34**, 1187–1198 (2003).
- [16] Pissis P., Kanapitsas A., Savelyev Y. V., Akhranovich E. R., Privalko E. G.: Influence of chain extenders and chain end groups on properties of segmented polyurethanes. II. Dielectric study. *Polymer*, **39**, 3431–3435 (1998).
- [17] Korzhenko A., Tabellout M., Emery J. R.: Influence of a metal-polymer interfacial interaction on dielectric relaxation properties of polyurethane. *Polymer*, **40**, 7187–7195 (1999).
- [18] Gatos K. G., Martínez Alcázar J. G., Psarras G. C., Thomann R., Karger-Kocsis J.: Polyurethane latex/water dispersible boehmite alumina nanocomposites: Thermal, mechanical and dielectrical properties. *Composites Science and Technology*, **67**, 157–167 (2007).
- [19] Elmahdy M. M., Chrissopoulou K., Afratis A., Floudas G., Anastasiadis S. H.: Effect of confinement on polymer segmental motion and ion mobility in PEO/Layered silicate nanocomposites. *Macromolecules*, **39**, 5170–5173 (2006).
- [20] Anastasiadis S. H., Karatasos K., Vlachos G., Manias E., Giannelis E. P.: Nanoscopic-confinement effects on local dynamics. *Physical Review Letters*, **84**, 915–918 (2000).
- [21] Tsangaris G. M., Psarras G. C.: The dielectric response of a polymeric three-component composite. *Journal of Materials Science*, **34**, 2151–2157 (1999).

# Thermal, dielectric and mechanical study of poly(vinyl chloride)/olive pomace composites

H. Djidjelli<sup>1\*</sup>, D. Benachour<sup>2</sup>, A. Boukerrou<sup>1</sup>, O. Zefouni<sup>1</sup>, J. Martinez-Véga<sup>2</sup>, J. Farenc<sup>2</sup>, M. Kaci<sup>1</sup>

<sup>1</sup>Laboratoire des Matériaux Organiques, University A. Mira of Bejaia, Bejaia, Algeria

<sup>2</sup>University Ferhat Abbas, Setif, Algeria

<sup>3</sup>Laboratoire de Génie Electrique, (UMR-CNRS 5003) Université Paul Sabatier, Toulouse, France

Received 3 September 2007; accepted in revised form 25 November 2007

**Abstract.** Composites from PVC and chemically treated olive pomace have been prepared. The effect of the incorporation of virgin and benzylated olive pomace in the poly(vinyl chloride) matrix on dielectric, mechanical and thermal stability properties, of /olive pomace composites was studied.

The mechanical properties of the benzylated composites were improved. Furthermore, the thermal characterization of the different samples carried out by thermogravimetric analysis revealed an increase in the onset temperatures of decomposition for the treated composites.

The dielectric investigation indicated that the samples containing olive pomace treated with the benzyl chloride can be used in electrical applications as insulators.

**Keywords:** polymer composites, mechanical properties, thermal stability, dielectric properties

## 1. Introduction

Olive pomace is an industrial byproduct of the olive oil production process that is obtained by squeezing the olive pulp without any chemical treatment. By water addition, three phases occur: oil, water and pomace. Chemically, the virgin olive pomace contains cellulose, hemicellulose and lignin, and cannot be processed as plastics due to both the high degree of crystallinity of the cellulose and the three-dimensional network.

In the last decade, wood-derived fillers have become more accepted in the thermoplastic industry. Polymer composites filled with natural lignocellulosic fibers have attracted the attention of many researchers and technologists [1–5]. Both polymer matrices and natural filler systems have been widely investigated [6–10]. As a matter of fact, Oksman and Lindberg [11] as well as the team

of Liao [12] studied the mechanical behavior of composites based on polyethylene and wood flour samples [11, 12]. On the other hand, Zaini *et al.* [13], Nitz *et al.* [14], and Kaci *et al.* [15, 16] investigated the mechanical behavior of polypropylene/wood flour composites. Some authors examined also the mechanical behavior of PS/PEHD/wood flour [17]. The electrical properties of SBR/PS blend and chemically treated wood flour have been investigated by the team of Mansour [18].

On the contrary, the research work dealing with PVC/wood flour composites is rather scarce. Although, some papers have been reported in literature including those of Matuana and Mengelöglu [19], Pedro *et al.* [20] devoted to a comparative study of the mechanical behavior of PVC/CaCO<sub>3</sub> with PVC/agalmatolithe, while Sain *et al.* investigated the filled PE/WF, PVC/WF et PP/WF formulations [21].

\*Corresponding author, e-mail: [hocdjidjidj@yahoo.fr](mailto:hocdjidjidj@yahoo.fr)  
© BME-PT and GTE

On the other hand, there are only a few works reported in the literature on olive pomace rejects and their uses in many applications involving mainly the production of thermal energy, fertilizer as well as food for animals [22–25].

In the present work, Algerian olive pomace was used as filler to reinforce polyvinylchloride composites. Thus decrease in amount of PVC in use and can accelerate its degradation. Every year, during the season of transformation of olive to oil, thousands tons of olive pomace are rejected to nature or incinerated causing environmental pollution. The recovery of this renewable waste may have a double positive impact, economic and ecological.

To solve the problem of the processability, it is proposed to plasticize the olive pomace by chemical treatment with benzyl chloride, this treatment have been already done by Hartman *et al.* [26], Lu and Zhang [27] and the results have proved that the polysaccharide-based natural polymers can be plasticized and processed. Therefore better processability of the composite materials and higher interfacial adhesion between the polymer and the filler are expected.

## 2. Experimental part

### 2.1. Materials

All the PVC-Olive pomace composite formulations used in this work were prepared based on PVC type 4000 M produced by the Algerian Company named 'Entreprise Nationale des Industries Pétrochimiques-ENIP' in Skikda on the Eastern Coast of Algeria. The polymer has the following physical characteristics:  $K_{value}$ , 67; powder density, 0.56 g·ml<sup>-1</sup>; thermal stability, 60 min at 180°C according to DIN 53381 part 1. The additives used in the preparation of the various formulations were di(2-ethyl-hexyl phthalate) (DEHP) as a plasticizer produced by ENIP SKIKDA, Algeria, with a vis-

cosity ranging from 80 to 85 mPa·s, a molecular weight of 390 g·mol<sup>-1</sup>, a boiling temperature of 233°C, a thermal stabilizer system based on Ba-Zn type LANKRO-MARK LZB325 produced by Akros Chemicals Ltd. U.K. and epoxidized Soya bean oil (ESBO) as co-stabilizer and a lubricant.

The blend obtained with PVC resin and the different additives (dry blend) were used to prepare the composites formulations. Olive pomace was used as filler having a length of around 100 µm.

### 2.2. Chemical treatment of olive pomace by benzylation

The Algerian olive pomace was subjected to several pretreatments, i. e. washing with hot water to eliminate pulp, drying under ambient conditions for 24 h then in a drying oven at 80°C for 24 h, crushing and finally sifting to obtain a flour of size lower than 100 µm which was dried under vacuum at 80°C for 12 hours.

After being pre-swelled by 18% NaOH for 1 h, the powder was transferred into a flask containing phase transfer catalyst and benzyl chloride.

The reaction was carried out under vigorous stirring at 120°C for 4 h at reflux. The products were purified through washing for several times with distilled water to remove inorganic salts, and with ethanol to remove residues of benzyl chloride. Finally, the treated flour was dried again under vacuum at 60°C for 72 h to be used as filler in composite matrix.

Five formulations of PVC with the olive pomace were prepared, the reference F0 only made of PVC without olive pomace, two formulations with PVC and the untreated olive pomace at 5 and 25% by weight noted by F5 and F25 and finally two formulations PVC with the treated olive pomace with benzyl chloride at 5 and 25% by weight noted by F5B and F25B. The mass composition of the several formulations was reported in Table 1.

**Table 1.** Mass composition of the various PVC formulations

Components	Formulations						
	F0	F5	F15	F25	F5B	F15B	F25B
PVC resin	100	100	100	100	100	100	100
(DEHP)	30	30	30	30	30	30	30
Ba-Zn	0.2	0.2	0.2	0.2	0.2	0.2	0.2
ESBO	0.5	0.5	0.5	0.5	0.5	0.5	0.5
Virgin olive pomace	0	5	15	25	0	0	0
Benzylated olive pomace	0	0	0	0	5	15	25

### 2.3. Sample preparation

Blends based on PVC powder, various additives, and olive pomace before and after treatment were placed in a high-speed twin steel-wall mixer and processed at a speed of 3000 rpm at 50°C, below the glass transition temperature of PVC to avoid gelification.

The different PVC formulations obtained were used to prepare preblended films by calendaring process at 160°C with a residence time of 8 min. The films obtained were placed in an aluminum mold which was placed between two steel platens. A *Fontume Holland* hydraulic oil heated press with a nominal maximum pressure level up to 250 kN was used for compression molding. The press platens were maintained at 170°C for 3 min. The plates obtained are 2 mm thick and they will be used for testing. The sample preparation was carried out in the laboratory of CABEL ‘*Cablerie Electrique*’ located in Algiers (Algeria).

### 2.4. Spectroscopic analysis

FTIR measurements were carried out on a SPECTRUM 100 Fourier-transform infrared spectrophotometer at a resolution of 4 cm<sup>-1</sup> with an accumulation of 100 scans for each spectrum. The infrared spectra were recorded in absorbance units in the 4000–400 cm<sup>-1</sup> range. FTIR spectra were measured in KBr pellets containing 1% finely ground samples.

### 2.5. Mechanical properties

Five samples of each test were used to determine tensile and impact properties. The tensile test was performed on a ZWICK/ROEL Z 2.5 tensile testing apparatus at a cross-head speed of 10 mm/min, according to ISO 527-1 procedure. The size of the specimen was 75×13×4 mm.

### 2.6. Thermal stability

For thermal stability analysis, the decomposition rates were measured by a SETARAM TGT DTA 92 thermogravimetric apparatus. A sample of initial mass of 15 to 20 mg was introduced into a platinum crucible; the sample mass (TG) variation was then measured as a function of temperature (or time), and the rates of mass loss (DTG) were determined by using a thermobalance under an inert argon

atmosphere up to 600°C, at a heating rate of 10°C min<sup>-1</sup>.

The onset of decomposition temperature corresponds to the inflexion point of the TG curve.

### 2.7. Dielectric properties

Permittivity and dielectric loss measurements were measured by using a dielectric spectrometer, type DEA2970. The apparatus allows the measurements of various dielectric properties over a large range of temperatures and frequencies at heating rate of 2°C/min.

## 3. Results and discussion

### 3.1. Characterization of olive pomace

FTIR spectra of olive pomace before and after benzylation are illustrated in Figure 1. It can be observed clearly that the chemical structure of benzylated olive pomace is quite different from that of the untreated one. The intensity of the absorption band of hydroxyl groups which appear at about 3500 cm<sup>-1</sup> decreases after benzylation process as a result of etherification. This broad band at 3500 cm<sup>-1</sup> cannot be assigned to the presence of water in the samples and, possibly in KBr because both the samples and KBr, before the FTIR analysis, were subjected to heat treatment in an oven at 80°C until the weight of the sample was constant. Results obtained from infrared spectra prove that the hydroxyl concentration decreases with the chemical treatment because the hydroxyl groups are substituted by the benzyl groups. This in addition, a reduction in the absorption band which appears at 1730 cm<sup>-1</sup> corresponding to the carbonyl groups is well detected for benzylated olive pomace sample compared to the untreated sample. This

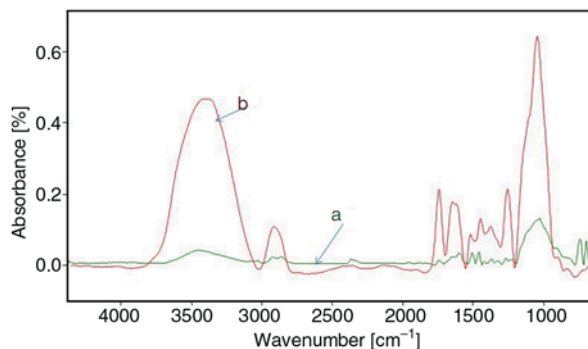


**Figure1.** FTIR spectra of a: untreated olive pomace and b: benzylated olive pomace

reduction can be attributed to the partial extraction of the lignin and the hemicellulose which contain these groups by the chemical treatment [21]. The appearance of a new absorption band characteristic of the phenyl groups located approximately at  $736\text{--}695\text{ cm}^{-1}$ . This band is nonexistent in FTIR spectra of the untreated olive pomace, that indicates that the reaction of the monosubstitution of the sodium ions by the benzyl groups occurred.

Instead, the degree of advance of this reaction can be evaluated by measuring the weight gain of the sample at the end of the reaction. This weight gain is attributed to the fact that the benzyl groups are heavier than the hydrogen groups. Indeed, it is obtained 30% weight gain of the sample (degree of benzylation of pomace).

### 3.2. Characterization of composites PVC/olive pomace

#### 3.2.1. Mechanical properties

The effect of the olive pomace incorporation on the mechanical properties of PVC/untreated olive pomace composites was examined. Figure 2, 3 and 4 show the mechanical behaviours of different PVC/olive pomace composites before and after treatment.

Generally, the incorporation of untreated olive pomace results in a very similar trend of decrease in both elongation and strain at break. In terms of tensile properties, the decrease of elongation and strength at break was probably caused by a number of factors, including moisture pick-up, poor disper-

sion of olive pomace in the matrix and increase of interfacial defects in debonding between polymer and olive pomace. The results obtained were in a good correlation with those found by Sombatsompop and Chaochanchaikul with the samples of PVC/sawdust composites [28]. The tensile properties of highly viscous thermoplastics, rubber materials or plasticized PVC depend on several factors, such as dispersion of fiber, increase in stress concentration at fiber ends and amount of air retained in the composite during mixing [19]. However it can be noticed an increase in both elongation and strength at break for the composite samples prepared with the modified fillers with benzyl chloride. It was found a value of elongation at break of

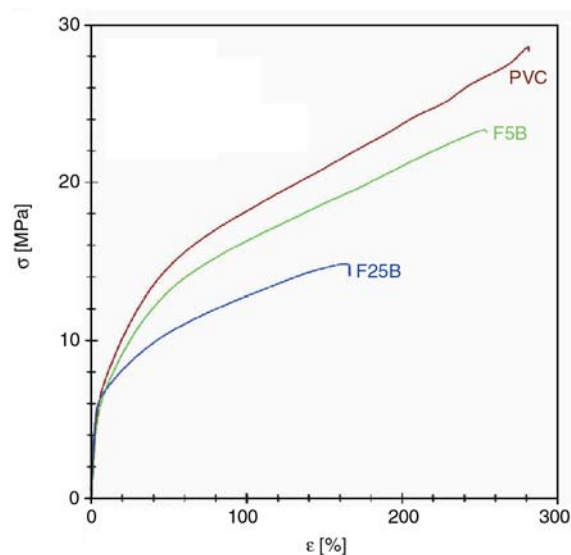


Figure 3. Tensile properties of virgin PVC and PVC/benzyolated olive pomace composites

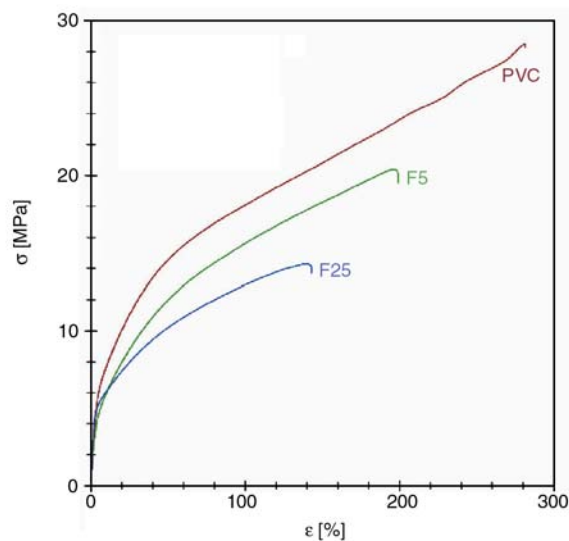


Figure 2. Tensile properties of virgin PVC and PVC/untreated olive pomace composites

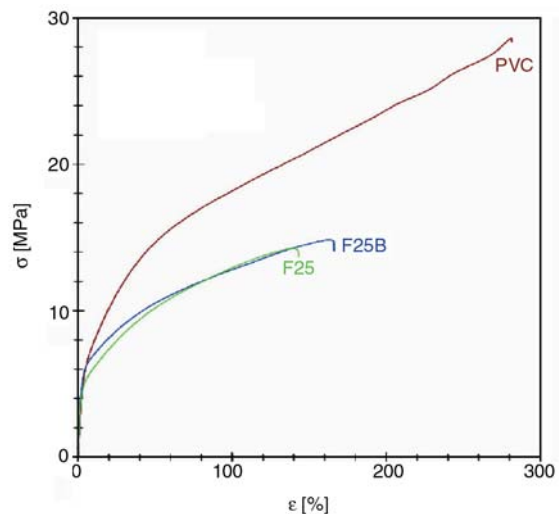


Figure 4. Tensile properties of virgin PVC, PVC/untreated olive pomace and PVC/benzyolated olive pomace composites

almost 141% for the F25 and 166% for the F25B. The improvement of both elongation and strength at break of benzylated composites is due to the thermoplastic character of the benzylated flour of olive pomace and consequently the good interfacial adhesion matrix/filler.

Generally, the tensile test shows clearly that the olive pomace has undergone a plasticization after treatment with benzyl chloride as reported by many authors. The olive pomace has been converted into a thermoplastic material after benzylation and acquired thermoforming ability leading to improvement in the mechanical properties of the composites compared to the untreated ones.

It can be noticed that the Young modulus is influenced by the addition of olive residue and benzylation. The value passes from 71 for F0 to 101 MPa for F25. The incorporation of 25% wt. of untreated olive pomace in the PVC matrix increase the Young modulus by 40%, it provides to the composite higher rigidity because of the rigid filler character. On the other hand, the addition of 25% wt. of olive pomace treated by benzyl chloride, no change in the modulus was observed when compared to that of unloaded PVC matrix. Generally, the tensile test shows clearly that the flour of olive residue has undergone a plasticization after treatment with benzyl chloride.

### 3.2.2. Thermal properties

The different composites were subjected to thermogravimetric analysis in argon atmosphere to understand their thermal behaviour. TG thermograms are shown in Figure 5 and the results are summarized in Table 2.

The data of Table 2 shows clearly that the incorporation of the treated olive pomace or the untreated one in the matrix PVC permits a gain in the onset temperature of the decomposition. In other words, the sample of the loaded PVC present a onset temperature of decomposition higher than that of F0, this is verified for the samples loaded with the vir-

**Table 2.** The effect of the chemical treatment and content of olive pomace on the onset temperature in TGA

Samples	Onset degradation temperature [°C]
F0	239.2
F5	280.3
F5B	286.9
F25	241.0
F25B	253.8

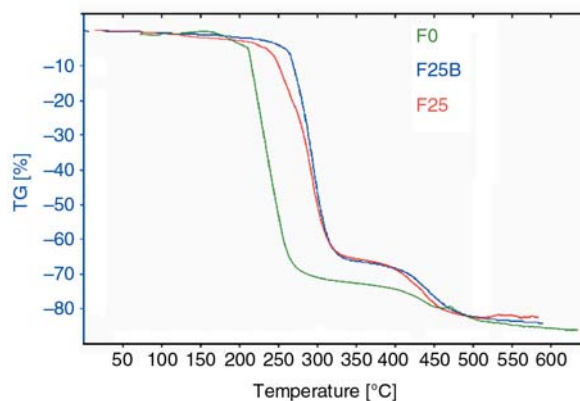


**Figure 5.** TG thermograms of virgin PVC and PVC/untreated and benzyolated olive pomace composites

gin or the treated olive pomace. For example, a gain of 14°C by F25B. Moreover, the effect of the chemical treatment on the onset temperature of the decomposition, a gain of 12°C is recorded by F25B in comparison to F25 sample. Concerning the weight loss recorded in the first stage of the decomposition, we can clearly see that the treated sample has almost the same rate of weight loss and lower than the sample of reference F0. This result is expected considering the treated samples which have undergone an extraction of hemicellulose that is degraded thermally at this temperature range. On the other hand, the samples loaded with the virgin olive pomace present a loss of weight clearly superior to that of F0 which can be explained by the degradation of hemicellulose and PVC at this temperature range.

### 3.2.3. Dielectric properties

The permittivity and dielectric loss factor values for PVC loaded with different concentrations of untreated olive pomace and those treated with benzyl chloride were measured at fixed frequency (100 Hz) and at temperatures ranging from –50 to 130°C.

The effect of temperature on both permittivity and dielectric loss at fixed frequency (100 Hz) for all the samples except F25, are illustrated graphically in Figures 6 and 7. From this figures it is clear that both values increase by increasing temperature, and this increase is slight at temperature ranging from –60 to 0°C, medium between 0 and 40°C and more pronounced after 70°C. For the samples F0, F15, F15B and F25 it is preferable to use them at temperatures not more than 70°C, e.g., the values of the

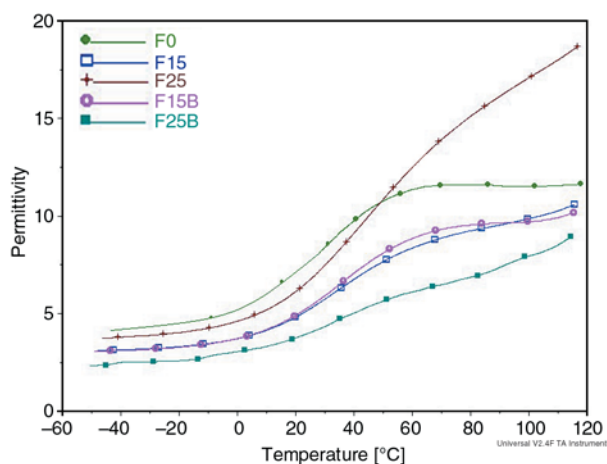


**Figure 6.** The variation of permittivity versus temperature at fixed frequency (100 Hz) for the different composites

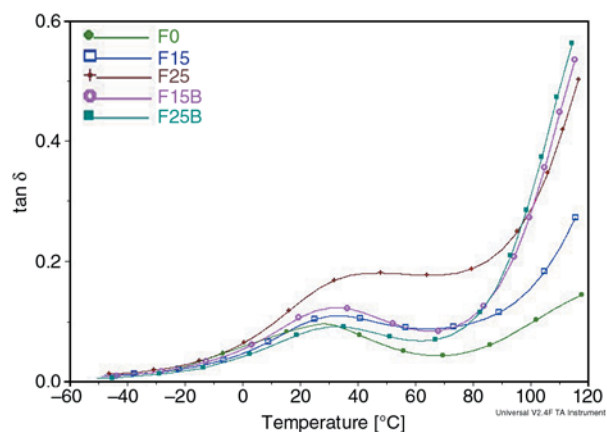


**Figure 7.** The variation of loss factor versus temperature at fixed frequency (100 Hz) for the different composites

dielectric loss rise for the samples of F15B from 0.796 at 70°C to 1.537 at 100°C.

For F25 the sample which contains a sizeable concentration of olive pomace, the increase is pronounced much starting from 0°C and it is not advised to use it in the field of the electric insulation, e.g. the values of the dielectric loss rise for the samples of F25 from 0.298 at 0°C to 2.478 at 70°C. On the other hand with the chemical treatment by benzylation this sample F25B records less important dielectric loss and can be used in insulation purposes.

#### 4. Conclusions

The results of the infrared spectroscopy indicate clearly that the reaction of the monosubstitution of the sodium ions by the benzyl groups was occurred in the structure of the olive pomace.

Also, the incorporation of the treated olive pomace in the PVC matrix improves both elongation and strength at break of benzylated composites; this is due to the thermoplastic character of the benzylated flour of olive pomace and consequently the good interfacial adhesion matrix/filler.

The effect of the chemical treatment on the onset temperature of the decomposition, a gain of 12°C is recorded by F25B in comparison to F25 sample.

On the other hand with the chemical treatment by benzylation this sample F25B records less important dielectric loss and can be used in insulation purposes.

#### References

- [1] Belgacem M. N., Gandini A.: The surface modification of cellulose fibres for use as reinforcing elements in composite materials. *Composite Interfaces*, **12**, 41–75 (2005).
- [2] Marcovich N. E., Aranguren M. I., Reboredo M. M.: Modified woodflour as thermoset fillers Part I. Effect of the chemical modification and percentage of filler on the mechanical properties. *Polymer*, **42**, 815–825 (2001).
- [3] Nunez A. J., Kenny J. M., Reboredo M. M.: Thermal and dynamic mechanical characterization of polypropylene-woodflour composites. *Polymer Engineering and Science*, **42**, 733–742 (2002).
- [4] Marcovich N. E., Reboredo M. M., Aranguren M. I.: Lignocellulosic materials and unsaturated polyester matrix composites: Interfacial modifications. *Composite Interfaces*, **12**, 3–24 (2005).
- [5] Belgacem M. N.: Surface modification of cellulose fibres. *Polimeros: Ciencia e Tecnologia*, **15**, 114–121 (2005).
- [6] Ferreira F. C., Curvelo A. A. S., Mattoso L. H. C.: Preparation and characterization of benzylated sisal fibers. *Journal of Applied Polymer Science*, **89**, 2957–2965 (2003).
- [7] Guinez D., Jasso C., Fuentes F., Navarro F., Davalos F., Ramos J.: Chemical treatments on sisal fibers to produce composite materials with polyethylene and polystyrene. in ‘Abstracts of 8<sup>th</sup> International Symposium on Polymers for Advanced Technologies. Budapest, Hungary’ 140 (2005).
- [8] Lu X., Zhang M. Q., Rong M. Z., Shi G., Yang G. C.: Self-reinforced melt processable composites of sisal. *Composite Science and Technology*, **63**, 177–186 (2003).
- [9] Lu X., Zhang M. Q., Rong M. Z., Shi G., Yang G. C.: All-plant fiber composites. I: Unidirectional sisal fiber reinforced benzylated wood. *Polymer Composites*, **23**, 624–633 (2002).

- [10] Zhang M. Q., Rong M. Z., Lu X.: Fully biodegradable natural fiber composites from renewable resources: All-plant fiber composites. *Composites Science and Technology*, **65**, 2514–2525 (2005).
- [11] Oksman K., Lindberg H.: Influence of thermoplastic elastomers on adhesion in polyethylene-wood flour composites. *Journal of Applied Polymer Science*, **68**, 1845–1855 (1998).
- [12] Liao B., Huang Y., Cong G.: Influence of modified wood fibers on the mechanical properties of wood fiber-reinforced polyethylene. *Journal of Applied Polymer Science*, **66**, 1561–1568 (1997).
- [13] Zaini M. J., Fuad M. Y. A., Ismail Z., Mansor M. S., Mustafah J.: The effect of filler content and size on the mechanical properties of polypropylene/oil palm wood flour composites. *Polymer International*, **40**, 51–55 (1996).
- [14] Nitz H., Reichert P., Römling H., Mülhaupt R.: Influence of compatibilizers on the surface hardness, water uptake and the mechanical properties of poly(propylene) wood flour composites prepared by reactive extrusion. *Macromolecular Materials and Engineering*, **276–277**, 51–58 (2000).
- [15] Kaci M., Cimmino S., Silvestre C., Duraccio D., Benhamida A., Zaidi L.: Ethylene butyl acrylate glycidyl methacrylate terpolymer as an interfacial agent for isotactic poly(propylene)/wood flour composites. *Macromolecular Materials and Engineering*, **291**, 869–876 (2006).
- [16] Kaci M., Zaidi L., Benhamida A., Cimmino S., Duraccio D.: Ethylene n-butyl acrylate glycidyl methacrylate terpolymer as compatibilizer for isotactic polypropylene/wood flour composites. *Czasopismo Techniczne*, **103**, 251–256 (2006).
- [17] Xu B., Simonsen J., Rochefort W. E.: Creep resistance of wood-filled polystyrene/high-density polyethylene blends. *Journal of Applied Polymer Science*, **79**, 418–425 (2001).
- [18] Mansour S. H., Asaad J. N., Abd-El-Messieh S. L.: Synthesis and characterization of brominated polyester composites. *Journal of Applied Polymer Science*, **102**, 1356–1365 (2006).
- [19] Matuana L. M., Mengeloglu F.: Microcellular foaming of impact-modified rigid PVC/wood-flour composites. *Journal of Vinyl and Additive Technology*, **7**, 67–75 (2001).
- [20] Pedro B. M. A., Monteiro E. C., Dweck J.: PVC and agalmatolite composite characterization. *Polymer Testing*, **20**, 269–273 (2001).
- [21] Sain M. M., Balatinecz J., Law S.: Creep fatigue in engineered wood fiber and plastic compositions. *Journal of Applied Polymer Science*, **77**, 260–268 (2000).
- [22] Chen M.-J., Meister J. J., Gunnels D. W., Gardner D. J. J.: A process for coupling wood to thermoplastics using graft copolymers. *Advances in Polymer Technology*, **14**, 97–109 (1995).
- [23] Sébe G., Brook M. A.: Hydrophobization of wood surfaces: covalent grafting of silicone polymers. *Wood Science and Technology*, **35**, 269–282 (2001).
- [24] Matuana L. M., Belatinez J. J., Sodhi R. N. S., Park C. B.: Surface characterization of esterified cellulosic fibers by XPS and FTIR spectroscopy. *Wood Science and Technology*, **35**, 191–201 (2001).
- [25] Nunez A. J., Kenny J. M., Reboredo M. A., Aranguren M. I., Marcovich N. E.: Thermal and dynamic mechanical characterization of polypropylene-woodflour composites. *Polymer Engineering and Science*, **42**, 733–742 (2002).
- [26] Hartman J., Albertsson A.-C., Sjöberg J.: Surface- and bulk-modified galactoglucomannan hemicellulose films and film laminates for versatile oxygen barriers. *Journal of Biomacromolecules*, **7**, 1983 (2006).
- [27] Lu Y., Zhang L.: Morphology and mechanical properties of semi-interpenetrating polymer networks from polyurethane and benzyl konjac glucomannan. *Polymer*, **43**, 3979–3986 (2002).
- [28] Sombatsompop N., Chaochanchaikul K.: Effect of moisture content on mechanical properties, thermal and structural stability and extrudate texture of poly(vinyl chloride)/wood sawdust composites. *Polymer International*, **53**, 1210–1218 (2004).